UNIVERSITY OF CALGARY

Complete Characterization of Quantum Optical Processes with a Focus on Quantum Memory

by

Connor Michael Kupchak

A THESIS
SUBMITTED TO THE FACULTY OF GRADUATE STUDIES
IN PARTIAL FULFILLMENT OF THE REQUIREMENTS FOR THE
DEGREE OF DOCTOR OF PHILOSOPHY

DEPARTMENT OF PHYSICS AND ASTRONOMY
CALGARY, ALBERTA
APRIL, 2013

Abstract

This thesis introduces and implements a characterization procedure called coherent state quantum process tomography and applies it to a selection of quantum operations. The procedure holds advantages over previous quantum process tomography methods, a primary one is that a process can be characterized by measuring its effect on a set of coherent states which are readily available from a laser source.

After introduction of the characterization procedure, the method is tested on a simple process of an electro-optical modulator and polarizing beam splitter. The accuracy of the characterization is verified by comparison of the predicted action of the reconstructed process tensor versus the actual experiment involving a squeezed vacuum state. The algorithm is then implemented and verified on a quantum memory system based on electromagnetically induced transparency, a system that was previously shown capable of storing a squeezed vacuum state.

Lastly, a new optical storage system based on a gradient echo memory scheme is constructed and optimized to achieve memory retrieval efficiencies of >80%. To characterize this system, a modified coherent state quantum process tomography algorithm based on the method of maximum likelihood estimation is employed. Despite the high efficiency values, the presence of excess noise resulted in the degradation of the storage device performance to be below the benchmarks of a quantum memory system. This estimation algorithm is also successfully implemented on the non-deterministic processes of photon creation and annihilation.

Acknowledgements

Parodizing[1] one of my many former lab mates, I can summarize my acknowledgements as follows: I owe everybody everything.

In August 2007 I graduated from the University of Western Ontario with my Masters in Medical Biophysics. At that time I was unfulfilled with my graduate school experience thus far, and I felt had really missed out on what I had envisioned doing a graduate degree in physics was going to be like. Deep inside I also felt I had not been true to myself, since in my opinion, I had chosen to "sell out" and leave the physics field after my undergrad. I wanted to make it up to myself by following what I knew was my true passion; working on more fundamental physics problems. It is for that reason I enrolled in a second M.Sc. program at the University of Calgary. It has now been five years and eight months since my first day of graduate school at the University of Calgary, and I can honestly say for a lot of that time I did not believe this day would ever arrive. The amount of physics I have learned from both the experimental and theoretical side of things over these years has been amazing. If it was not for the long list of outstanding people who helped and supported me along the way I may have never made it to this day.

I begin with thanking my supervisor Alex Lvovsky who welcomed me into his group many years ago and was both patient and understanding until I (finally) grew into the quality of physicist he pushes his students to strive for. Alex has taught me a wealth of physics in these past six years; including his informative and simplistic descriptions of many complex concepts that I would have never understood otherwise.

Moving onto the Lab C version 2.0 crew, Ryan Thomas who I worked with for a year and a half taught me many aspects of both theoretical and experimental physics. His

---

[1] Not an actual word!

textbook-level knowledge along with his innovation in the laboratory would often leave me in awe and feeling very fortunate to have him as a lab mate. His endless patience when explaining concepts and ideas to me did not go unnoticed. I thank Geoff Campbell for helping my transition into the Lvovsky lab when I first arrived. I also thank him for coming back to Calgary just to start up the GEM experiment with me; as well all the late night pints at the Den back in the earlier years were a great time. Pierre Jobez was an awesome exchange student to work with, in addition to his endless dedication to the GEM experiment, he was always one to go out for pints and wings after a long days work. I would also like to thank Dr. Morgan Hedges from Wolfgang Tittel's group who was always available for my questions during the last eight months of my degree and was always excited to come to my lab to brainstorm and try out ideas.

When I first started in Alex's group I had very little experimental experience and theoretical background relevant to what I was suppose to be working on. I owe a lot of this transition to the Lab C version 1.0 crew. I thank Dr. Dimtry Korystov for "showing me the ropes" in the lab and teaching me how to operate all the equipment. Big thanks to Dr. Mirko Lobino who was an excellent source of theoretical knowledge and accepted me as part of the Lab C team, he was large part of getting my academic career kickstarted. Rounding out the first version of the Lab C team, I thank Eden Figueroa who really took me under his wing when I first entered the Lvovsky lab, he was always understanding towards my questions and really believed in my capabilities as a physicist. I look forward to my new postdoctoral position in his newly minted group at Stony Brook University this summer.

While we never worked together directly, I owe a big thanks to Andrew MacRae who was there almost everyday throughout my tenure in the Lvovsky group. It was the welcoming and laid back attitudes of both Andrew and Eden that ultimately persuaded me to join the Lvovsky crew. From my first day until the day he departed Andrew always made time to answer my questions and offer guidance in the laboratory. Additionally he had the ability to make me burst out laughing at any moment turning the most miserable of days. You could always count on him to keep the mood in the laboratory light and positive.

During my long tenure in the Lvovsky lab I have had to opportunity to witness more people join and leave than almost all others. Many of these people have had a positive impact on my overall experience including Anna, Boris, Michael, Nitin, Ranjeet, Erick, Travis, Adarsh, Aveek, Aleksey, Aimee, Attie, Erwan, Pan, Roshan, and Matt.

I am very thankful to my parents Dan and Michelle Kupchak and my grandma Florence Beardy for always being supportive of whatever decisions I've made throughout my life. I would also like to mention my late grandfather Paul Kryminski who sadly passed away in the duration of this degree, he was always silently but overwhelming proud of every one of my accomplishments growing up.

Finally I thank my amazing fiancée Krystina who I met during my time in Calgary and who will become my wife and life long partner this summer. She has always been my number one supporter throughout this process and always guided me to look at the positive side of everything. We've been through a lot together already, including the burning down of our first home; I deeply thank her sister and brother-in-law Rachel and Pawel for taking us in and allowing us to live in their home during the final months of my degree. Without Krystina I would have not accomplished this, and because of that I dedicate this thesis to her...this is for you babe!

List of Published Articles

"Experimental characterization of bosonic creation and annihilation operators", R. Kumar, E. Barrios, C. Kupchak and A. I. Lvovsky, *Physical Review Letters* **110**(13):130403, March 2013

"Observation of electromagnetically induced transparency in evanescent fields", R. Thomas, C. Kupchak, G. S. Agarwal and A. I. Lvovsky, *Optics Express* **21**(6):6880 - 6888, March 2013

"Memory for light as a quantum process", M. Lobino, C. Kupchak, E. Figueroa and A. I. Lvovsky, *Physical Review Letters* **102**(20):203601, May 2009

"Complete characterization of quantum-optical processes" M. Lobino, D. Korystov, C. Kupchak, E. Figueroa, B. C. Sanders and A. I. Lvovsky, *Science* **322**(5901):563 - 566, October 2008

Table of Contents

List of Figures and Illustrations

Chapter 1

Introduction

The field of quantum information is founded upon the incorporation of quantum principles into computation and communication. This includes, the discovery of quantum cryptography which promises unconditionally secure transfer of information [4]. Naturally, the fastest method to transfer this information is optically with the use of photons. As a result, in the last decade the scientific community has witnessed a significant advancement of quantum optical technologies. These include but are not limited to: quantum networks [5], quantum computing [6] including quantum optical gates [7], quantum teleportation [8], long distance entanglement distribution [9], quantum metrology [10], and quantum state engineering [11], including refined methods of single photon generation [12, 13]. Almost all of the aforementioned technologies will rely on a trustworthy quantum memory device in order for practical implementation to become a reality [14]. However, before any of these technologies can be integrated into the everyday world for routine use, each component of the quantum optical circuit must have its performance completely understood. This is especially crucial when dealing with quantum optical states that are fragile and could be easily lost or destroyed by interaction with the environment. What is needed is a standard debugging and testing procedure that every optical element must clear before being put in to operation, analogous to what one would expect from an electronics manufacturer before their devices are sent to the retailer. Extending on this, it would be convenient if the testing procedure could be accomplished in a more durable manner, void of the difficulties associated with reliable preparation of near identical copies of complex quantum states.

Returning to quantum memories, an optical quantum memory is a device capable of receiving, storing, and recalling a light state without the need to actually measure the light state. This is in contrast to a classical memory that measures an input state and subsequently reconstructs it. A classical storage technique cannot store two conjugate observables simultaneously without increasing the noise of the output signal; in accordance with the Heisenberg uncertainty principle [15]. Hence, any quantum memory must add less noise than its classical counterpart.

In recent years a copious amount of articles have cited secure long distance quantum communication as a motivating factor for quantum memory development. It is driven by the fact that successful transmission of optical quantum information over distances greater than 200 km becomes severely hindered by the loss of photons in transit through a quantum channel (either optical fibre or free space). Proposals [16] have called for optical quantum memories as a necessary component to practically increase the transmission distance via the implementation of a so-called quantum repeater [17, 18, 19]. This is accomplished by dividing a total transmission distance into a series of links that are connected by nodes housing a reliable optical memory. If the memory is capable of storing an arbitrary quantum state for a sufficient time period, it would permit synchronization so that entangled resources could be distributed over neighbouring links.

A requirement for an optical quantum memory is a device capable of preserving the quantum nature of an unknown state for a sufficient amount of time better than is achievable with any classical device. Many varieties of quantum optical memories exist, with each of them having multiple theses and publications dedicated to their improvement and understanding. For reasons of brevity and keeping in mind the multiple themes of this work, we aim to describe only the most common modalities tersely.

Optical Delay Line

The most straightforward method for storing light is simple application of an optical delay line such as a fibre or cavity. While trivial in implementation, fibres suffer from the obvious shortcomings of propagation loss and by definition, are incapable of on-demand readout. Alternatively, one could also use high Q-factor cavities to achieve the same result, where by externally driving the cavity it can be switched on and off-resonance as a means of extracting the contained light field [20]. The drawback here is that in order to achieve a suitable storage time the light will suffer losses due to the coupling efficiency [14].

Electromagnetically Induced Transparency (EIT)

EIT is one of the most well studied and implemented methods of optical storage. It is a phenomenon most often observed in an ensemble of atoms with a three-level system where a weak probe field and a non-degenerate, strong control field couple to a common excited state (known as Λ-systems which will be discussed in Chapter 3). When the atoms are under two-field resonance, the electric susceptibility can undergo dramatic changes affecting the group velocity of an on-resonant probe pulse. By proper intensity modulation of the control field, a probe pulse can be slowed down to to a complete stop, effectively trapping it, followed by acceleration out of the ensemble on demand. We will discuss this technique in greater detail in Chapter 3 where we implemented and characterized an optical quantum memory device based on EIT.

DLCZ Technique

This scheme is ideally suited for quantum repeater implementations [17] and was one of the earliest proposals that called for atomic ensembles using Λ-systems [16]. The idea is to subject an ensemble to a strong off-resonant “write” pulse on one of the transitions, followed by detection of a single Stokes photon which signifies that the ensemble holds a single excitation. Subsequent application of a “read” pulse can then convert the atomic excitation back into a single photon at the anti-Stokes frequency. In this way, initial detection of the Stokes photon heralds that a signal photon has been loaded into the ensemble which can be "shot out" on demand. Not surprisingly, some have referred to such a prepared ensemble as a "photon gun". The application to quantum repeaters comes from subjecting two identical ensembles to an identical pair of write pulses. Through interference of the Stokes emission channels on a 50:50 beam splitter, a single photon detection prepares the ensembles in an entangled superposition [16]. Placement of such ensembles at the connecting nodes of the channel links allows transmission of the prepared ensemble entanglement over greater distances. While not strictly a read-in read-out quantum memory in its most basic form, this technique has garnered much attention and has been spun into many hybrid experiments.

Photon Echoes

This label encompasses a wide range of optical storage schemes stemming from a light state being absorbed by an atomic ensemble in a coherent manner such that when the absorption process is reversed, the ensemble produces an echo of the original input state. In these techniques, a resonant quantum state is absorbed and delocalized over a frequency-broadened ensemble. As a result, each atom in the ensemble is now in a coherent superposition with all others atoms, with individual phases determined by each atom's position and resonance. Manipulation of the inhomogeneous broadening of the ensemble by an external field allows control of the dephasing and rephasing of the atoms. Upon rephasing, the direction in which the ensemble is most likely to emit the echo is predisposed from the original direction of the incoming light state, a property due to phase matching and collective emission. The fundamentals of these types of memories and the their possible applications will be discussed in detail in Chapter 4. An in depth review of these types of memories in solid state systems can be found in Reference [2], and in atomic vapours in Reference [21].

Off-resonant Faraday Interaction

This technique is very elegant and the reader is better off to seek other sources for a thorough description [22, 14]. This scheme involves the non-destructive interaction between optical polarization and collective atomic angular momentum. The microscopic components of the optical polarization are mapped to a prepared atomic ensemble by off-resonant interaction and subsequent feedback operation to the atoms using an RF-field conditioned on a homodyne measurement of one of the quadratures of the optical field.

Now that a majority of the optical storage techniques involving atomic ensembles have been covered, we believe this is a good place to stop. While other optical storage techniques exist, such as optomechanical, their description provides no benefit to the current discussion and are omitted. A more comprehensive review can be found in the thesis of Mahdi Hosseini of Australian National University [3].

Thesis Overview

The goal of this thesis is twofold. The first is to design a procedure to obtain complete information about how any element of a quantum optical circuit will perform when implemented. To achieve this we will use a procedure known as quantum process tomography (QPT) [23], a tool with a history of process characterization. Specifically we will introduce a completely new method of QPT that only requires probing the process with simple coherent states in order to achieve the characterization (csQPT). This is attractive since coherent states are assumed readily available from a laser source. Once developed, we will verify the reliability of this procedure by testing it on a selection of quantum processes. The second goal is to develop an optical storage device capable of receiving, preserving, and recalling quantum optical states such that it can be classified as a quantum memory. We aim to evaluate whether our devices have reached the designation of a quantum memory through utilizing the full potential of our csQPT method. We will do this for two classes of quantum memory protocols, specifically that of electromagnetically induced transparency (EIT) and a type of photon echo technique called gradient echo memory (GEM).

The remainder of this thesis is organized as follows: Chapter 2 begins by explaining the concept of quantum tomography, why we want it and what information it provides for us. Using some brief descriptions of the quantized nature of light fields we go on to describe how quantum optical states can be measured and characterized. From that point we then proceed to how a quantum optical *process* can be characterized using different quantum process tomography techniques involving coherent states (csQPT). We will also detail the experiments where processes were characterized using these techniques. In Chapter 3 we introduce the phenomenon of EIT and how it can be utilized as a quantum memory and then employ our csQPT techniques on such an EIT memory. Chapter 4 is focused on quantum memories based on photon echo techniques. After an explanation of how photon echoes can be used for memory and what the current state of the art is, we construct a system based on the GEM technique and discuss our classical results. This is followed with the investigation of the quantum capabilities of our GEM system using our csQPT techniques in Chapter 5. Finally, Chapter 6 summarizes the presented work.

Chapter 2

Quantum Process Tomography

2.1 What is Quantum Tomography?

In physics, when we are interested in the state of a physical system, at least from the theoretical side of things, we often write down or calculate a mathematical equation describing what is known about it and how it evolves in time. From an experimental standpoint, if we wish to prepare a physical system in a desired state for any practical application, we almost certainly need complete information about the state both presently, and in the future. If the state of a system abides by the rules of classical physics, one could in principle subject the system to a sufficient set of test measurements to gain knowledge about it. From this information we could identify the state of the system and its dynamics giving us the complete characterization we need. If full information cannot be obtained by direct probing of the system, as is often the case in quantum mechanics, we instead settle for a way to estimate what the state is *most likely to be* using different measurements on an ensemble.

To obtain the information required for characterization we could perform multiple measurements on a single system provided that upon measurement, the system is not disturbed from its current state or can be easily and reproducibly reset to its original form. However, in the regime where quantum effects are apparent, one cannot perform multiple measurements on a system without disturbing it in a manner which changes the state itself due to the uncertainty principle [24]; imposing a fundamental limit on how much information can be retrieved from a single measurement. Therefore, to increase the information we want to gain about a quantum state we must turn to an alternative method. The solution is to use identical preparations of a desired state and subject each preparation to a set of measurements that will give us complete information, this is the principle behind quantum tomography.

Theoretically, the information about a quantum state is found in its state vector $|\psi\rangle$. In general, an arbitrary quantum state $|\psi\rangle$ can be written in a decomposition of basis states $|\psi_n\rangle$.

$$|\psi\rangle = c_1|\psi_1\rangle + c_2|\psi_2\rangle + c_3|\psi_3\rangle \ldots, \tag{2.1}$$

where, in the most general form, the corresponding coefficients c_n can be complex. These coefficients, if known, provide us with information related to the relative population in each basis state and additionally any phase relationship that may exist between each of the basis states. Preparation and full characterization of this state in a laboratory setting is a daunting task. Not only would we have to devise a series of measurements to project the state on the full set of basis states but would also require a controllable, phase sensitive setup to accurately measure any phase shifts that may exist between the basis states. This adds a degree of difficulty when attaining experimental characterization, since phase dependent measurements are, in general, more complicated to implement.

Of high relevance to the context of this thesis, information about a quantum state of a system can also be found in its density operator. If a system is described by an ensemble of quantum states $|\psi_i\rangle$ (here $|\psi_i\rangle$ are not necessarily basis states) the density operator $\hat{\rho}$ is

$$\hat{\rho} = \sum_i p_i|\psi_i\rangle\langle\psi_i|, \tag{2.2}$$

where p_i are the probabilities of measuring the system in state $|\psi_i\rangle$. Note that by Equation (2.2) the density operator is by definition a linear decomposition of its possible states. If the decomposition in Equation (2.2) forms an orthonormal basis such that $|\psi_i\rangle = |a_j\rangle$, where $\langle a_j|a_k\rangle = \delta_{jk}$, then the matrix elements of the density operator $\rho_{jk} = \langle a_j|\hat{\rho}|a_k\rangle$ form what is called the density matrix. Then conveniently, the diagonal elements of the density matrix ρ_{jj} are the probabilities of measuring the system in state $|a_j\rangle$ and the off-diagonal elements ρ_{jk} correspond to the coherences between $|a_j\rangle$ and $|a_k\rangle$. Many results presented in this thesis will be in regard to elements of the density matrix, it is related to the density operator by the expression

$$\hat{\rho} = \sum_{j,k} \rho_{jk} |a_j\rangle\langle a_k|. \tag{2.3}$$

To further illustrate the difficulty in obtaining phase information, I will describe a modified example from the one given in Reference [25]. Suppose we have an ensemble (1000 say) of identically prepared 1D quantum masses on springs (quantum harmonic oscillators) at time $t = 0$, hence identical displacements and momenta (velocities). If we measure the position x of each prepared spring at $t = 0$ each measurement will collapse the wave function into one of the discrete position eigenstates, after measurements on the full ensemble we will gain the position probability density for the oscillator $\mathrm{pr}(x) = |\psi(\mathbf{x})|^2$. This probability density also tells us where the mass is *most likely* to be found. However, if the wave function of this mass is of the form $|\psi(\mathbf{x})|e^{i\phi(\mathbf{x})}$ where $\phi(\mathbf{x})$ is the phase of the wavefunction of the oscillator with respect to some reference, then for complete characterization, we require more information than the constructed probability density. So this leaves us with the question of how can we perform tomography such that we retrieve both position and phase information? In the next sections I will describe how we can, at the very least, achieve this goal for quantum optical states.

2.2 Tomography of Quantum Light

2.2.1 Classical Description of Phase Space

The results in this thesis focus on light states described in the continuous variable (CV) regime. Quantum optical states in their CV representation are best understood using the phase space representation of light and we will therefore provide a brief explanation about what phase space is. To explain this concept, we will once again use the analogy of a mass on a spring, i.e. a classical harmonic oscillator without damping. In this analogy, the dynamics of the mass can be represented by a point following a trajectory in what is known as phase space. Phase space is a 2D space represented on a Cartesian grid with the axes corresponding to the particle's position x and its momentum p. Note that these variables satisfy the classical canonical equations of motion

$$\dot{p} = -\frac{\partial H}{\partial x} \tag{2.4a}$$

$$\dot{x} = \frac{\partial H}{\partial p}. \tag{2.4b}$$

Here H is the Hamiltonian which corresponds to the total energy of the system. For a harmonic oscillator this is given by $H = \frac{p^2}{2m} + \frac{1}{2} m\omega x^2$, where m is the mass of the particle and ω is the frequency of oscillation. Not that the overdot in Equation (2.4) denotes the time derivative. When the mass on the spring is set into oscillation, in phase space its dynamics will map out a circular trajectory as shown in Fig. 2.1a. This is simply the motion described by a quadratic potential, with the radius of the circle related to the amount of total energy in the spring. This is a quantity that remains constant for an ideal spring. If we have an ensemble of nearly identically prepared springs, we can then talk about the phase-space probability distribution of the ensemble. By observing the position and momentum values at the same instant after preparation (Fig. 2.1b) we can build a 2D probability distribution $w(x,p)$ in phase space. This distribution, when constructed, would be governed by the rules of classical probability distributions, those of positivity and normalization.

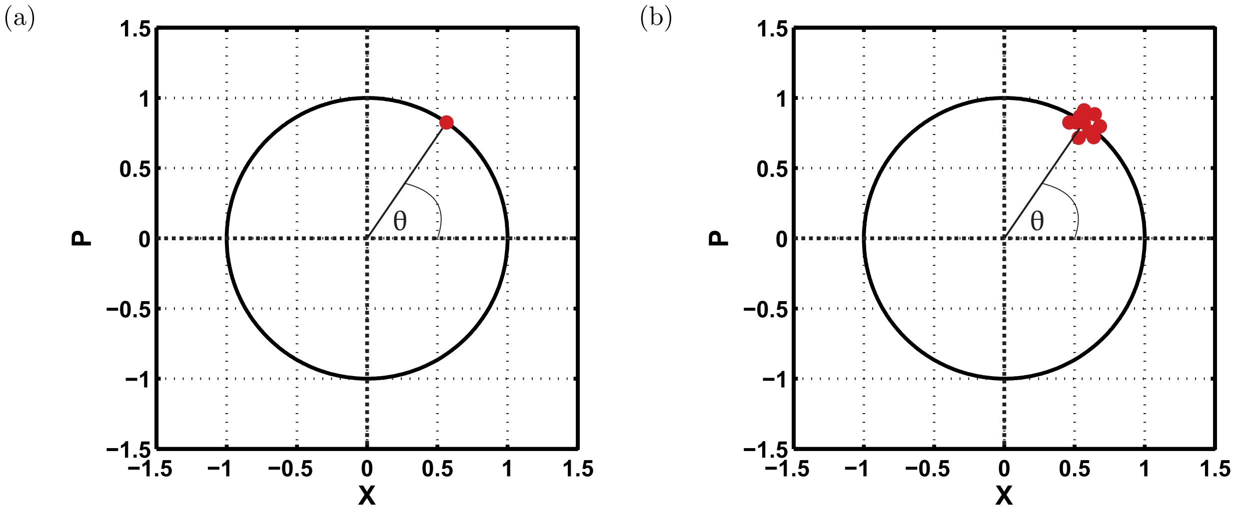

Figure 2.1: Phase space dynamics for a classical harmonic oscillator for the case of a single (a) and nearly identically prepared ensemble of springs (b).

Another important property exhibited by this 2D distribution comes forth if, for a given time t, we measure only the position of the mass, these measurements would give us the position probability distribution described in Section 2.1. This is what's known as the mass's marginal distribution and it is related to the 2D phase space probability density by

$$\mathrm{pr}(x,\theta) = \int_{-\infty}^{\infty} w(x\cos\theta - p\sin\theta, p\sin\theta + x\cos\theta)dp, \tag{2.5}$$

where θ parameterises the elapsed time with $\theta = \theta(t)$ (Fig. 2.1). The marginal distribution is an integral projection of the probability distribution on the plane oriented at an angle θ in the optical phase space. A similar distribution for $\mathrm{pr}(p,\theta)$ can be obtained by measuring only the momentum of the mass.

The analogy of a mass on a spring is very convenient for describing quantum light since the time evolution of a harmonic oscillator is the same as that of an electromagnetic field, providing a natural extension to the optical regime.

2.2.2 Light Quantization

In classical electromagnetism we can define a field to exist in a particular spatial-temporal mode $u(\mathbf{x}, t)$ which describes its values at all moments in time and space. A simple example is a wave (of particular polarization) with a time-dependent amplitude such that $u(\mathbf{x}, t) = e^{i\mathbf{k}\cdot\mathbf{x}-\omega t}$, where $\mathbf{k}$ and ω are the wavevector and frequency of the electromagnetic field respectively. For more complex fields that must obey a set of boundary conditions, such as those confined inside a box, the field can be mathematically formulated as a decomposition of planes waves in a Fourier series. Each of these possible plane waves constitute a mode of the field. Upon quantization of the electromagnetic field it can be derived that the energy stored in a single mode of the electromagnetic field can be found using the same Hamiltonian as the quantum harmonic oscillator [26]

$$\hat{H} = \hbar\omega\left(\hat{a}^\dagger\hat{a} + \frac{1}{2}\right). \tag{2.6}$$

Here, $\hat{a}^\dagger$ and $\hat{a}$ are the bosonic creation and annihilation operators respectively. They are associated with a chosen mode of the electromagnetic field and are mathematically equivalent to the ladder operators of the quantum harmonic oscillator. These operators obey the commutation relation

$$[\hat{a}, \hat{a}^\dagger] = 1. \tag{2.7}$$

However, if we wish to characterize a quantized electromagnetic field via tomography we need to perform measurements on physically observable quantities. Note that these bosonic operators are not Hermitian and their direct measurement is not possible, furthermore we would like quantities analogous to the canonical position and momentum of the classical harmonic oscillator. To achieve this we will use the bosonic operators to form the Hermitian quadrature operators of the quantum field given by

$$\hat{X} = \frac{\hat{a}^\dagger + \hat{a}}{\sqrt{2}} \tag{2.8a}$$

$$\hat{P} = i\frac{\hat{a}^\dagger - \hat{a}}{\sqrt{2}}. \tag{2.8b}$$

If we replace the bosonic operators with quadrature operators in the Hamiltonian of the quantized field we arrive at:

$$\hat{H} = \frac{\hbar\omega}{2}(\hat{X}^2 + \hat{P}^2). \tag{2.9}$$

It can be shown that if these quadrature operators are associated with a mode of the electric field they obey the canonical equations of motion (Eqns. (2.4a) and (2.4b)). Furthermore, through substitution of Equations (2.8a) and (2.8b) into Equation (2.7) we find that the position and momentum associated with a single mode of the electromagnetic field give the commutation relation

$$[\hat{X}, \hat{P}] = i, \tag{2.10}$$

and it can be shown that $\hat{X}$ and $\hat{P}$ therefore exhibit the uncertainty relation of

$$\langle \Delta\hat{X}^2 \rangle \langle \Delta\hat{P}^2 \rangle \geq \frac{1}{4}. \tag{2.11}$$

Here $\Delta\hat{X}^2$ and $\Delta\hat{P}^2$ are the variance of the position and momentum quadratures and the angle brackets $\langle\rangle$ correspond to the quantum mechanical expectation value. Any state whose canonical variables hold the minimum value for the above inequality (Eqn. (2.11)) is known as a minimum uncertainty state.

Turning our attention to the energy quantization, the number of excitations in a particular mode of the electromagnetic field can be found via the number operator defined as:

$$\hat{n} = \hat{a}^\dagger \hat{a}. \tag{2.12}$$

The eigenstates of this operator are what are known as the Fock states $|n\rangle$, which form an orthonormal basis $\langle m|n\rangle = \delta_{mn}$ and will be of high relevance in the following sections. Since photons are bosonic particles, the operations of the creation $\hat{a}^\dagger$ and annihilation $\hat{a}$

on states of a definite number of photons m will incremented or decremented the photon number m by one, respectively [26]:

$$\hat{a}^{\dagger}|m\rangle = \sqrt{m+1}|m+1\rangle \tag{2.13a}$$

$$\hat{a}|m\rangle = \sqrt{m}|m-1\rangle. \tag{2.13b}$$

Using the above properties we can calculate the energy in the mode of the field from Equation (2.6) and with the help of Eqns. (2.8a) and (2.8b), the quadrature variance for any Fock state is

$$\langle \Delta\hat{X}^2 \rangle = \langle \Delta\hat{P}^2 \rangle = \langle n|\hat{n} + 1/2|n\rangle = n + \frac{1}{2}. \tag{2.14}$$

We note that the vacuum state $|0\rangle$ satisfies the criteria of a minimum uncertainty state (Eqn. (2.11)). Finally, since we are interested in doing CV measurements, it is useful to state the wave functions of these Fock states in the quadrature basis [27]:

$$\psi_n(X) = \langle X|n\rangle = \frac{H_n(X)}{\sqrt{2^n n! \sqrt{\pi}}} e^{-\frac{X^2}{2}}, \tag{2.15}$$

where H_n denote the Hermite polynomials of order n. Immediately we see that for the case of no excitations (a vacuum state with $n = 0$) the position wave function is given by Gaussian centred at the origin of phase space $\psi_0(X) = \frac{1}{\pi^{1/4}} e^{-\frac{X^2}{2}}$.

2.2.3 Coherent States

In this thesis we utilize coherent states to completely characterize a quantum optical process (to be discussed in detail in Section 2.6), and therefore their description is paramount to the following sections. In quantum optics, coherent states are a preeminent class of states since they are a close approximation of the states emitted by a laser and of high relevance in quantum optics experiments. The first quantum optical description of these states was by Glauber [28] and they can be formally defined as the eigenstate of the annihilation operator:

$$\hat{a}|\alpha\rangle = \alpha|\alpha\rangle. \tag{2.16}$$

Here, α holds information about the phase and amplitude and in general is, complex-valued. Coherent states have several important properties relevant to this work, first, they can be expressed as a superposition in the Fock basis:

$$|\alpha\rangle = e^{-\frac{|\alpha|^2}{2}} \sum_n \frac{\alpha^n}{\sqrt{n!}} |n\rangle. \tag{2.17}$$

We see that a given coherent state does not contain a definite number of photons and the photon number statistics follow a Poissonian distribution. However, the mean photon number of the state $|\alpha\rangle$ will be given by

$$\langle n\rangle_{|\alpha\rangle} = \langle\alpha|\hat{a}^\dagger\hat{a}|\alpha\rangle = \alpha^*\alpha\langle\alpha|\alpha\rangle = |\alpha|^2, \tag{2.18}$$

and similarly the photon number variance can be calculated to be

$$\langle\Delta n^2\rangle = |\alpha|^2. \tag{2.19}$$

Like the vacuum state $|0\rangle$, coherent states are also minimum uncertainty states satisfying the equality in Eqn.(2.11):

$$\langle\Delta\hat{X}^2\rangle_{|\alpha\rangle} = \langle\Delta\hat{P}^2\rangle_{|\alpha\rangle} = \frac{1}{2}. \tag{2.20}$$

Note that from Equations (2.20) and (2.14) coherent states have the same quadrature variance as the vacuum state $|0\rangle$ and Equation (2.16) is valid for the case of $\alpha = 0$. These characteristics imply that the vacuum state is a zero-amplitude coherent state. At this point we introduce the displacement operator $\hat{D}(\alpha) = \exp(\alpha\hat{a}^\dagger - \alpha^*\hat{a})$, a unitary operator since the expression $i(\alpha\hat{a}^\dagger - \alpha^*\hat{a})$ is Hermitian. The action of the displacement operator on an amplitude $\hat{a}$ will be as follows [27]:

$$\hat{D}(\alpha)^\dagger\hat{a}\hat{D}(\alpha) = \hat{a} + \alpha. \tag{2.21}$$

Therefore coherent states are displaced vacuum states and can be calculated by the operation

$$|\alpha\rangle = \hat{D}(\alpha)|0\rangle. \tag{2.22}$$

Like vacuum states, the distribution of a coherent state's position and momentum quadratures are Gaussian in nature. Hence, the position wave function for a given coherent state is

$$\psi_{|\alpha\rangle}(X) = \psi_0(X - X_0)e^{iP_0X - i\frac{P_0X_0}{2}}, \tag{2.23}$$

where the decomposition of the complex amplitude into its real and imaginary parts is

$$\alpha = \frac{X_0 + iP_0}{\sqrt{2}}. \tag{2.24}$$

Finally we look at the time evolution of these coherent states in phase space. When acted on by the evolution operator $\exp(-i\hat{H}t/\hbar)$, where the Hamiltonian is that of Equation (2.6), a coherent state $|\alpha\rangle$ becomes:

$$e^{i\hat{H}t/\hbar}|\alpha\rangle = e^{-i\omega t/2}|e^{-i\omega t}\alpha\rangle. \tag{2.25}$$

We can see from Equation (2.25) that after time evolution, a coherent state will remain a coherent state but with a different eigenvalue. Like the example of the mass on a spring, under time evolution coherent states plot out the trajectory of a circle of radius $|\alpha|$ (Fig. 2.2).

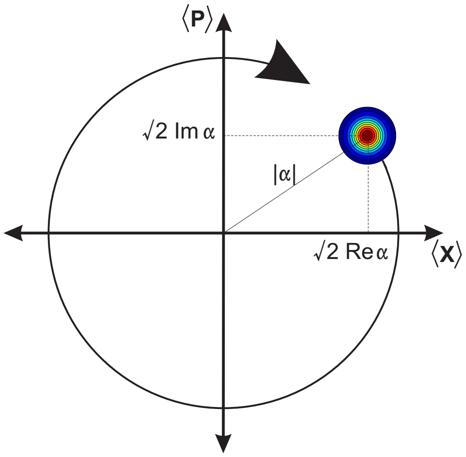

Figure 2.2: Time evolution of position and momentum observables for a coherent state. The 2D ring structure represents the Gaussian nature, and hence quadrature uncertainties of the state.

2.2.4 Squeezed States

In regard to this thesis, while not as important as coherent states, *squeezed* states will be used for verification of our process characterizations for some of the experiments. So far both the vacuum state $|0\rangle$ and coherent states $|\alpha\rangle$ hold the minimum value of Equation (2.11). A pure squeezed state is also a minimum uncertainty state but in contrast to Eqn. (2.20), exhibits $\langle \Delta\hat{X}^2 \rangle < 1/2$ with $\langle \Delta\hat{P}^2 \rangle$ increasing accordingly. Mathematically, we can define an operator that gives rise to this class of states [27]:

$$\hat{S} = \exp\left[\frac{\zeta}{2}(\hat{a}^2 - \hat{a}^{\dagger 2})\right]. \tag{2.26}$$

This is the unitary squeezing operator where the parameter ζ is called the squeezing parameter. Action of this operator on a single vacuum mode $\hat{S}|0\rangle$ generates a single-mode squeezed vacuum state. Contrary to coherent states where the photons are uncorrelated to each other, a squeezed state consists of correlated photon pairs. As a result, the noise (quadrature distribution) at a particular phase is reduced with respect to coherent states

(Eqn. (2.20)). Squeezed states satisfy the criterion to be classified as *nonclassical*[1].

2.2.5 The Wigner Function

In the preceding sections we have introduced and described some basic properties of numerous quantum optical states. Now we would like to visually represent these states in a way that provides complete information about them. In classical mechanics and optics we could gain this information via tomography and the phase-space probability density function $w(x, p)$, as described Section 2.1. The distribution $w(x, p)$ quantifies the probability of measuring a simultaneous x and p value and therefore this distribution provides all the information to completely describe the state in classical physics. Ideally, we would like to have a similar distribution for our quantum optical state. However, in the realm of quantum mechanics the phase-space probability density does not exist since the notion of measuring a particle's exact position in phase space, both position x and momentum p, is not possible due to the uncertainty principle. Similarly in quantum optics we cannot simultaneously know the exact value of orthogonal quadratures (Eqn. (2.11)). We can, however, perform measurements on a single quadrature (X or P) or a linear combination of X and P at some angle in phase space (i.e. in a different basis):

$$\hat{X}_\theta = \hat{X}\cos\theta + \hat{P}\sin\theta. \tag{2.27}$$

With the availability of a large number of identical state preparations we can obtain multiple measurements along a chosen angle in Equation (2.27) and one will be able to build a probability distribution (or marginal distribution) of the chosen quadrature operator (Eqn (2.5)). Similar distributions can be obtained by rotating to a new angle and repeating the measurements. Analogous to the classical case, a function exists which relates the marginal distributions at all angles (Eqn. (2.5)). This function is called the

---

[1] A quantum optical state is said to be classical if it can be expressed as a statistical mixture of coherent states, and non-classical if it cannot.

Wigner function $W(X,P)$ [27] and its definition is (note that Q is a dummy variable)

$$W_{\hat{\rho}}(X,P) = \frac{1}{2\pi}\int_{-\infty}^{\infty} e^{iPQ}\left\langle X - \frac{Q}{2}\right|\hat{\rho}\left|X + \frac{Q}{2}\right\rangle dQ. \tag{2.28}$$

A measurement set on a particular basis constitutes a integral projection of the state's Wigner function along that plane. The major difference for states in the quantum regime, is that the phase space probability distribution is no longer restricted to the rules of classical probability. While the Wigner function is both real and normalized, it is not necessary that the distribution be positive everywhere: it can take on negative values! Hence, the Wigner function on its own does not hold the meaning of classical probability density and is instead defined as a *quasi-probability* distribution. From Equation (2.28) the Wigner function of a quantum state can be calculated directly from that state's density matrix $\hat{\rho}$ and hence it is uniquely determined for a given quantum optical state. Therefore, like the density matrix, the Wigner function also provides us with complete information about the state, i.e. its statistical quantities of mean values and variances, which can be presented in a convenient, visual manner. An example Wigner function and a corresponding marginal distribution is shown in Figure 2.3. It can be seen that the Wigner function provides us with both the mean value and statistical distributions of the quadratures values.

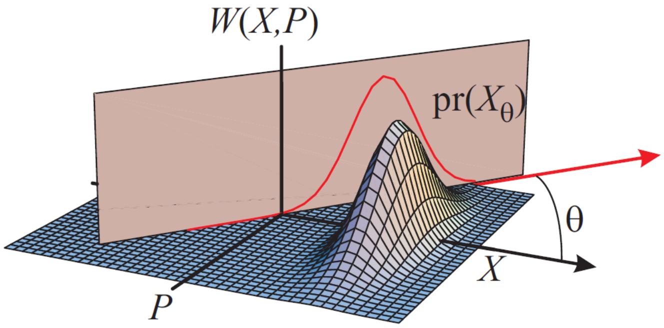

Figure 2.3: Example Wigner function and corresponding marginal distribution at a given angle θ.

Also of central importance to the work is this thesis, specifically to process tomography, is another quasi-probability distribution called the Glauber-Sudarshan P-function [29, 30]. The P-function for a given quantum state $\hat{\rho}$ can be found by the deconvolution of the state's Wigner function and the Wigner function of a vacuum state:

$$W_{\hat{\rho}}(X, P) = \frac{1}{2\pi} \iint_{-\infty}^{\infty} P_{\hat{\rho}}(X', P') W_{|0\rangle\langle 0|}(X - X', P - P') dX' dP'. \tag{2.29}$$

For quantum light states the P-function usually has a highly singular nature. For instance, following from Eqn. (2.29), of a coherent state $|\alpha\rangle$ whose Wigner function is Gaussian by nature has a P-function described by a delta function $P_{|\alpha\rangle\langle\alpha|} = \delta^2(\alpha)$. Hence, reconstruction of a given quantum state's P-function, which often contains higher order cumulants, is a task preferably left avoided.

2.3 Measurement of Quantum Optical States

2.3.1 The Difficulty in Measuring Quantum Light

Now that we have Wigner functions available to help describe and characterize quantum light states, how does one physically obtain the data necessary to use this description? Due to their non-classical nature, Wigner functions cannot in general be measured directly as a probability distribution. However the marginal distributions for a quantum state do indeed follow classical statistics (positive and definite). As alluded to previously, by acquiring the marginal distributions associated with all quadrature operators we can recover the Wigner function of the quantum state.

To measure these projections for optical states we go back to our picture of the classical harmonic oscillator. Suppose we measure the position of the spring mass at a given time to obtain the marginal distribution $\mathrm{pr}(x)$. This by itself is insufficient for full tomography since we need information about all linear combinations of x and p. In order to obtain all projections recall that our harmonic oscillator indeed oscillates, meaning our mass on the spring will be changing its position x and momentum p values with time. This is equivalent to a time dependent rotation $\theta(t)$ of the projection allowing measurements of all possible quadrature operators in Equation (2.27). Instead of measuring the marginal distribution at all angles, one can alternatively measure the distributions at different moments in time through a method called balanced homodyne tomography to be introduced in Section 2.3.2.

Returning to the problem at hand, we are measuring the quantized electromagnetic field, not the position and velocity of a spring mass. In the case of light, it is the electromagnetic wave itself that is oscillating. Immediately we are presented with a few obstacles. The first is that the photodiodes commonly used to measure light, measure only the intensity I of light, where $I \propto |E|^2$ is a static quantity for a plane wave light field. Secondly, waves in the visible spectrum oscillate at hundreds of terahertz, orders of magnitude faster than the limitations of present day photodetectors! Luckily, balanced homodyne tomography allows phase sensitive measurements of the amplitude of a light field using detector speeds currently attainable.

2.3.2 Balanced Homodyne Tomography

To directly measure the quadratures of the quantum state the technique of balanced homodyne detection (BHD) is employed. This is accomplished by interfering a weak light field which we will term the “signal field” with a large amplitude ($|\alpha| \gg 1$) coherent state of known optical phase termed the “local oscillator”, on a 50:50 beam splitter as shown in Figure 2.4. The local oscillator is reflected off a piezoelectric device that provides a dynamic phase modulation $\theta(t)$. If we denote the electric fields of the signal field and local oscillator by E_s and $E_{LO}e^{i\theta(t)}$ respectively, then the output of the two ports of the beam splitter are:

$$E_1(t) = \frac{E_{LO}e^{i\theta(t)} + E_s}{\sqrt{2}} \tag{2.30a}$$

$$E_2(t) = \frac{E_{LO}e^{i\theta(t)} - E_s}{\sqrt{2}}. \tag{2.30b}$$

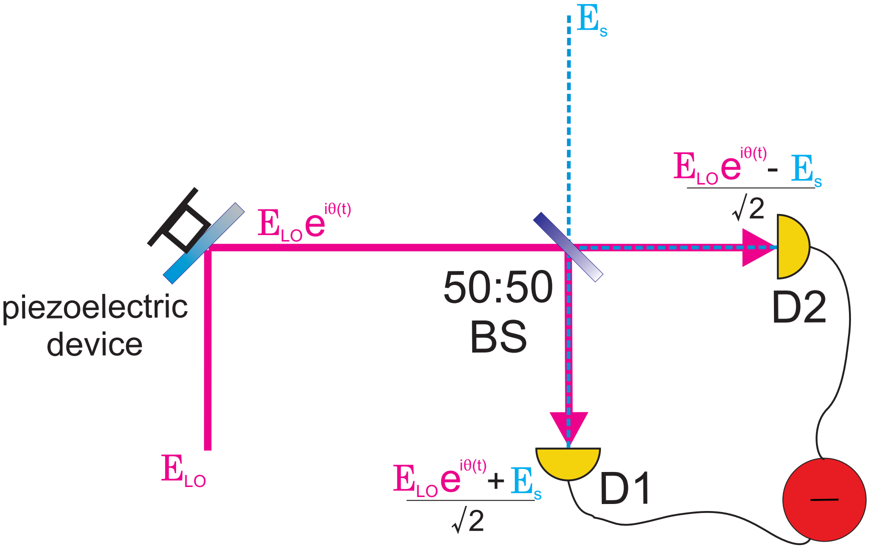

Figure 2.4: Homodyne detection scheme: the weak signal field E_s is interfered with a strong local oscillator beam $E_{LO}e^{i\theta}$ that has a variable phase provided by a piezoelectric device. The resultant photocurrents in each arm are subtracted to produce a signal proportional to the signal field amplitude.

We then measure the output of these two ports on separate high efficiency photodetectors D1 and D2 and subtract their associated photocurrents as depicted in Figure 2.4. Each photodiode produces a current i proportional to the intensity of the field I, the resulting photocurrent difference $i_- = i_1 - i_2$ will be

$$i_- \propto I_1 - I_2 \propto |E_1|^2 - |E_2|^2 = |E_{LO}|(E_s e^{i\theta(t)} + E_s^* e^{-i\theta(t)}). \tag{2.31}$$

Here, since $E_{LO} \gg E_s$ we take the amplitude of the local oscillator to be real such that $E^*_{LO} = |E_{LO}|$ and neglect its field fluctuations. Equation (2.31) leaves us with a photocurrent proportional to only the phase dependent amplitude of the signal field, or in other words the quadrature at a given projection:

$$i_-(t) \propto |E_{LO}| \langle \hat{E}^\theta_s(t) \rangle. \tag{2.32}$$

We see by Equation (2.32) the phase dependent quadrature of the quantum state $E^\theta_s(t)$ is amplified by a factor proportional to the amplitude of the local oscillator field. In the laboratory this means that even weak signals on the order of a few photons can be detected. By performing this measurement at different local oscillator phases, we can obtain the marginal distribution for all projections. This is exactly the information needed to reconstruct the state's Wigner function $W(X, P)$ and density matrix $\hat{\rho}$.

Note the relationship between the homodyne current and signal field amplitude in Equation (2.32) is only a proportional one. To get the exact conversion one must have knowledge of the amplifier gain of the detector, and additionally for any real detector, one must also account for experimental imperfections. One such factor is the conversion efficiency for the percentage of incident photons that are converted to current by the photodiodes, this efficiency is intrinsic to the diode. Another caveat is that Equations (2.30) assume perfect spatial overlap between the local oscillator and the signal field, or in other words the interference between the two fields is assumed to be perfect. Experimentally, achieving near-perfect interference involves a few requirements. The first is that the fields ideally have matching transverse beam profiles; that is, identical intensity profiles across their finite beam waists. The second is that the **k**-vectors of the two fields are completely matched. The degree of spatial overlap between the two light fields is quantified by the visibility $\mathcal{V}$. The visibility can be determined by scanning the phase between two light fields of equal intensity I_0 and recording the minimum and maximum observed intensities to compute the quantity:

$$\mathcal{V} = \frac{I_{max} - I_{min}}{I_{max} + I_{min}}, \tag{2.33}$$

where the theoretical minimum and maximum intensities are $I_{min} = 0$ and $I_{max} = 4I_0$ respectively. If there is not perfect overlap between the fields we will observe a reduction in the intensity modulation and degradation in the interference. This results in $I_{min} > 0$ and by Equation (2.33) we will not achieve a perfect visibility of $\mathcal{V} = 1$. Both the imperfect detector efficiency and non-unit visibility will be equivalent to attenuation of our signal field, an effect detrimental to any procedure involving the measurement of quantum light states. This is why it is crucial when performing any quantum optics experiment to employ the highest efficiency photodiodes attainable and to carefully match the signal and local oscillator fields to obtain the highest reasonably achievable visibility. Mathematically, these losses can be modelled by transmission through a beam splitter interfering with vacuum in the opposite port, i.e. a detector of efficiency η could be treated as a beam splitter with transmission $T = \eta$ [27].

2.4 Quantum Optical Modes

Thus far we have discussed the importance of spatial-mode matching when detecting and characterizing quantum light. However, the matching of the spatial modes is only one of the degrees of freedom that need to be matched when performing quantum optics experiments. The term mode is associated with all degrees of freedom exhibited by our light state, which include: spatial, polarization, longitudinal (frequency), temporal, and quadrature. In the derivation of Equation (2.32) it was assumed that the local oscillator was prepared with the same polarization, frequency, and ideally spatial mode as the signal field. Any deviations in the local oscillator mode to that of the signal field would ruin any perfect cancellation of the fields and subsequently decrease the visibility. Equation (2.32) also corresponds to an instantaneous measurement of the signal field quadrature $\hat{E}_s^\theta(t)$.

As is often the case with quantum memory applications our light state exists as a pulse, meaning that it is defined in a specific temporal mode. If a light state is prepared in a specific (normalized) temporal mode $\phi(t)$ the associated quadrature in that mode can be defined by

$$\hat{Q} = \int_{-\infty}^{\infty} \hat{q}(t)\phi(t)dt, \tag{2.34}$$

where $\hat{q}(t)$ is the instantaneous field quadrature value in the spatial mode of the signal field. Experimentally, the measured quadrature value can be found by integrating the photocurrent from the BHD in Equation (2.32) over a particular weighting function $\psi(t)$ determined by temporal modulation of the pulse:

$$\hat{Q}_{meas} \propto \int_{-\infty}^{\infty} \hat{\imath}_-(t)\psi(t)dt. \tag{2.35}$$

In reality, this relationship between the homodyne current and the measured quadrature value is more complex due to the presence of electronic noise and a limited bandwidth of the detection system. Neglecting electronic noise for the moment, the bandwidth of the detector is limited by its time response. Basically, the time response is a measure of how fast the detector can follow changes in the signal: any signal fluctuations faster than this limit will be averaged out. An ideal detector would have a time response $r(t)$ with the behavior of a Dirac delta function which would correspond to an instantaneous response. In a real detector, the response function $r(t)$ will have some finite width and the maximum frequency measurable by the detector will scale as the inverse width via the Fourier relation. The actual photocurrent from BHD is the result of a convolution of the detector response function and the instantaneous quadrature value $\hat{q}(t)$ such that:

$$\hat{\imath}_-(t) = \int_{-\infty}^{\infty} \hat{q}(t')r(t-t')dt'. \tag{2.36}$$

If we again measure in the temporal mode $\psi(t)$ we find that

$$\hat{Q}_{meas} \propto \iint_{-\infty}^{\infty} \hat{q}(t')\psi(t)r(t-t')dtdt' = \int_{-\infty}^{\infty} \hat{q}(t')\psi'(t')dt', \tag{2.37}$$

where $\psi'(t') = \int_{-\infty}^{\infty} \psi(t)r(t-t')dt$. It can be seen by preparing our light state in the temporal mode $\phi(t) = \psi'(t)$ the effects of limited bandwidth can be corrected for, however actual preparation of such a precise temporal mode would be difficult. A simpler solution involves only ensuring that the detector bandwidth is comparable to or larger than the inverse temporal width of the signal field, a requirement which is sufficient to not degrade the measurement of the state.

In regard to electronic noise, its presence will result in an increase the variance of the quadrature value measured in the mode, this can effectively be modelled as a loss experienced by the quantum state. The effect of the loss caused by electronic noise can be reduced by increasing the optical power to the local oscillator channel [31].

2.4.1 Maximum Likelihood Estimation

Using BHD to measure a suitable data set of phase and quadrature values $\{X_j, \theta_j\}$ one can also measure all necessary marginal distributions $\Pr(X, \theta)$. These distributions can then be used to reconstruct a state's density matrix and Wigner function using a few possible techniques. The most straightforward is to invert an equation similar to Eqn. (2.5) with $w(x, p)$ replaced by the Wigner function. This involves using a filtered back-projection algorithm, a technique common to medical imaging to produce 3D images from 2D projections. However, this method has inherent drawbacks, in that numerical representations of the integration kernel must be approximated due to the singularity at the origin. Adding to the problem is that integration limits must be invoked at some finite cutoff value leading to possible artifacts and unphysical representations (i.e. non-unit trace of the density matrix) in the reconstructions [25]. While no quantum state reconstruction method can be perfect due to the finite measurement precision and size of the data set, we still seek a technique that guarantees a physical density matrix and minimal reconstruction artifacts. The solution is to use a *maximum likelihood algorithm*, a method which selects, from amongst all possible density matrices, the one that fits the data with the highest probability. This method guarantees a physical density matrix and does not suffer from the aforementioned reconstruction artifacts.

The measurements necessary for tomography come from positive operator-valued measures (POVMs), or in other words the state in question is projected on to an eigenstate of the measurement apparatus (i.e. homodyne detector). For BHD we can associate the full set of possible measurement results to a set of basis states $\{|X_\theta\rangle\}$[2]. In other words, we want the distributions of all projections in Equation (2.27). With a large set of measurements on identically prepared copies of optical quantum state $|\psi\rangle\langle\psi| = \hat{\rho}$, we can tabulate the number of occurrences $f_{j,\theta}$ of each possible measurement outcome $|X_{j,\theta}\rangle$. Here, the subscript j will index all possible observed quadratures when integrating the photocurrents. Then the *likelihood* $\mathcal{L}$ to obtain the data set $\{f_{j,\theta}\}$ will be

$$\mathcal{L}(\hat{\rho}) = \prod_{j,\theta} \Pr(X_{j,\theta})^{f_{j,\theta}}, \tag{2.38}$$

where $\Pr(X_{j,\theta})$ is the probability of measuring outcome $X_{j,\theta}$ which is determined by our quantum state $\hat{\rho}$, and can be found from[3]:

$$\Pr(X_{j,\theta}) = \langle X_{j,\theta}|\hat{\rho}|X_{j,\theta}\rangle = \mathrm{Tr}\left[|X_{j,\theta}\rangle\langle X_{j,\theta}|\hat{\rho}\right]. \tag{2.39}$$

The principle of a maximum likelihood algorithm would be to estimate the state $\hat{\rho}$ that maximizes $\mathcal{L}$. To start, we take the logarithm of Equation (2.38) which converts the

---

[2] For measurement in the CV regime which is often via BHD the full set of POVMs is, in principle, infinite.

[3] For simplicity we will treat the measurement outcomes as discrete values. Truthfully, since the set of outcomes $\{|X_{j.\theta}\rangle\}$ is infinite we need to bin the quadrature values. Therefore $\Pr(X_{j,\theta}) = \int_{X_j}^{X_{j+1}} X_\theta dX_\theta = \int_{X_j}^{X_{j+1}} \mathrm{Tr}\left[|X_{j,\theta}\rangle\langle X_{j,\theta}|\hat{\rho}\right] dX$. Technically, any detector and signal measuring device already does this.

product into a sum:

$$\ln\left[\mathcal{L}(\hat{\rho})\right] = \ln\left[\prod_{j,\theta}\Pr(X_{j,\theta})^{f_{j,\theta}}\right] = \sum_{j,\theta} f_{j,\theta}\ln(\Pr(X_{j,\theta})). \tag{2.40}$$

We also need to introduce a constraint so that the algorithm produces a physically realizable density matrices such that $\mathrm{Tr}(\hat{\rho}) = 1$, and therefore finding the most likely and realistic density matrix now becomes a Lagrange multiplier λ problem [32]. To find a solution we construct a function of the form

$$F(\hat{\rho}) = f(\hat{\rho}) + \lambda\Phi(\rho), \tag{2.41}$$

where $f(\hat{\rho})$ is the function we want to find the maximum of, in this case the likelihood function $\mathcal{L}$ (Eqn. (2.38)). The function $\Phi(\hat{\rho})$ governs the constraint that must be satisfied which here is $\mathrm{Tr}(\hat{\rho}) = 1$. Since we are trying to find the maximum of $f(\hat{\rho})$ we set $df(\hat{\rho})/d\hat{\rho} = 0$ and likewise since $\Phi(\hat{\rho}) = \mathrm{Tr}[\hat{\rho}] = \mathit{const}$ then $d\Phi(\hat{\rho})/d\hat{\rho} = 0$ and also $\lambda df(\hat{\rho})/d\hat{\rho} = 0$. From the differential of Equation (2.41) with respect to $\hat{\rho}$ we can construct an extremal equation:

$$\frac{dF}{d\hat{\rho}} = \frac{df}{d\hat{\rho}} + \lambda\frac{d\Phi}{d\hat{\rho}} = \frac{d}{d\hat{\rho}}\left[\ln(\mathcal{L}(\hat{\rho})) + \lambda(\mathrm{Tr}(\hat{\rho}))\right] = 0. \tag{2.42}$$

To find the the value of $\hat{\rho}$ that maximizes $\mathcal{L}$ we will first solve for λ, so by carrying out the differentiation in Equation (2.42) we arrive at:

$$\frac{d}{d\hat{\rho}}\left(\sum_{j,\theta} f_{j,\theta}\ln(\Pr(X_{j,\theta}))\right) = \sum_{j,\theta}\frac{f_{j,\theta}}{\Pr(X_{j,\theta})}\frac{d}{d\hat{\rho}}\mathrm{Tr}\left[|X_{j,\theta}\rangle\langle X_{j,\theta}|\hat{\rho}\right] = -\lambda\frac{d}{d\hat{\rho}}\left(\mathrm{Tr}(\hat{\rho})\right). \tag{2.43}$$

At this point, we will utilize the differential properties of traces, specifically that $\frac{d}{d\hat{B}}\mathrm{Tr}(\hat{A}\hat{B}) = \hat{A}^T$ and $\frac{d}{d\hat{B}}\mathrm{Tr}(\hat{B}) = \hat{\mathbb{1}}$ [33] and by noting that $|X_{j,\theta}\rangle\langle X_{j,\theta}| = |X_{j,\theta}\rangle\langle X_{j,\theta}|^T$ Equation (2.43) becomes:

$$\sum_{j,\theta}\frac{f_{j,\theta}}{\Pr(X_{j,\theta})}|X_{j,\theta}\rangle\langle X_{j,\theta}| = -\lambda\hat{\mathbb{1}}. \tag{2.44}$$

Next, because $\sum_{j,\theta} |X_{j,\theta}\rangle\langle X_{j,\theta}|, \hat{\rho} \propto \hat{\mathbb{1}}$ we can multiply both sides by $\hat{\rho}$ to get [34]

$$\sum_{j,\theta} \frac{f_{j,\theta}}{\Pr(X_{j,\theta})} |X_{j,\theta}\rangle\langle X_{j,\theta}|\hat{\rho} = -\lambda\hat{\rho}, \tag{2.45}$$

and then trace both sides of the equation to yield

$$\sum_{j,\theta} \frac{f_{j,\theta}}{\Pr(X_{j,\theta})} \operatorname{Tr}\left[|X_{j,\theta}\rangle\langle X_{j,\theta}|\hat{\rho}\right] = -\lambda \operatorname{Tr}\left[\hat{\rho}\right]. \tag{2.46}$$

One can see that the expression inside the trace on the left hand side of Equation (2.46) is equal to Equation (2.39) and with our constraint of $\operatorname{Tr}(\hat{\rho}) = 1$ we can solve for λ:

$$\sum_{j,\theta} f_{j,\theta} = N = -\lambda, \tag{2.47}$$

where N is the total number of measurements. We can put the result from Eqn. (2.47) into Eqn. (2.45) to get

$$\left[\frac{1}{N}\sum_{j,\theta} \frac{f_{j,\theta}}{\Pr(X_{j,\theta})} |X_{j,\theta}\rangle\langle X_{j,\theta}|\right]\hat{\rho} \equiv \hat{R}_{\hat{\rho}}\hat{\rho}, \tag{2.48}$$

where $\hat{R}_{\hat{\rho}}$ is known as the iteration operator. If for a given data set the density matrix $\hat{\rho}_0$ (or estimator) yields the maximum of Eqn. (2.38) then it is true that

$$\hat{R}_{\hat{\rho}}\hat{\rho}_0 = \hat{\rho}_0, \tag{2.49}$$

and our iteration operator is $\hat{R}_{\hat{\rho}} = \hat{\mathbb{1}}$ because $f_{j,\theta}/N \approx \Pr(X_{j,\theta})$. For this case, and by observation of Eqn. (2.48) we see that $\hat{\rho}_0\hat{R}_{\hat{\rho}} = \hat{\rho}_0$ which means $\hat{R}_{\hat{\rho}} = \hat{R}^{\dagger}_{\hat{\rho}}$ and it also holds true that

$$\hat{R}_{\hat{\rho}}\hat{\rho}_0\hat{R}_{\hat{\rho}} = \hat{\rho}_0. \tag{2.50}$$

If however, we have an estimator $\hat{\rho} \neq \hat{\rho}_0$ (i.e. does not maximize Eqn. (2.38)), then the above operation will produce a new density matrix $\hat{\rho}^{'}$ that is a closer approximation of $\hat{\rho}_0$. An intuitive explanation is as follows: if our current estimator underestimates the probability of obtaining a particular measurement outcome $X_{j,\theta}$ then $f_{j,\theta} > \Pr(X_{j,\theta})$ and the quantity $f_{j,\theta}/\Pr(X_{j,\theta})$ will be greater than one. As a result, the projection operator $|X_{j,\theta}\rangle\langle X_{j,\theta}|$ associated with this value will increase in weight for the next iteration. Of course, the reverse scenario is also true. Starting with an initial "guess" estimator $\hat{\rho}^{(0)}$ (zeroth iteration), we can use an iterative approach to achieve best possible estimation $\hat{\rho}_0$ for the quantum state corresponding to our data. We can now write down the heart of our iteration algorithm

$$\hat{\rho}^{(k+1)} = \frac{1}{\eta}\left[\hat{R}_{\hat{\rho}^{(k)}}\hat{\rho}^{(k)}\hat{R}_{\hat{\rho}^{(k)}}\right], \tag{2.51}$$

where η is a normalization constant to ensure the trace is unity. Each iteration will increase the likelihood (Equation (2.38)) monotonically and will asymptotically approach the most probable density matrix $\hat{\rho}_0$. The iteration scheme is based on Equation (2.50) rather than Equation (2.49) to ensure the diagonal elements of the density matrix are positive after each step [35, 34]. This algorithm will be implemented to reconstruct quantum states in the experiments described in Sections 2.6.1 and 3.2.

Before moving on, it is important to mention that there is another key component of quantum optical technologies that require tomography; that component is quantum detectors. Detectors are of fundamental and practical importance in quantum optical systems, they serve the purposes of both observation and preparation of quantum optical states. Hence, having a detector characterization will be a crucial component of any realized quantum optical procedure. The leaders in this area is the group of Ian Walmsley at Oxford University who have reported the tomography of avalanche photodiodes and photon number resolving detectors [36], which was followed by the tomography of a hybrid detector exhibiting both wave and photon-number sensitivities [37]. With the availability of quantum detector tomography and the methods of state tomography just described, it leaves only one more constituent that requires characterization in order to fully characterize a quantum optical machine. This final component is the tomography of a quantum process, the main focus of this thesis.

2.5 Tomography of a Process

Practical implementation of any complex machine requires precise knowledge of the behaviour for all its constituents. For example, in any electronic circuit constructed of passive and active elements, each element would have its transfer function $H(\omega)$ for all frequencies fully known before the circuit is sent out for large scale manufacturing. The electronic transfer function of each element (or series of elements) serves as a characterization that tells us the frequency response of the system and allows one to evaluate the performance of the circuit independent of the signal at the input. Likewise, a characterization analogous to the electronic transfer function would be crucial for any element of a quantum circuit comprising a technology being developed for practical application. Just as the transfer function for an electronic device will give a reliable prediction of the output signal for any arbitrary input, we need a similar tool to predict how an arbitrary quantum state will be transformed under a quantum operation.

The problem stated above is analogous to the "black box" concept which is commonly used in science and engineering contexts, where a device's characteristics are learned by strictly using knowledge of the input and output signals. Specifically, for our purposes of quantum optical circuits, we have a quantum "black box" into which we send a set of "probe" states. Using knowledge of the quantum states $\hat{\rho}_{in}$ sent into the box, and the corresponding output states $\hat{\rho}_{out}$ they are mapped to, we aim to completely characterize the black box. To align with the themes of this thesis, henceforth we will refer to any quantum black box as a *process*, and the procedure for characterization is what is known as quantum process tomography (QPT). A schematic diagram of the concept is shown in Figure 2.5.

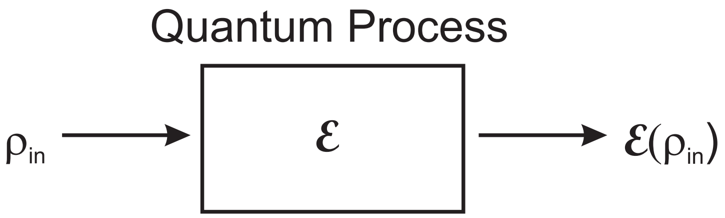

Figure 2.5: Principle of process tomography.

To begin the mathematical theory of QPT, we start with the fact that all quantum processes $\mathcal{E}$ are linear maps in the space of density matrices such that the following holds true:

$$\mathcal{E}(\alpha\hat{\rho}_1 + \beta\hat{\rho}_2) = \alpha\mathcal{E}(\hat{\rho}_1) + \beta\mathcal{E}(\hat{\rho}_2). \tag{2.52}$$

For a bit more insight into why this is true, we refer to Equation (2.2) for the density operator of a system. By its definition, the density operator is a linear decomposition of the states that it is comprised of. The values p_i in Equation (2.2), as was stated, tell us the probability that we will measure the system to be in state $|\psi_i\rangle$. Then intuitively, after operation of a process on the system, a measurement at the output can only correspond to finding the system in the state $\mathcal{E}(|\psi_i\rangle\langle\psi_i|)$ with the probability p_i preserved. Note that this linearity relation is not always valid in vector state space, an easy example being decoherence where a coherent superposition becomes a fully or partially mixed state.

For a quantum state, we can write its density operator $\hat{\rho}$ as a decomposition of basis states such that $\hat{\rho} = \sum_i \lambda_i\hat{\rho}_i$. Then under action of quantum process $\mathcal{E}$, and following from Equation (2.52) we see that:

$$\mathcal{E}(\hat{\rho}) = \sum_i \lambda_i\mathcal{E}(\hat{\rho}_i). \tag{2.53}$$

It becomes immediately apparent that by knowing the effect of the process on a set of basis states $\mathcal{E}(\hat{\rho}_i)$ (via state tomography) we are provided knowledge about the effect of the process on our original quantum state $\hat{\rho}$. However, in its most basic experimental implementation, QPT quickly becomes a cumbersome task. If our states span a dimension d of the Hilbert space, for each $\hat{\rho}_i$ we would need to prepare d^2 separate, linearly independent inputs. After subjecting each input to the process $\mathcal{E}$ we would then require measurement of the d^2 possible output operators $\mathcal{E}(\hat{\rho}_i)$. This brings the total number of measurement configurations necessary for a complete characterization to d^4. To obtain output statistics sufficient to characterize the process, the result of each measurement configuration would be the mean value from an ensemble of identical preparations. This is called standard quantum process tomography (SQPT) [23].

While SQPT requires preparing ensembles of different states, another QPT method is known as ancilla-assisted process tomography (AAPT) that involves preparation of only a single state, i.e. one two-qubit quantum state as oppose to four one-qubit states. Generally in AAPT, a quantum state $\hat{\rho}$ that spans the quantum system A is maximumly entangled with an ancilla state that spans quantum system B with a Hilbert space equal to or greater than A. The quantum process $\mathcal{E}$ is performed on system A leaving B completely isolated. By performing state tomography on the output $(\mathcal{E} \otimes \mathbb{1})(\hat{\rho})$ it is possible to characterize the process $\mathcal{E}$ [38]. AAPT has the advantage of only a single state preparation (as oppose to many in SQPT) but still requires the same amount of measurement configurations as SQPT (e.g. 16 measurements on a single 2-qubit state in AAPT versus 4 measurements on four input states in SQPT). Like SQPT, this technique suffers from the same drawback of needing identical preparations of complex states in order to perform the characterization. In the next section we introduce a scheme which overcomes these shortcomings.

2.6 Coherent State Quantum Process Tomography

We introduce a technique to completely characterize a quantum optical process that utilizes coherent states (Sec. 2.2.3) as our basis states. The procedure is to send in a set of "probe" coherent states to undergo the process and measure the corresponding output state via BHD. After maximum likelihood reconstruction, the output states give full information about the process over all elements of the Fock basis as well as the coherences between them.

The method is derived from the Glauber-Sudarshan decomposition [39, 30] where any quantum state density matrix $\hat{\rho}$ can be represented as a weighted sum of coherent state density matrices (Eqn. (2.54)):

$$\hat{\rho} = \int P_{\hat{\rho}}\left(\alpha\right) |\alpha\rangle\langle\alpha| \, d^2\alpha, \tag{2.54}$$

where $P_{\hat{\rho}}$ is the Glauber-Sudarshan P-function of the state, and α is the coherent state amplitude. By exploiting the linearity in Equation (2.52); from the action of the process $\mathcal{E}$ on the state $\hat{\rho}$, we arrive at

$$\mathcal{E}\left(\hat{\rho}\right) = \int P_{\hat{\rho}}\left(\alpha\right) \mathcal{E}\left(|\alpha\rangle\langle\alpha|\right) d^2\alpha. \tag{2.55}$$

At this point we draw attention to the simplicity and appeal of Equation (2.55); starting with only Equation (2.54) and then utilizing the linearity of quantum processes as described in Section 2.5 we have already reached an expression analogous to Equation (2.53). Furthermore, the output quantum state can be found only with knowledge of the effect of the process in the basis of coherent states, or in other words the action of the process on light states emitted from a laser source.

Before the result in Equation (2.55) can be implemented experimentally we must address a few issues. The first is that, as mentioned in Section 2.2.5, the P-function exhibits singular behavior for non-classical states (i.e. Fock states). The solution first chosen by our group to overcome this obstacle was to apply a theorem by Klauder [40] that used an approximated P-function corresponding to a density matrix that sufficiently approximated the original quantum state. To implement this approximation, we note that the Fourier transform of the operator's Glauber-Sudarshan function always exists and is given by

$$\widetilde{P}_{\hat{\rho}}(k_x, k_p) = \widetilde{W}_{\hat{\rho}}(k_x, k_p) \exp\left(\frac{k_x^2 + k_p^2}{4}\right). \tag{2.56}$$

Here, $\widetilde{W}_{\hat{\rho}}(k_x, k_p)$ is the Fourier transform of state's Wigner function and k_x and k_p are the Fourier variables of the position and momentum observables respectively[4]. By applying a regularizing function (smoothed top hat) $G_L(k_x, k_p)$ to Equation (2.56) we get a truncated version of $\widetilde{P}_{\hat{\rho}}$ such that $\widetilde{P}_{L,\hat{\rho}}(k_x, k_p) = \widetilde{P}_{\hat{\rho}}(k_x, k_p)G_L(k_x, k_p)$. Here, L denotes the length in Fourier space from the origin to where $\widetilde{P}_{L,\hat{\rho}}(k_x, k_p)$ rapidly approaches zero.

To show the validity of this approximation, we tested it on a squeezed vacuum state exhibiting a noise reduction in the squeezed quadrature of -1.58 dB and excess noise in the orthogonal quadrature of 2.91 dB. These decibel quantities are with respect to the variance of the coherent state. Figure 2.6a shows $\widetilde{P}_{L,\hat{\rho}}(k_x, k_p)$ with L =5.2 and the corresponding inverse Fourier transform is shown in Figure 2.6b. The function $\widetilde{P}_{\hat{\rho}}(k_x, k_p)$ was calculated according to Equation (2.56). Figures 2.6c and 2.6d show the Wigner function of the original experimentally reconstructed squeezed vacuum state compared to the one obtained from the approximated P-function respectively. The approximated states exhibit a fidelity greater than 0.9999 with the original.

Before moving on we will digress to speak about fidelity, where fidelity is a measure often used to quantify the overlap or "closeness" between two quantum states, in this case a squeezed vacuum from the approximated P-function compared to the original state. In the space of density matrices, which is what we are most concerned with in this work,

---

[4] In this section we will use lower case x and p for the field quadratures in place of their uppercase versions as was introduced in Section 2.2.2.

the fidelity between two states $\hat{\rho}_1$ and $\hat{\rho}_2$ is found by $F(\hat{\rho}_1, \hat{\rho}_2) = \left[\mathrm{Tr}\left(\sqrt{\sqrt{\hat{\rho}_1}\hat{\rho}_2\sqrt{\hat{\rho}_1}}\right)\right]^2$.

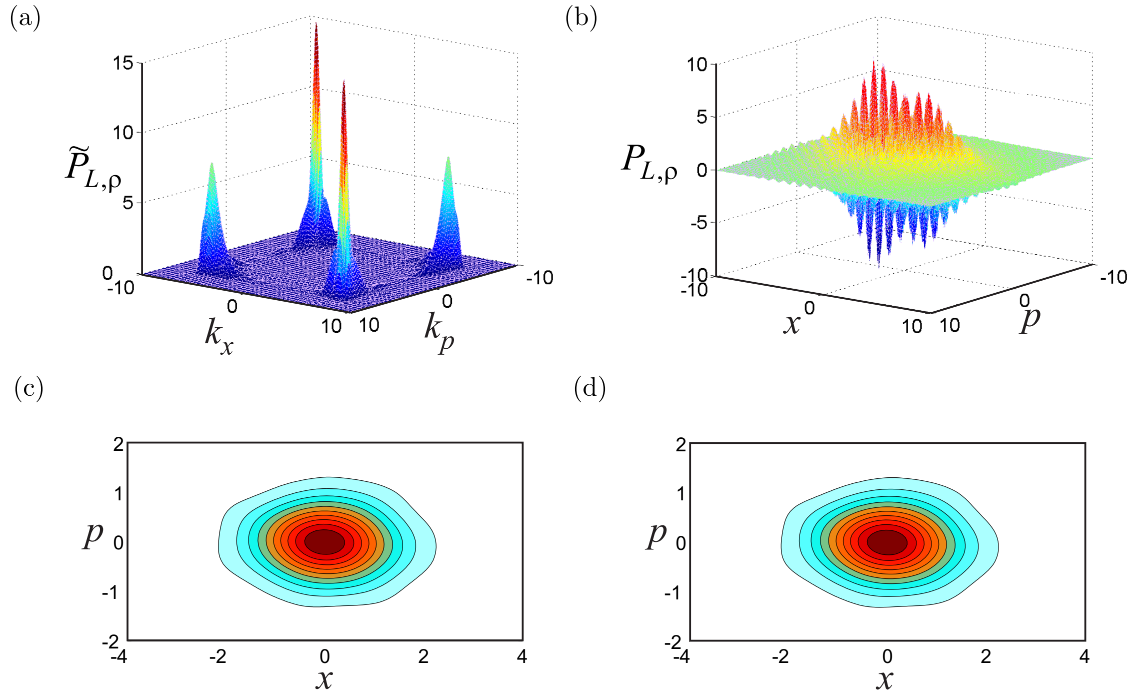

Figure 2.6: Regularized Glauber-Sudarshan decomposition of an experimentally measured squeezed vacuum state. (a) Truncated Fourier transform of the squeezed vacuum P-function, and (b) corresponding inverse Fourier transform. (c),(d) Wigner functions of the originally measured squeezed vacuum and that calculated using the approximation, respectively

The second issue with the direct implementation of Equation (2.55) is the dependence on prior knowledge of a state specific P-function. This situation is not ideal since we aim for a process characterization *independent* of the input state. To circumvent this obstacle, we first assume that our state can be represented by a density matrix in the Fock basis. We can then express our state in a form in accordance with Equation (2.3) which we will then substitute into an expression for the Wigner function (Eqn. (2.28)) to yield [27]:

$$W_{\hat{\rho}}(x,p) = \sum_{m,n=0} \rho_{mn} W_{mn}(x,p). \tag{2.57}$$

Here, m and n denote the indices for the photon number states and $W_{mn}(x,p)$ is the Wigner function of the $|m\rangle\langle n|$ Fock basis projectors. Next, we replace the Wigner function on the LHS of Equation (2.57) with the convolution of its Glauber Sudarshan P-function with the vacuum state Wigner function (Sec. 2.2.5) and take the Fourier transform of both sides to arrive at:

$$\widetilde{P}_{\hat{\rho}}(k_x,k_p)\exp\left(-\frac{k_x^2+k_p^2}{4}\right) = \sum_{m,n=0} \rho_{mn} \widetilde{W}_{mn}(k_x,k_p). \tag{2.58}$$

Finally by referring to Equation (2.56) we can find that the state's Glauber-Sudarshan P-function can be rewritten as [28]:

$$P_{\hat{\rho}}(\alpha) = \sum_{mn} \rho_{nm} P_{nm}(\alpha), \tag{2.59}$$

where P_{mn} is the P-function for the Fock basis projectors $|m\rangle\langle n|$. Equation (2.55) now takes the form:

$$\mathcal{E}\left(\hat{\rho}\right) = \sum_{mn} \rho_{nm} \int P_{nm}(\alpha)\mathcal{E}\left(|\alpha\rangle\langle\alpha|\right) d^2\alpha. \tag{2.60}$$

It can be seen that Equation (2.60) allows one to calculate the effect of the process on a input state $\hat{\rho}$ using the process tensor given by

$$\mathcal{E}_{lk}^{nm} = \int P_{L,nm}(\alpha)\mathcal{E}\left(|\alpha\rangle\langle\alpha|\right)_{lk} d^2\alpha, \tag{2.61}$$

and furthermore we can use the tensor in Equation (2.61) to relate the density matrix of the input and output states:

$$\left[\hat{\rho}_{out}\right]_{jk} = \sum_{m,n,j,k} \mathcal{E}_{jk}^{mn} \left[\hat{\rho}_{in}\right]_{mn}. \tag{2.62}$$

At this moment, we pause and focus on the impact of the results that have just been derived. Equation (2.61) gives us the expression for the process tensor, which in this thesis will be synonymously referred to as the *superoperator*. All information about the process is provided by the quantity on the RHS of Equation (2.61) and thus all dependencies on the quantum input state have now been removed. Instead, we require the P-function for the $|m\rangle\langle n|$ Fock basis projectors, which by use of the regularization procedure, are quantities that can be pre-tabulated. To complete the characterization we only require knowledge of the effect of the process over a sufficient subspace of the coherent state basis. This is information that can be obtained by measuring the process output with a set of coherent states as input using BHD, which is a routine procedure in quantum optical experiments. Thus we have now reached the goal we originally set out for, in that we have the ability to predict the effect of our quantum optical process on *any* input state. Our process tensor is valid in the optical (frequency, spatial, temporal and polarization) mode in which the BHD measurements were carried out. As can be seen by Equation (2.62), with this rank-4 tensor we have the ability to know the output of the process for a given input state, and that our superoperator behaves as a quantum optical analog to an electronic transfer function.

The advantages of this procedure over its SQPT and AAPT predecessors are immediate. We have bypassed the need of preparing an unwieldy number of complex and delicate quantum states to characterize the process, and instead only require mere laser light. This is attractive since laser light is more readily available, and therefore the process can be characterized and optimized in a more robust and reliable manner.

One final point worth mentioning, is that Equation (2.61) is valid for classical light states as well as states that exhibit quantum properties. However, as we have shown, complete information about the process is obtained by measurements on coherent states which follow classical statistics. This is an appealing property, using data that abides by classical statistics we are able to produce a reliable prediction about how quantum statistics will be affected.

Returning back to the problem, we note that the integral in Equation (2.61) is over the entire phase space for a continuous range of α values. To realize this calculation, the integral must be truncated to a maximum amplitude value. Furthermore the output of the process can only be tractably measured at a finite number of α values, therefore polynomial interpolation between the α values is also required.

The value of L required for a faithful state approximation up to a given photon number is shown in Figure 2.7a for fidelities of 99.99% and 99%. Similarly, the lowest amplitude needed in the integration to get a 99% fidelity is shown in Figure 2.7b.

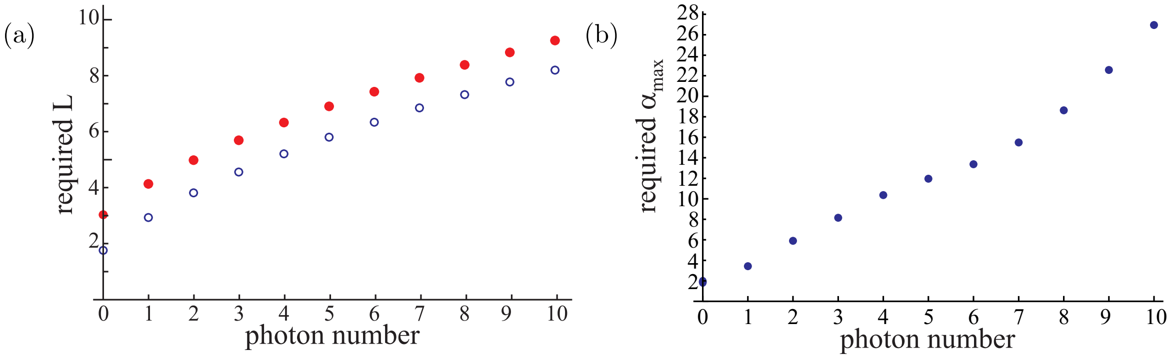

Figure 2.7: Requirements for faithful state approximation up to a particular photon number using a restricted Glauber-Sudarshan decomposition. (a) Shows the low pass filtering parameter L needed for fidelities of 99.99% (red) and 99% (blue-empty). (b) Lowest amplitude needed in the integration for a fidelity of 99%.

Many processes that operate on a single mode of the electromagnetic field exhibit what is known as phase invariance, that is if two input states are identical up to an optical phase shift ϕ the corresponding output states exhibit that same phase shift:

$$\mathcal{E}[\hat{U}(\phi)\hat{\rho}\hat{U}^{\dagger}(\phi)] = \hat{U}(\phi)\mathcal{E}(\hat{\rho})\hat{U}^{\dagger}(\phi). \tag{2.63}$$

In other words, if we know the effect of the process on a given coherent state $|\alpha\rangle$ we will know what the effect will be on any coherent state $|\alpha e^{i\theta}\rangle$. Experimentally, this greatly simplifies the characterization procedure. With phase invariance we only require input coherent states over a sufficient range of real, positive amplitudes, and the need for careful adjustment of phase is removed. In general, any process that does not involve interference with another mode of the electric field will be phase invariant, examples of such processes include: identity, attenuation, photon addition and subtraction, a beam splitter with vacuum in the orthogonal port, and quantum memory. A counter example would be the displacement operator (Sec. 2.2.3) implemented by interfering the input state with a strong coherent state on a weakly reflecting beamsplitter [41].

2.6.1 Proof of Principle Experiment

To test the validity of our Coherent State Quantum Process Tomography (csQPT) method we implemented it on a relatively simple experiment involving an electro-optical modulator (EOM) and a polarizing beam splitter (PBS), a schematic of the setup is shown in Figure 2.8.

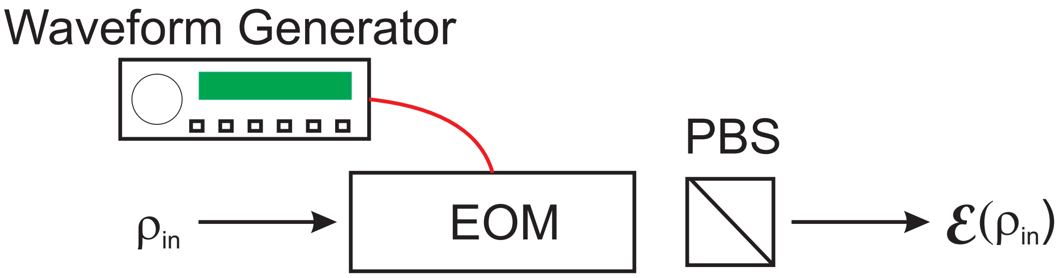

Figure 2.8: Schematic diagram of a proof of principle process. Light undergoes phase modulation through the EOM followed by a loss through the PBS.

By applying a bias voltage to the EOM we observed birefringence and thus losses through the PBS along with a phase shift. To characterize this process, a continuous-wave (CW) Ti:Sapphire laser at 795 nm was employed as our source of coherent states. We sent in 11 different input states as probes with amplitude values ranging from $0 < \alpha < 10.9$ and measured the associated output states via BHD. To obtain an accurate measure of phase shift the voltage was gated at a rate of 10 kHz and the local oscillator phase was modulated at 100 Hz, hence a single oscilloscope trace concurrently measured both the input and output states (Figure 2.9a). These traces allowed recovery of the time dependent local oscillator phase $\theta(t)$ necessary for maximum likelihood reconstruction. For each input and output state, 50,000 quadrature values were obtained by integrating the oscilloscope trace over a uniformly weighted temporal mode (Sec. 2.4) of 20 ns duration. These phase and quadrature values were then used in a maximum likelihood reconstruction algorithm (Sec. 2.4.1) to obtain the corresponding density matrices. We found the output state exhibited a phase shift of 36° and a loss of 34 % with respect to the input state. The state mapping is exemplified by the phase space reconstruction of the Wigner functions which are shown in Figure 2.9b.

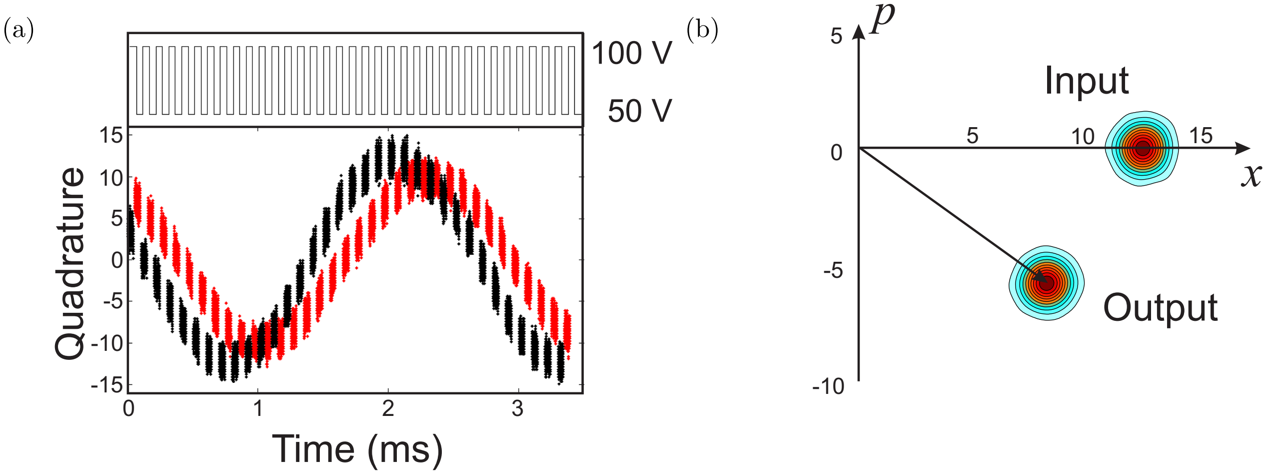

Figure 2.9: (a) Time dependent quadrature values of the coherent states before and after the process measured with BHD and α_{in} =8.3. The black points and red points represent the input and output quadrature values respectively. (b) Phase space representations of the Wigner functions of corresponding input and output traces, note the loss and phase shift.

By fitting polynomials to the output density matrix elements with respect to α we can then use that information in Equation (2.61) to calculate the corresponding process superoperator $\mathcal{E}_{lk}^{nm}$. The diagonal elements of the superoperator $\mathcal{E}_{kk}^{mm}$ that relate the photon number output distribution to a given input Fock state are shown in Figure 2.10. For comparison a theoretical process tensor was calculated by treating the process as a beam splitter with the transmissivity such that the loss is equal to that of the EOM and PBS combination. The orthogonal port is assumed to contain vacuum. The corresponding output density matrix is then given by:

$$\hat{\rho}_{out} = \sum_{m,n} \sum_{k} \rho_{mn} A_{mk} A_{nk} |m-k\rangle\langle n-k|, \tag{2.64}$$

where A_{nk} (A_{mk}) denotes the binomial distribution

$$A_{nk} = \sqrt{\begin{pmatrix} n \\ k \end{pmatrix}} t^{n-k} r^{k}. \tag{2.65}$$

Here, r and t are the beamsplitter reflection and transmission amplitudes respectively. Equation (2.64) is known as generalized Bernoulli transformation and is regularly used in quantum optics calculations to model loss [41]. From Figure 2.10 we can see a close resemblance between the two representations of the superoperators, similar agreement was also found for the non-diagonal terms.

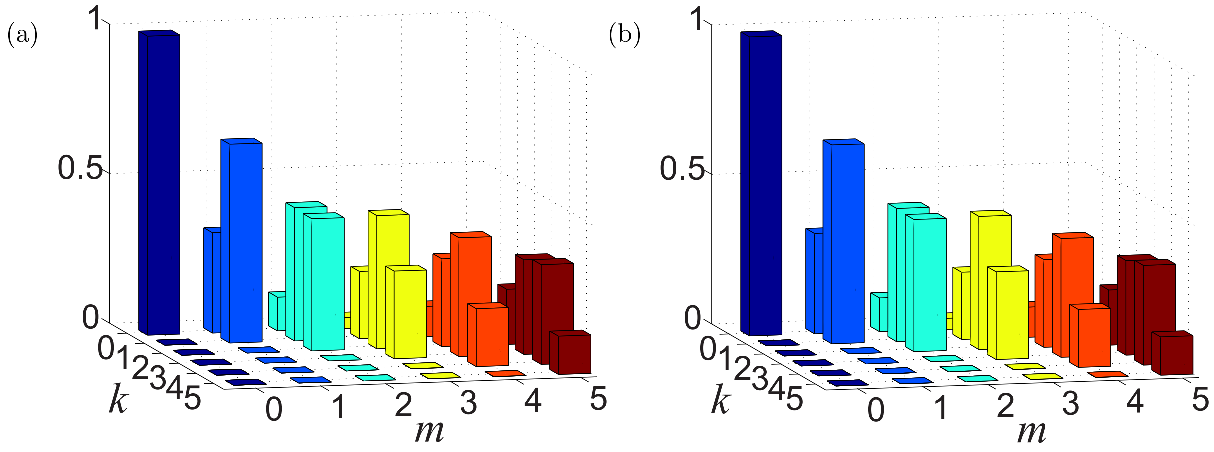

Figure 2.10: The diagonal elements of the superoperator $\mathcal{E}_{kk}^{mm}$. (a) As obtained with our csQPT method and (b) theoretical model.

For verification of our method, we applied the reconstructed superoperator to the experimental density matrix of a squeezed vacuum state and compared the result to the actual experiment. The squeezed vacuum state was prepared using a frequency-doubled beam to pump a periodically poled $KTiOPO_4$ crystal situated inside a bow-tie optical resonator [42]. The reconstructed Wigner functions corresponding to both the prediction and the experiment are shown in Figure 2.11. The predicted quadrature noise reduction after the process was -0.95 dB compared to -1.07 dB for the measurement with 2.15 dB and 2.19 dB excess noise in the orthogonal quadrature for the prediction and measurement respectively. These values corresponded to a fidelity of 0.9935±0.0002 between the prediction and experiment.

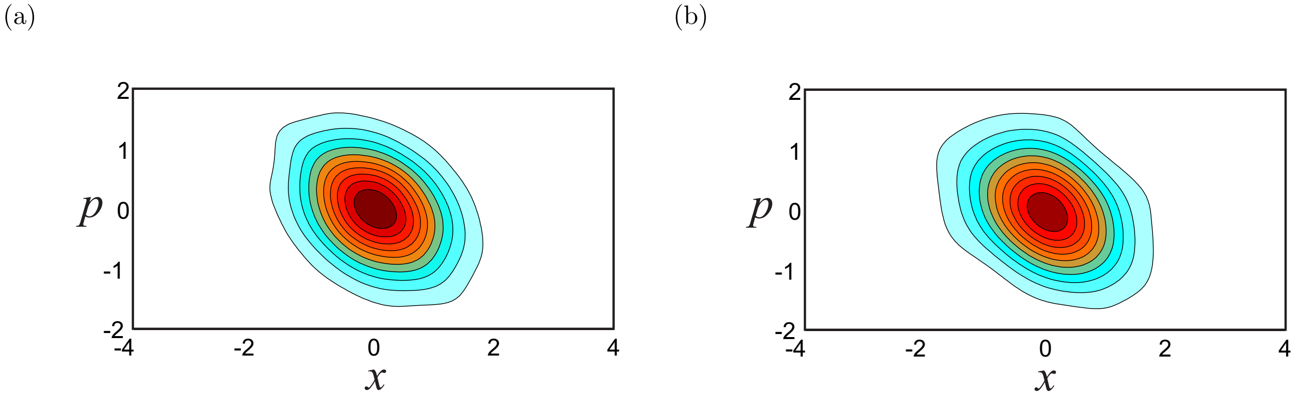

Figure 2.11: Wigner functions of the squeezed vacuum states after action of the process for (a) the csQPT prediction and (b) actual experiment.

To summarize, we have introduced and demonstrated a procedure for completely characterizing quantum-optical processes called coherent state quantum process tomography (csQPT). The method utilizes coherent states to probe the process which are readily available from a laser source. Characterization is achieved by state reconstruction of the output for a series of input states whose amplitudes and phases are easily manipulated. This method of csQPT was also implemented for the characterization of a quantum memory based on Electromagnetically Induced Transparency (EIT) which will be discussed in detail in Chapter 3.

2.7 Other csQPT Methods

Since the publication of the work discussed above [43] two other forms of csQPT [44, 45] have been reported. Both of these methods were utilized in various experiments in this thesis so I will present an overview. However, I would like to state that I had no direct involvement in this work.

2.7.1 Glauber-Sudarshan Function Free Method

In the previously described method of csQPT we required some modified representation of the Glauber-Sudarshan function to obtain the characterization. However, use of this function is not convenient as the function only exists in a highly singular, generalized form for many non-classical states [46]. Despite the approximation employed to alleviate this issue [40], elimination of the high-frequency oscillations will naturally limit the precision of the characterization. Additionally, the truncation bounds for obtaining a suitable regularized function was obtained empirically which is undesirable. Rahimi-Keshari *et al.* [44], reported a method that obviates the direct use of the Glauber-Sudarshan function and therefore completely avoids any ambiguity in the regularization procedure. Starting from the foundation laid in Section 2.6, we use Equation (2.60) to obtain the integral form of the process tensor in the Glauber Sudarshan representation:

$$\mathcal{E}_{lk}^{nm} = \int P_{nm}(\alpha)\langle l|\mathcal{E}(|\alpha\rangle\langle\alpha|)|k\rangle d^2\alpha. \tag{2.66}$$

We now make a substitution for the P function of the Fock basis projectors $|m\rangle\langle n|$ and will instead express it as [28]

$$P_{mn}(\alpha) = (-1)^{m+n}\frac{e^{|\alpha|^2}}{\sqrt{m!n!}}\frac{\partial^m}{\partial\alpha^m}\frac{\partial^n}{\partial\bar{\alpha}^n}\delta^2(\alpha), \tag{2.67}$$

where α and $\bar{\alpha}$ are treated as independent variables for the orthogonal quadratures and $\delta^2(\alpha) = \delta(\mathrm{Re}(\alpha))\delta(\mathrm{Im}(\alpha))$. Substitution of Eqn. (2.67) into Eqn. (2.66) leaves an integral that can be simplified by using integration by parts. Making use of the fact that the Dirac delta function vanishes outside of $\alpha = 0$, the expression becomes

$$\mathcal{E}_{lk}^{nm} = \int \frac{\delta^2(\alpha)}{\sqrt{m!n!}}\left[e^{|\alpha|^2}\langle l|\mathcal{E}(|\alpha\rangle\langle\alpha|)|k\rangle\right] d^2\alpha, \tag{2.68}$$

which can be evaluated to

$$\mathcal{E}_{lk}^{nm} = \frac{1}{\sqrt{m!n!}}\frac{\partial^m}{\partial\alpha^m}\frac{\partial^n}{\partial\bar{\alpha}^n}\left[e^{|\alpha|^2}\langle l|\mathcal{E}(|\alpha\rangle\langle\alpha|)|k\rangle\right]\Big|_{\alpha=0}. \tag{2.69}$$

Note the that the object $\left[e^{|\alpha|^2}\langle l|\mathcal{E}(|\alpha\rangle\langle\alpha|)|k\rangle\right]\Big|_{\alpha=0}$ is computed from experimental data and by Equation (2.69) we can see that the process superoperator can by found by simply taking partial derivatives of this object and evaluating the derivative at $\alpha = 0$. An immediate feature of this method is that complete information about the process is contained in the action of the process on a small subspace of the coherent state basis in the vicinity of the vacuum state. This makes sense since each term of the process output $e^{|\alpha|^2}\langle l|\mathcal{E}(|\alpha\rangle\langle\alpha|)|k\rangle$ is infinitely differentiable and is equal to its Taylor series expansion at any point. Hence, the process can be characterized by calculating the Taylor series of the output matrix at $\alpha = 0$, and the Glauber-Sudarshan representation has been eliminated and thereby sidesteps any transformation of that function to the Fock basis representation. Before moving on we should however state a word of caution about this method. Since calculation of the coefficients could require high order derivatives of the density matrix, an accurate density matrix reconstruction is imperative. Even small errors in the reconstruction can lead to sharp changes in the density matrix elements which in turn will cause even larger errors in the process tensor reconstruction.

Using this method the theoretical process tensors for the identity operation, attenuation, $\hat{a}^\dagger$,$\hat{a}$, Cat state generation, beam splitter, and parametric down conversion process were calculated [44]. This method was also used in the intermediate steps for the work of Kumar *et al.* [47] to be discussed later.

2.7.2 Maximum-likelihood csQPT

The previous two methods of csQPT calculated the process superoperator using the output state density matrices reconstructed via the iterative maximum likelihood estimation algorithm. We now introduce a technique of csQPT that iteratively reconstructs the process tensor in the Fock basis using the output quadrature and phase values *directly*. Hence, the step of reconstructing the output state density matrices is completely bypassed.

Similar to the algorithm for state reconstruction, we will use projection operators $\hat{\prod}_\theta(X) = |X_\theta\rangle\langle X_\theta|$ for a quadrature eigenstate $|X_\theta\rangle$ of the homodyne detector. The probability of detecting a particular phase and quadrature value θ, X on the output of some prepared quantum state $\hat{\rho}_m$ in mode m is:

$$\mathrm{Pr}_\theta^m(X) = \mathrm{Tr}\left[\hat{\prod}_\theta(X)\mathcal{E}(\hat{\rho_m})\right]. \tag{2.70}$$

If we perform a set of N (index i) quadrature and phase measurements[5] on a set of M (index m) coherent states the corresponding log-likelihood function similar to Equation (2.40) is:

$$\ln\left[\mathcal{L}(\mathcal{E})\right] = \sum_{m,i} \ln(\mathrm{Pr}^m_{\theta_{m,i}}(X_{m,i})) = \sum_{m,i} \ln\left(\mathrm{Tr}\left[\hat{\prod}_{\theta_{m,i}}(X_{m,i})\mathcal{E}(\hat{\rho}_m)\right]\right). \tag{2.71}$$

We want to obtain the process tensor $\mathcal{E}$ that maximizes this likelihood function (Eqn. (2.71)) and, similar to Section 2.4.1, want to develop an algorithm that finds the best possible estimate based on measured data. To achieve this we use the Jamiolkowki isomorphism between linear completely positive maps $\mathcal{E}$ from operators on Hilbert space $\mathcal{H}$ to the space $\mathcal{K}$, where $\hat{\rho}_{in} \in \mathcal{H}$ and $\hat{\rho}_{out} \in \mathcal{K}$. Further, we need positive semidefinite operators $\hat{E}$ on the Hilbert space $\mathcal{H} \otimes \mathcal{K}$. The explicit relationship between $\hat{E}$ and $\mathcal{E}$ is [24]:

$$\hat{E} = \sum_{m,n,j,k} \mathcal{E}^{mn}_{jk} |m\rangle\langle n| \otimes |j\rangle\langle k|. \tag{2.72}$$

With this definition along with Equation (2.62) the output state under action of the process is given by:

$$\hat{\rho}_{out} = \mathcal{E}(\hat{\rho}_{in}) = \mathrm{Tr}_{\mathcal{H}}\left[\hat{E}\hat{\rho}_{in}^T \otimes \hat{\mathbb{1}}_{\mathcal{K}}\right], \tag{2.73}$$

where the superscript T denotes the transpose. For trace-preserving processes we note that $\mathrm{Tr}[\hat{\rho}_{out}] = \mathrm{Tr}[\hat{\rho}_{in}]$ and we are given the constraint:

$$\mathrm{Tr}_{\mathcal{K}}[\hat{E}] = \hat{\mathbb{1}}_{\mathcal{H}}. \tag{2.74}$$

---

[5] Here we will change notation slightly from Section 2.4.1, where the subscript i indexes all measurements and subsequently $f_{i,\theta} = 1$ for all measurement outcomes.

Much like the state reconstruction algorithm, we have once again formulated a Lagrange multiplier problem. For the case of identical input and output Hilbert spaces we have $dim\mathcal{H}^4$ parameters and $dim\mathcal{H}^2$ constraints leaving $dim\mathcal{H}^4 - dim\mathcal{H}^2$ free parameters. By substituting Eqn. (2.73) in to Eqn. (2.70) the probability for measuring quadrature value X at a given local oscillator phase θ is:

$$\mathrm{Pr}_\theta^m(X) = \mathrm{Tr}\left[\hat{E}\hat{\rho}_{in}^T \otimes \hat{\prod}_\theta(X)\right]. \tag{2.75}$$

Following the same methodology as Section 2.4.1 and analogous to Equation 2.40, the relevant log-likelihood functional is given by

$$\mathcal{L}(\hat{E}) = \sum_{m,i} \ln(\mathrm{Pr}_{\theta_{m,i}}^m(X_{m,i})) - \mathrm{Tr}\left[\hat{\Lambda}\hat{E}\right] = \sum_{m,i} \ln\left(\mathrm{Tr}\left[\hat{E}\hat{\rho}_{in}^T \otimes \hat{\prod}_\theta(X)\right]\right) - \mathrm{Tr}\left[\hat{\Lambda}\hat{E}\right], \tag{2.76}$$

where $\hat{\Lambda} = \hat{\lambda} \otimes \hat{I}_\mathcal{K}$ and $\hat{\lambda}$ is the Hermitian matrix of Lagrange multipliers for the trace preservation condition (Eqn. (2.74)). By the same routine as was done for state tomography, we setup an extremal equation but this time we differentiate Eqn. (2.76) with respect to $\hat{E}$ such that:

$$\frac{d}{d\hat{E}}\left[\ln(\mathrm{Pr}_{\theta_{m,i}}^m(X_{m,i})) - \mathrm{Tr}\left[\hat{\Lambda}\hat{E}\right]\right] = 0 \tag{2.77a}$$

$$\sum_{m,i} \frac{1}{\mathrm{Pr}_{\theta_{m,i}}^m(X_{m,i})}\hat{\rho}_{in}^T \otimes \hat{\prod}_\theta(X) - \hat{\Lambda} = 0. \tag{2.77b}$$

We can then derive the relation

$$\hat{E} = \hat{\Lambda}^{-1}\hat{R}\hat{E}, \tag{2.78}$$

where $\hat{R}$ serves as the iteration operator similar to Eqn. (2.48):

$$\hat{R} = \sum_{m,i} \frac{1}{\mathrm{Pr}_{\theta_{m,i}}^m}(X_{m,i})\hat{\rho}_{in}^T \otimes \hat{\prod}_\theta(X). \tag{2.79}$$

Due to Hermicity, Equation (2.78) can also be stated as $\hat{E} = \hat{E}\hat{R}\hat{\Lambda}^{-1}$ and we arrive at

$$\hat{E} = \hat{\Lambda}^{-1}\hat{R}\hat{E}\hat{R}\hat{\Lambda}^{-1}. \tag{2.80}$$

Determination of $\hat{\Lambda}$ is achieved by using the above expression for $\hat{E}$ in the trace preservation condition Eqn. (2.74)

$$\hat{\lambda} = (\mathrm{Tr}_K[\hat{R}\hat{E}\hat{R}])^{1/2}. \tag{2.81}$$

By starting with an unbiased initial $\hat{E}$ such as $\hat{E}^0 = \hat{I}_{\mathcal{H}\otimes\mathcal{K}}/(dim\mathcal{K})$, Equations (2.74) and (2.81) can be solved numerically through iterations. After each iteration both the positive semi-definiteness of $\hat{E}$ is ensured and constraint $Tr_K[\hat{E}] = \hat{I}_{\mathcal{H}}$ is satisfied.

Similar to the method above that circumvents the use of the Glauber-Sudarshan function, this technique only requires a small range of input α values to complete the reconstruction. This is ideal since suitable reconstruction of high amplitude coherent states is technically challenging. The method just outlined has since been implemented in a few experiments, first, in the experimental process reconstruction of the photon addition and annihilation operators $\hat{a}^\dagger, \hat{a}$ to be presented in the next section, and in characterization of an optical storage device based on a gradient echo memory scheme to be presented in Chapter 5.

2.8 Experimental Characterization of Bosonic Creation and Annihilation Operators

A practical device capable of implementing photon creation and annihilation operations (Eqn. (2.13a) and (2.13b)) would be a valuable component of a quantum state engineering toolbox. However, employing these operators is challenging, since they are non-trace preserving processes, and can only be realized in an approximate, non-deterministic fashion. Previously, groups have applied the photon annihilation operation for the generation of optical "Schrödinger cats" [48], continuous-variable qubits [49], and entanglement distillation [50]. In regard to the photon creation operation, photon added states have been used to verify bosonic commutation relations [51]. Photon annihilation can be achieved by use of a low reflectivity beam splitter (Fig. 2.12a) transmitting a target state $|\psi\rangle$. A successful single photon detection in the reflection channel indicates a photon has been lost and the state in the transmission channel is approximated by $\hat{a}|\psi\rangle$. Photon creation, from an experimental standpoint, is more challenging and requires sending the target state into a nonlinear optical crystal undergoing a low-amplitude spontaneous parametric down-conversion (SPDC) process. When SPDC occurs, a creation event $\hat{a}^\dagger$ takes place in both signal and idler modes, by detection of a single photon in the idler channel, the target state becomes $\hat{a}^\dagger|\psi\rangle$ (Fig. 2.12b). Using probe coherent states and our csQPT methodology we aim to reconstruct the process superoperator capable of predicting the action on photon number states in accordance with Equations (2.13a) and (2.13b).

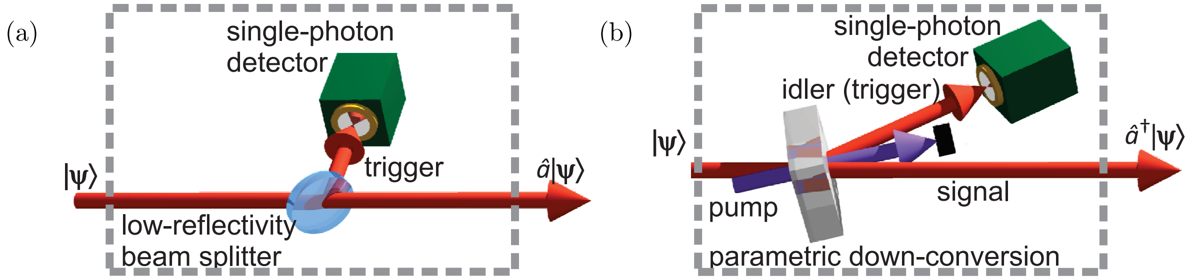

Figure 2.12: Schematic experimental setups for (a) photon annihilation and (b) creation. Both processes are heralded by single photon detections.

2.8.1 Preliminary Results

The first implementation of the photon subtraction operator was obtained with a setup similar to Figure 2.12a. The probe field and local oscillator were generated with a Ti:Sapphire (Coherent MBR-110) laser operating in the CW regime near 795 nm. We used pulsed coherent states as input that were generated using two acousto-optical modulators (AOM) to create pulses of 1 μs duration. The annihilation operation was realized with a half-wave plate and PBS serving as a weakly reflecting beam splitter. Subtraction events were recorded with a single photon counting module (PerkinElmer SPCM-AQR-

14-FC) with a dark count rate of 72 Hz. We used 9 different coherent states with amplitudes ranging from $\alpha = 0$ to $\alpha = 12$ and subjected them to the annihilation process. The quadrature and phase values of the output were measured using BHD and the corresponding count rate in the reflection channel was also recorded. The output state density matrices were reconstructed using 50 000 time-averaged phase and quadrature values input into a maximum likelihood reconstruction algorithm (Sec. 2.4.1).

Contrary to the experiment involving the EOM and PBS, the photon annihilation process is non-deterministic meaning the probability of occurrence is dependent on the input state. Accounting for this dependence is crucial in order to reconstruct an accurate process tensor. The success probability is obtained by renormalization of the process output such that $\mathrm{Tr}[\mathcal{E}(|\alpha\rangle\langle\alpha|)]$ is proportional to the event probability. Hence, applying this procedure to the photon annihilation operator we find:

$$\mathrm{Pr}_{\hat{a}}(\alpha) \propto \mathrm{Tr}[\mathcal{E}(|\alpha\rangle\langle\alpha|)] = |\alpha|^2. \tag{2.82}$$

Note that neglecting the $|\alpha|^2$ coefficient responsible for the probabilistic nature of $\hat{a}$ would be equivalent to reconstructing the identity process. We can then see that accurate reconstruction of the process tensor will only be dependent on *i)* the polynomial fit to the success probability which should be linear with respect to $|\alpha|^2$ and *ii)* the quality of the reconstructed coherent states. Fitting of the polynomial yielded a success probability of 0.01 per mean photon number in the input. Using the method described in Section 2.6 we computed the corresponding process tensor with the diagonal elements $\mathcal{E}_{kk}^{mm}$ shown in Figure 2.13.

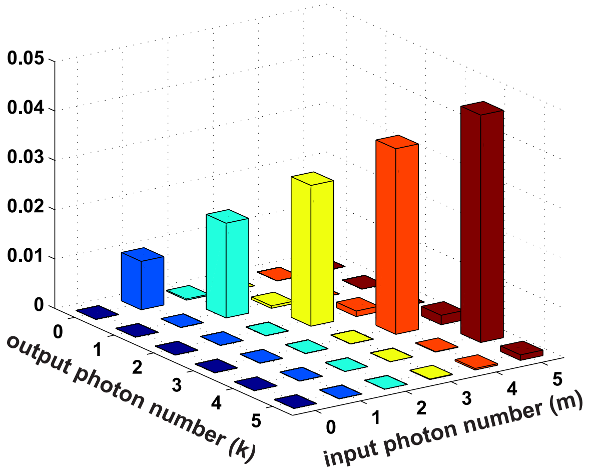

Figure 2.13: Diagonal elements $\mathcal{E}_{kk}^{mm}$ of the first reconstruction of the photon subtraction operator. The vertical axis corresponds the probability that the annihilation operation $\hat{a}$ was successful.

The interpretation of the elements of this tensor is straightforward, where each colour corresponds to the photon number distribution of the output or the Fock state input $|m\rangle$ present at the input. From Eqn. (2.13b) we would expect $(\mathcal{E}_{\hat{a}})_{kk}^{mm} = m\delta_{k,m-1}$ consistent with the "lowering" features of this operator. Furthermore, the height of the tensor elements increase linearly with the input photon number as one would expect from Eqn. (2.82). After this preliminary result, the experiment was moved into another laboratory such that both processes $\hat{a}$ and $\hat{a}^\dagger$ could be characterized.

2.8.2 Experiment

In the second implementation, all light beams were derived from a mode-locked Ti:Sapphire laser (Coherent Mira 900) at 790 nm that emits transform-limited pulses of width 1.6 ps at a 76 MHz repetition rate. Photons heralding the successful action of the processes were registered by a PerkinElmer SPCM-AQR-14-FC single photon detector. Field quadratures of the process output were measured by a high-bandwidth balanced homodyne detector [31]. Probe field amplitudes were controlled via a half-wave and PBS combination. SPDC required for photon creation was generated by first manufacturing a frequency-doubled beam by single pass of the 790 nm light through a 17 mm long lithium tiborate (LBO) crystal, which typically yielded 80 mW of SHG pump. This field was then focussed into a 2 mm long periodically poled potassium-titanyl phosphate crystal phase-matched for type II SPDC producing orthogonally polarized signal and idler modes.

Characterization was achieved by subjecting a set of coherent states with amplitudes ranging from 0 to 1.7 to the processes and by acquiring quadrature and phase data of the output. The count rates needed to calibrate the success probability was recorded for each input. Theoretically, the success probability for each of these processes should behave as:

$$\mathrm{Pr}_{\hat{a}}(\alpha) \propto \langle\alpha|\hat{a}^{\dagger}\hat{a}|\alpha\rangle = |\alpha|^2, \tag{2.83a}$$

$$\mathrm{Pr}_{\hat{a}^{\dagger}}(\alpha) \propto \langle\alpha|\hat{a}\hat{a}^{\dagger}|\alpha\rangle = 1 + |\alpha|^2. \tag{2.83b}$$

Experimentally we observed probabilities that were consistent with Equations (2.83) as shown in Fig. 2.14.

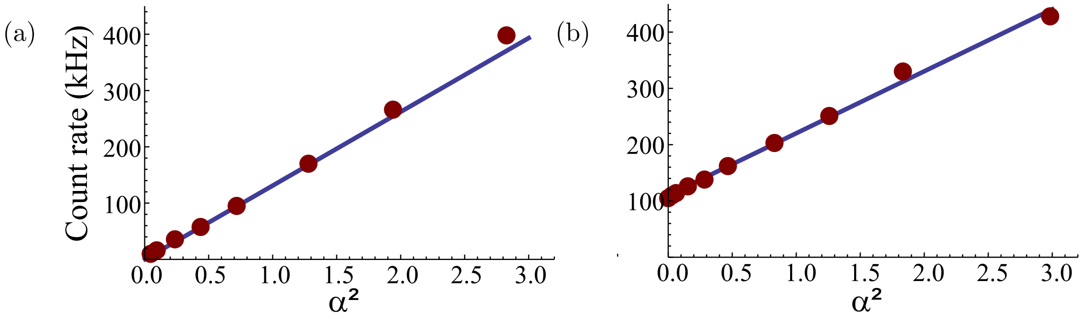

Figure 2.14: Count rates for (a) photon annihilation and (b) photon creation events as a function of input coherent state amplitudes squared. Solid lines give the expected theoretical dependencies.

With these count rates and the phase and quadrature values, process tensors for both operators were obtained using the csQPT method based on maximum likelihood estimation described in Section 2.7.2 (Shown in Fig. 2.15).

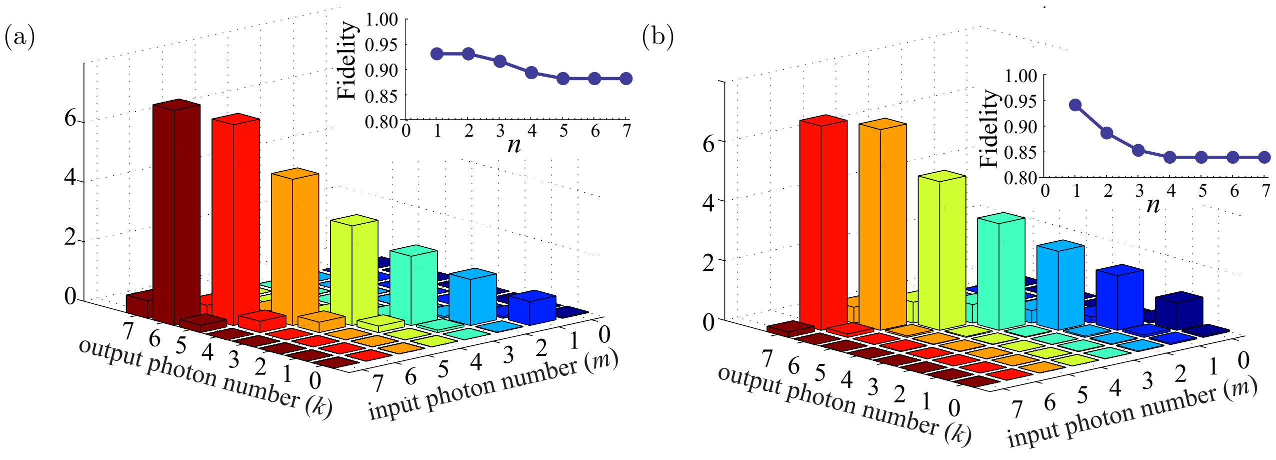

Figure 2.15: Diagonal elements of the process superopertor $\mathcal{E}_{kk}^{mm}$ for (a) photon annihilation and (b) creation processes reconstructed from experimental data. Insets are the worst-case fidelities of the reconstructed processes acting within the relevant subspace of the optical Hilbert space.

The interpretation for the annihilation operator $\hat{a}$ was already described previously. For the creation operator $\hat{a}^\dagger$, we observed the expected behavior $(\mathcal{E}_{\hat{a}^\dagger})_{kk}^{mm} = (m+1)\delta_{k,m+1}$ corresponding with the “raising” feature of the operator. Additionally, the height of the tensor elements increase linearly in accordance with Eqn. (2.83b). The insets show the estimated worst-case fidelity between the normalized states $\hat{a}|\psi\rangle, \hat{a}^\dagger|\psi\rangle$ and the respective outputs $\mathcal{E}_{\hat{a},\hat{a}^\dagger}(|\alpha\rangle\langle\alpha|)$ of the reconstructed processes. Finally, when characterizing these processes one must also consider any experimental imperfections that can distort the recorded measurements. The details of how such effects were quantified can be found in Reference [47], where all effects equivalent to a loss were accounted for directly in the reconstruction algorithm.

Chapter 3

Process Tomography of a Memory Based on Electromagnetically Induced Transparency

The importance of a quantum memory device as it applies to quantum information was discussed in Chapter 1 and we now set our sights on the characterization of such a device. To do so, we will apply our csQPT techniques introduced in Sections 2.6 and 2.7.2 to characterize quantum memories suitable for quantum light states. This will be in an attempt to answer the general question: How will an *arbitrary* quantum state of light be preserved after storage in a memory apparatus? We begin with one of the most widely implemented quantum memory techniques, that based on electromagnetically induced transparency (EIT).

3.1 Electromagnetically Induced Transparency (EIT)

3.1.1 Theory

Electromagnetically induced transparency is a phenomenon observed in atoms with a Λ-type energy level scheme in the presence of two on or near-resonant laser fields that couple two non-degenerate electronic ground states to a common excited state. The *transparency* occurs when the two optical dipoles driven by the laser fields interfere in the excited level and render the atoms transparent to both fields and consequently trap the atomic populations in the ground states. The fields consist of a relatively weak probe which is monitored for transparency and a strong control field that mediates the interaction of the probe with the atomic system. With the control field absent the probe undergoes typical two-level absorption; when it is present the system will exhibit two-photon resonance and the absorption will significantly decrease. The cause of the transparency is the presence of a so-called dark state of the atoms that does not interact with the fields. This concept was first used in the description of coherent population trapping (CPT) [52].

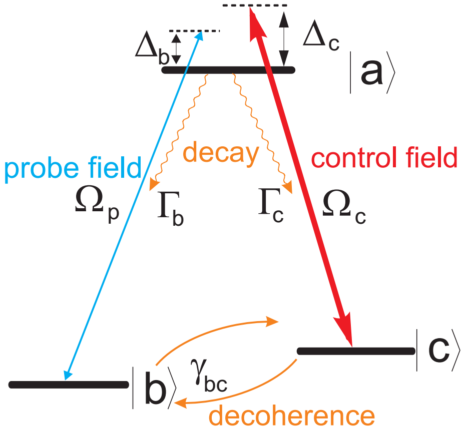

Figure 3.1: A Λ-type atom with associated coupling fields and decoherence and decay mechanisms shown. Rubidium atoms, which will be utilized in this work, exhibit this type of energy level scheme.

To understand the concept of a dark state first consider an atom featuring this aforementioned Λ scheme (Figure 3.1) with two non-degenerate ground states $|b\rangle$ and $|c\rangle$ (dipole-forbidden meaning transitions are not allowed between the two states) that couple to a shared electronic excited state $|a\rangle$ (dipole-allowed). The strong control field couples the $|c\rangle \Leftrightarrow |a\rangle$ transition with Rabi frequency Ω_c and is detuned from resonance by frequency Δ_c, the weak probe field couples the $|b\rangle \Leftrightarrow |a\rangle$ transition with Rabi frequency Ω_p and is detuned by Δ_b. Here, the Rabi frequency is the rate at which the atomic population will exchange levels in a two-level system. For a given dipole-allowed interaction the Rabi frequency is given by $\Omega \equiv \frac{|\mathbf{E}\cdot\mathbf{d}|}{\hbar}$, where $\mathbf{d}$ is the dipole moment and $\mathbf{E}$ is the electric field. In the interaction picture and under the rotating wave approximation the Hamiltonian associated with this system takes the following form:

$$\hat{H} = -\hbar \begin{bmatrix} \Delta_b & \Omega_p & \Omega_c \\ \Omega_p^* & 0 & 0 \\ \Omega_c^* & 0 & \Delta_b - \Delta_c \end{bmatrix}. \tag{3.1}$$

We will neglect decay and decoherence for the moment. Of particular interest is the case of two-photon resonance $\Delta_c = 0$, in which one of the eigenstates, called the dark state, of this Hamiltonian is:

$$|\psi\rangle_d = \frac{1}{\sqrt{|\Omega_p|^2 + |\Omega_c|^2}}(\Omega_c|b\rangle - \Omega_p|c\rangle). \tag{3.2}$$

This state is a coherent superposition of the ground states and contains no component of the excited state. Atoms prepared in this state do not interact with either laser field, and in the absence of ground state dephasing they will remain in their present ground state. This effect is known as coherent population trapping. EIT is a particular case of CPT where we have the condition $\Omega_p \ll \Omega_c$ causing most of the population to occupy only one ground state $|b\rangle\langle b| \approx 1$, it is in this configuration where a transparency dip will be observed on the probe field transition.

Before moving forward note that in any practical implementation of EIT, the dark state $|\psi\rangle_d$ will experience degradation due to incoherent population exchange and dephasing processes. Such effects are labeled in Figure 3.1 and must be included in the Hamiltonian to calculate an accurate atomic response to the light fields. We use the Lindblad formalism to incorporate the degradation effects and calculate the subsequent time evolution of the density matrix using the master equation [53]:

$$\partial_t \rho = -\frac{i}{\hbar}[\rho, H] + (\partial_t \rho)_{decay}, \tag{3.3}$$

where $(\partial_t \rho)_{decay}$ holds the decay and dephasing terms that affect the density matrix elements. After the inclusion of dephasing effects, one can solve Equation 3.3 in the steady state $\partial_t \rho = 0$ and obtain the pertinent elements of the density matrix. Specifically, we need the element corresponding to the susceptibility χ of the medium with respect to the probe field which is ρ_{ab}. Using the fact that the mean polarization for an atomic ensemble is given by $P = N d \rho_{ab}$ and the susceptibility for linear media is related by $P = \epsilon_0 \chi E$ we can calculate χ to be

$$\chi = \frac{N d^2}{\hbar \epsilon_0} \frac{\delta + i\gamma}{|\Omega_c|^2 - (\delta + i\gamma)(\Delta_b + i\Gamma/2)}, \tag{3.4}$$

where N is the number density of the atomic ensemble, γ is the ground state decoherence rate, and Γ is the excited state relaxation rate. For convenience we have renamed the variables $\delta = \Delta_b - \Delta_c$ and $\Gamma = (\Gamma_b + \Gamma_c)/2$. The susceptibility in Equation (3.4) is related to the complex-valued refractive index for light where $n = \sqrt{1+\chi} \approx 1 + \frac{\chi}{2}$. With this relation we can find the amplitude transfer function of the medium [54]:

$$T(\omega, z) = e^{i\mathbf{k}\cdot\mathbf{z} - i\omega t} \approx e^{i\mathbf{k}_0\cdot\mathbf{z} - i\omega t} e^{i\mathbf{k}_0\cdot\mathbf{z}\frac{\chi(\omega)}{2}}. \tag{3.5}$$

From Equation (3.5) it is apparent that the real and imaginary components of Equation (3.4) correspond to the dispersive and absorptive (respectively) responses of the probe field near atomic resonance. Figure 3.2 shows the real and imaginary terms of the Equation (3.4) with and without the control field present.

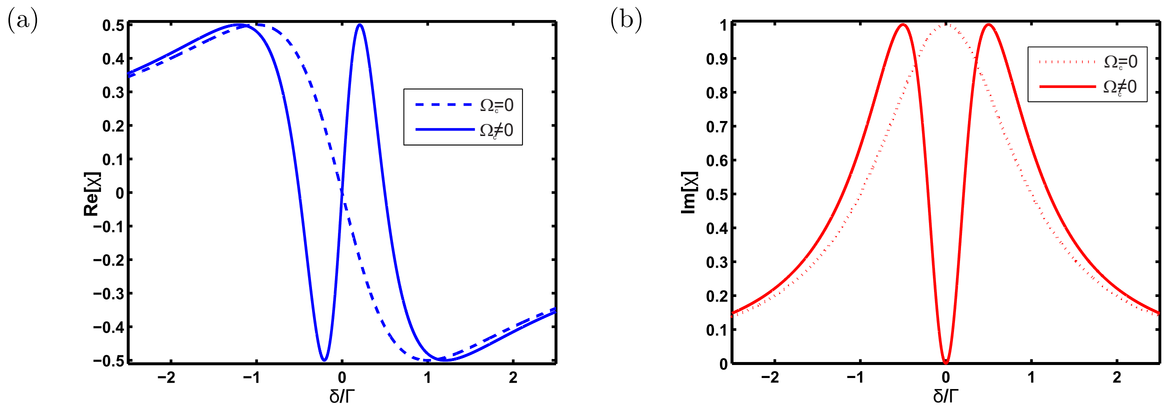

Figure 3.2: (a) Real and (b) imaginary components of the susceptibility χ on the $|b\rangle \Leftrightarrow |a\rangle$ transition both in the absence (dashed line) and presence (solid line) of the control field. It is in the latter scenario where EIT is observed.

Highlighting the characteristic features of EIT, one can see a transmission window more narrow than the two-level absorption profile in the imaginary component and the accompanying steep dispersion profile in the real component. A final feature, relevant to quantum memory applications, is the width of the transparency feature. Solving for this width one finds that

$$\mathrm{FWHM} = \frac{4|\Omega_c|^2}{\Gamma}, \tag{3.6}$$

and we see that the FWHM exhibits a linear dependence with respect to the control field power, and experimentally permits adjustment of the transparency window by means of simple intensity variation. It is important to realize that Equation (3.6) applies to non-Doppler broadened media. Under Doppler broadening, it can be found that the excited state relaxation rate increases such that $\Gamma \rightarrow W_d + \Gamma$, where $2W_d$ is the FWHM of the Doppler-broadened line. However, the form of the susceptibility remains unchanged in hot atoms [55]. We will further discuss the implications of Doppler broadening in Section 4.4.3.

3.1.2 EIT and slow light

With a description of how EIT behaves we now focus on how it can be utilized for quantum memory applications. The theory described above pertains to monochromatic electromagnetic plane waves, but interesting effects occur when pulses of particular bandwidth and mean frequency are subjected to EIT conditions. The group velocity for a propagating light pulse is given by:

$$v_g = \frac{\partial \omega}{\partial k}. \tag{3.7}$$

Using the relations for the wave number $k = \frac{n(\omega)\omega}{c}$, where $n(\omega)$ is the frequency dependent refractive index we can calculate the group index n_g as follows

$$n_g = \frac{c}{v_g} = n(\omega_0) + \omega_0 \frac{dn}{d\omega}\Big|_{w_0} \tag{3.8}$$

and the ensuing group velocity at the carrier frequency ω_0. We can immediately see in the relation that significant changes in the refractive index, such as those exhibiting a steep dispersion curve, will correspond to greater reduction in the group velocity. Furthermore, inspection of Eqns. (3.8) and (3.4) tells us that the group velocity increases with control field power under EIT conditions. The first demonstrations of this phenomenon reported a group velocity reduction by seven orders of magnitude with the observation of velocities on the order of 10 m/s [56, 57]. Since then this effect has been extended, with reports of the observation of double EIT and simultaneous slow-down of two probe fields [58]. A tradeoff naturally arises in these EIT systems: ideally the pulse will fit spatially inside a finite medium requiring both a large group velocity reduction and a short temporal length. However pulses of small duration correspond to larger spectral bandwidths which in turn will require larger EIT transparency widths (Eqn. (3.6)). Therefore, depending on the application, one usually sacrifices one of these attributes for the other. Most often this involves absorption of the high frequency components of the pulse which results in distortion.

3.1.3 Storage of light with EIT

If one were to encode some type of information into a light state (polarization, frequency, quadrature, etc.), one could in principle delay this information by passing the pulse through a medium under EIT conditions. However, for quantum memory applications we want to recall this light state on-demand, and to do so we must transfer this light state to the atoms themselves. When light travels through an EIT medium it becomes geometrically compressed by a factor $\frac{c}{v_g}$ and slows down. Initially the atoms are prepared in the ground state $|b\rangle$, but as the probe field enters the medium the frequency components of the light pulse are transferred to the atoms and a coherence is created between the ground states. The coherence formed between the ground states is called a spin wave. The probe pulse now has components both electromagnetic and atomic in nature and exists as a quasi-particle known as a *dark-state polariton* [59]. Note the ground state coherence, while often referred to as a spin excitation, generally does not store energy as most of the field energy is transferred to the control field and exits the medium via Stokes emission.

Through adiabatic intensity modulation of the control field we can mediate the transition of the probe field between its electromagnetic and atomic forms all while preserving the original coherence of the probe pulse. When the control field is turned completely off, the polarition exists as a pure spin wave of the ground states and only moves in accordance to the movement of the atoms. When the control field is turned back up, the polariton reverts back to a light pulse and accelerates away from the atomic medium. Hence, atomic media that, under the proper conditions, exhibit this polariton nature can serve as a storage medium, or memory, for light.

3.1.4 State of the Art EIT Memory

Electromagnetically induced transparency is one of the most, if not *the* most established system used for quantum memory. The first experimental demonstration of storage was reported by two independent groups. In the work of Phillips *et al.* [60] light pulses of 10-30 μs duration were stored in a Rb vapour cell for a duration of 200 μs with the magnetic sub-levels utilized as the ground states. The work by Lui *et al.* [61] was performed in a cold atomic cloud near BEC temperatures and used the hyperfine splitting of sodium as the grounds states to observe storage times near 1 ms. Later extensions moved to using hyperfine states in Rubidium [62, 63]. A study focused on improving EIT memory performance was developed by Gorshkov *et al.* in 2007 [64]. In that report, the temporal intensity profile of the control field was optimized for the best retrieval efficiency at a particular density of the atoms. Based on these findings, the same group achieved storage efficiencies of up to 42 % in a warm vapour of ^{87}Rb atoms [65, 66, 67]. Warm vapour EIT has also demonstrated its capability in storing images [68]. Other studies have pursued the implementation of EIT in solid state systems which are advantageous due to the possibility of significantly longer storage times. Using ion doped crystals, light was slowed down by a factor of 10^7 as well as stored [69]. This was followed up by the work of Longdell *et al.*, demonstrating the storage of light for a period of 2.3 s [70]. From a memory lifetime standpoint, storage times of greater than 1 s were observed in a Bose-Einstein condensate by the Hau group [71] and most recently, lifetimes up 16 s were presented by the Kuzmich group at Gatech [72]. Regarding quantum network applications, EIT has been demonstrated on the single atom level [73] which was followed up by single atom storage [74].

More pertinent to the theme of this thesis is the application of EIT for the storage of quantum light states. Studies have looked at the quadrature observables of continuous variable light states stored with an EIT medium [75]. The reduced variance of a squeezed vacuum was shown to be retained after propagation through a ^{87}Rb vapour cell under EIT conditions in both the CW [76] and pulsed regime [77]. The first successful experiment where the quantum nature of a light state was shown to be preserved after storage and retrieval using EIT was simultaneously achieved by two groups in 2005. Single photons resonant to Rb atoms were generated using a DLCZ protocol and stored for 500 ns in both a cold atomic cloud [78] and a vapour cell [79]. In both cases the single photon nature of the retrieved state was verified by measuring sub-Poissonian statistics at the output. In the continuous variable regime, squeezed vacuum was read in and out of memories in a warm vapour by our group [42] and concurrently by another group using a cold ensemble [80]. This same group extended this experiment to multiple sidebands storage using bi-chromatic EIT [81]. A significant advancement came in 2008 when for the first time an entangled light state in the form of a dual-rail single photon qubit was mapped in and out of a cold atomic ensemble [82]. Later polarization entanglement storage was achieved with the use of two cold atomic ensembles operating under EIT conditions which showed a postselected fidelity of 92% of the read out state [83].

3.2 csQPT of an EIT Memory

Up to this point we have described methods for characterizing quantum processes with csQPT and introduced the well established quantum memory scheme of EIT. We will now combine the two technologies with the goal of obtaining a reconstruction that can predict how an EIT setup will store and retrieve any arbitrary quantum input state.

3.2.1 Experimental Setup

We performed the csQPT procedure on an EIT-based memory with a system nearly identical to that used in Reference [42]. Our memory was realized in a warm vapour of isotopically pure ^{87}Rb atoms with 10 Torr of Ne buffer gas. The rubidium vapour was contained in a cylindrical glass cell with dimensions of 5 cm length and 25 mm diameter and was manufactured by Triad Technologies (Longmount, Co). To minimize losses experienced by the optical fields both input and output windows were anti-reflection coated. The cell was situated in a temperature-controlled oven system held constant at 65°C to achieve a sufficient optical depth with 3 layers of μ-metal shielding to eliminate any ambient magnetic fields in the laboratory setup. Buffer gas is a common feature in warm vapour EIT experiments in order to minimize spin-changing collisions and reduce the diffusion experienced by the atoms active in the EIT process. Further information about the effect of buffer gas in Rb vapour cells can be found in Section 4.4.4.

The probe field was set resonant to the $|{}^5S_{1/2}, F = 1\rangle \leftrightarrow |{}^5P_{1/2}, F = 1\rangle$ hyperfine transition ($D1$ line) at 795 nm and was produced by a continuous-wave Ti:Sapphire laser (Coherent MBR-110). The control field was produced via an external cavity diode laser (Toptica) phase-locked at the ^{87}Rb hyperfine ground state splitting of 6834.68 MHz red-detuned to the probe field. The locking was achieved via a homemade phase lock loop device [84]. It was found that optimal EIT was achieved with a probe field detuning of $\Delta_b = -630$ MHz (red detuning) and control field power of 5 mW. Both control and signal fields were spatially mode-matched to a beam waist of 0.6 mm while propagating through the rubidium cell. Under these conditions the FWHM of the EIT window was near 1.5 MHz. Probe and control fields were of orthogonal linear polarization allowing the convenience of combination and separation with the use of PBSs. The oven, PBSs, and mode-matched control field constituted our quantum process to be characterized as shown in Figure 3.3.

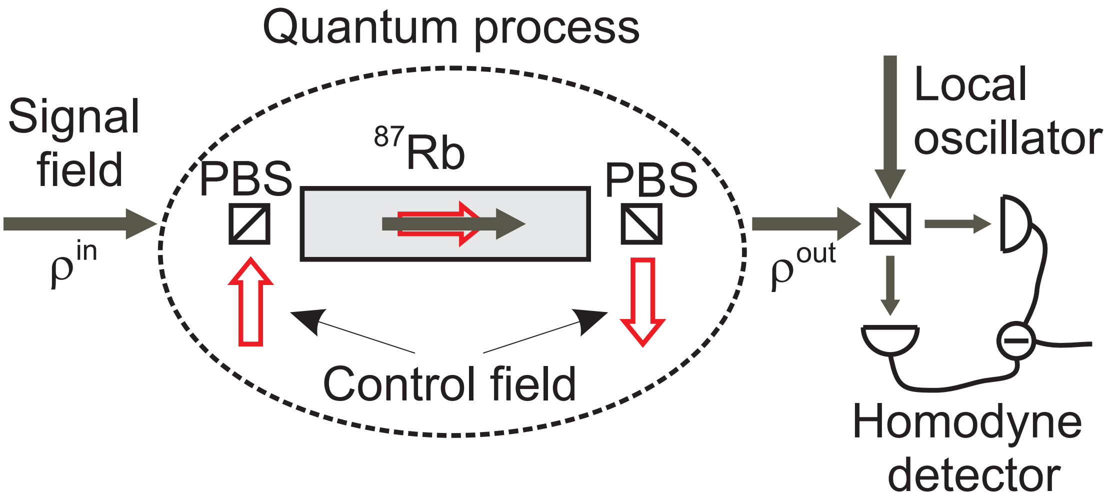

Figure 3.3: Schematic of the experimental setup used to characterize the process associated with the EIT quantum memory.

Input pulses subjected to the memory process had a top-hat shaped temporal profile of 1 μs duration and were produced with a pair of AOMs driven at 80 MHz. After the probe pulse entered the vapour cell, the control field was turned off to map the state of the pulse to an atomic spin wave. After a desired storage duration of τ=1 μs the control field was turned back on to retrieve the pulse from the memory (Figure 3.4).

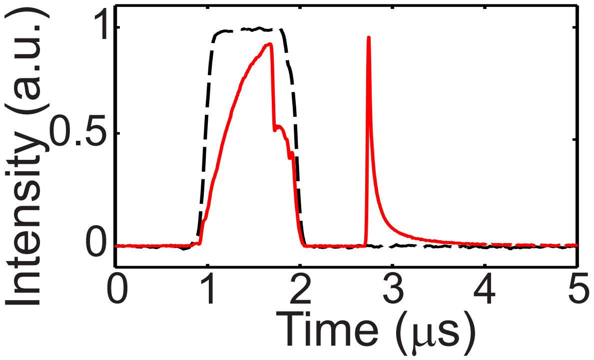

Figure 3.4: Example input pulse (black dashed line) and transmitted and retrieved light (red solid line).

We performed full quantum state tomography on the input, transmitted and retrieved fields with BHD. This was achieved by mixing input and output states with a local oscillator beam derived from the same laser as the probe field, as also depicted in Figure 3.3. To calculate the quadrature values, the homodyne current was integrated over the corresponding temporal mode (Sec. 2.4) which was obtained from the photodetector measurements shown in Figure 3.4. The entire storage and retrieval procedure was repeated at a repetition rate of 100 kHz. For every state, 50 000 quadrature values in the temporal modes of the input and retrieved pulses along with their corresponding phases were recorded with an oscilloscope. In order to both acquire enough data at all phase values in a practical manner the local oscillator was modulated with a ramp signal at about 7 Hz. Density matrices of both input and output states were reconstructed in the Fock basis by processing phase and quadrature values with a maximum likelihood algorithm (Section 2.4.1). Our memory was characterized using two different values of the two-photon detuning $\delta = \Delta_b - \Delta_c$, with δ=540 kHz and δ=0 kHz.

3.2.2 Results and Conclusion

To achieve an accurate characterization, we sent 10 coherent states $|\alpha_i\rangle$ of different real amplitudes α_i into the EIT memory system (our process $\hat{\mathcal{E}}$) with amplitudes ranging from 0 to 16.9. We measured the retrieved output $\hat{\mathcal{E}}(|\alpha_i\rangle\langle\alpha_i|)$ as well as the corresponding inputs in absence of the control field and vapour cell. Experimentally reconstructed input state Wigner functions resembled their theoretical form (Eqn. (2.17)) with fidelities greater than 0.999 up to $\bar{n} = 150$. Examples of experimentally reconstructed Wigner functions for the different two photon detuning conditions are shown in Figure 3.5.

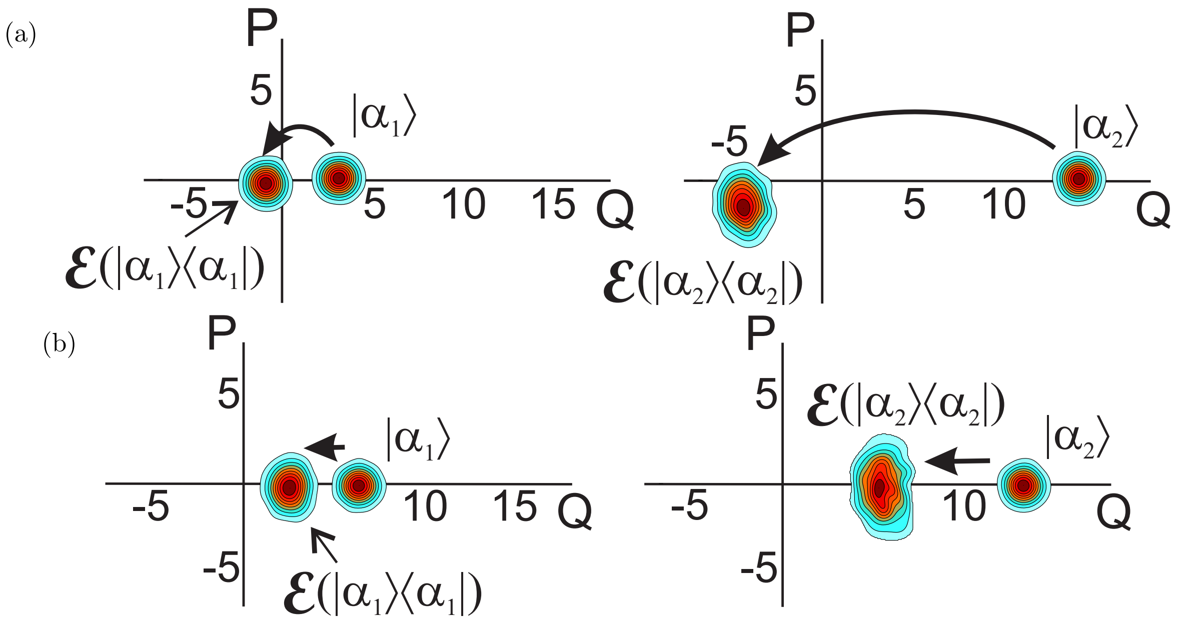

Figure 3.5: Wigner functions of input coherent states with two different amplitudes and the corresponding retrieved states $\hat{\mathcal{E}}(|\alpha_1\rangle\langle\alpha_1|)$ and $\hat{\mathcal{E}}(|\alpha_2\rangle\langle\alpha_2|)$. The input state amplitudes are (a) $\alpha_1 = 2.3$, $\alpha_2 = 10.3$ and (b) $\alpha_1 = 4.5$, $\alpha_2 = 10.9$ for the two photon detuning conditions of (a) δ=540 kHz and (b) δ=0 kHz.

Inspection of the above Wigner functions highlights the detrimental effects caused to the output states. A reduction of 0.41 ± 0.01 of the input amplitude was observed in the retrieved states for the case of two-photon resonance (δ=0) and was further reduced to 0.33 ± 0.02 for δ=540 kHz, corresponding to memory efficiencies of 17% and 9% respectively. In the case of non-zero two-photon detuning δ=540 kHz, measurements done with optical homodyne tomography and a standard photodetector exhibited differences in efficiency up to 14%. This is because the local oscillator frequency was not identical to that of the retrieved field, causing a chirping in the retrieved state and consequently reduced the time integrated quadrature values[1].

Secondly, the retrieved coherent states exhibit an increase in their phase quadrature

---

[1] We will see later that this value of δ was experimentally found to be optimal for the preservation of squeezed states.

variance. We attribute this noise to the phase lock used to lock the probe field, as we found it produced extra noise in the phase quadrature which is apparent from the ellipticity in the retrieved state Wigner functions (Fig. 3.5). Fluctuations of the relative phase between the control and probe field lead to a randomization of the phase of the retrieved state with respect to the local oscillator. Assuming the phase noise is Gaussian distributed with a mean of zero and variance σ_ϕ^2, we modelled the variance to increase quadratically with the input state amplitude as

$$\sigma_q^2 = \frac{1}{2} + \frac{q_0^2}{2}(1 - e^{-2\sigma_\phi^2}), \tag{3.9}$$

where q_0 is the mean quadrature amplitude. Fitting our experimental data via Eqn. (3.9) we find that $\sigma_\phi = 0.192$, which is in agreement with independent results [84] (Fig. 3.6).

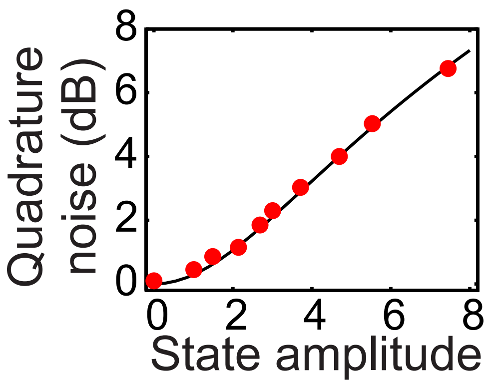

Figure 3.6: Variance of the retrieved phase quadrature as a function of the retrieved state amplitude.

The last detrimental effect to the memory comes in the form of population exchange between the hyperfine ground states [85, 77]. This is due to atoms moving in and out of the active memory region (beam waist) and results in both a reduced storage lifetime and the addition of spontaneously emitted photons in the retrieved state (extra noise). Additional photons uncorrelated to the probe field cause thermalization of the retrieved mode and consequently increase the output quadrature variance independent of amplitude and phase values. To quantify this extra noise, the storage and retrieval of vacuum states $\hat{\mathcal{E}}(|0\rangle\langle 0|)$ was studied. Under the two-photon resonance condition we found an excess noise of 0.185 dB in the quadrature variance corresponding to a mean photon number in the vacuum retrieved state of $\bar{n} = \mathrm{Tr}[\hat{n}\hat{\mathcal{E}}(|0\rangle\langle 0|)] = 0.022$. The noise showed a monotonic decrease with two-photon detuning until reaching a minimum value of 0.05 dB (corresponding to $\bar{n}$=0.005) for δ=540 kHz. It is for this reason that a non-zero two-photon detuning value was used despite its lower efficiency values. The presence of a nonzero two-photon detuning gives rise to a phase shift in the retrieved state with respect to the input, in this case $2\pi\delta\tau$=200° as can be observed in Fig. 3.5. The phase shift between the input and retrieved states was characterized by measuring the quadrature values corresponding to the transmitted and retrieved pulses in EIT conditions.

With this information available, we were able to reconstruct the superoperator $\mathcal{E}^{n,m}_{k,l} = \langle k|\hat{\mathcal{E}}(|n\rangle\langle m|)|l\rangle$ of the memory process, similar in fashion to what was done in [43]. Figure 3.7 shows the diagonal elements of the process tensor $\mathcal{E}^{k,k}_{m,m}$, where the colours correspond to the photon output distribution $|k\rangle$ for a given Fock state input $|m\rangle$.

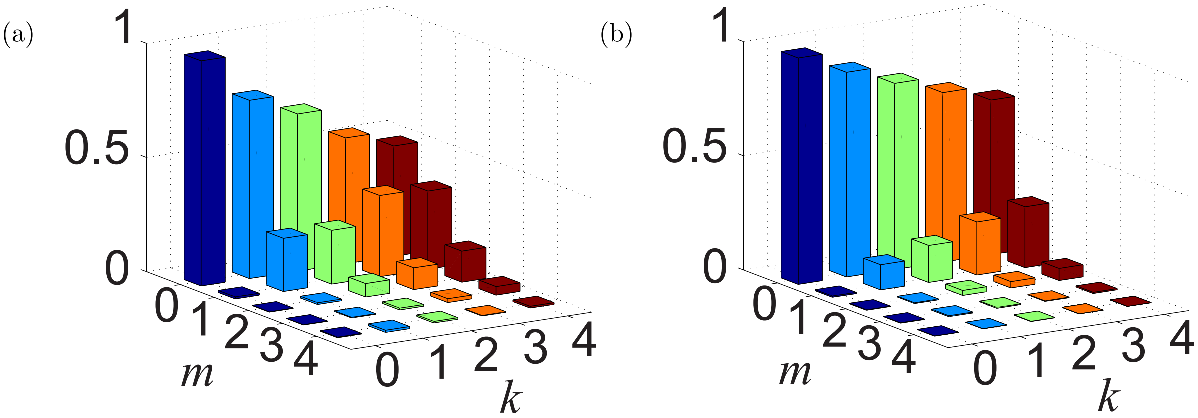

Figure 3.7: The diagonal elements of the process tensor $\mathcal{E}^{kk}_{mm}$ measured by csQPT in the Fock basis for (a) δ = 0 kHz and (b) δ = 540 kHz. Colours represent the output distribution for an input Fock state $|k\rangle$.

Analyzing Figure 3.7, we can see that the storage of vacuum, that is operation of the memory with the input channel blocked, results in mainly vacuum retrieval with a small component of higher number photon states due to extra noise. For a single photon Fock state, the retrieved state is a primarily mix of vacuum and one photon. Note the higher single photon component in the $\delta = 0$ case due to the higher efficiency (Fig. 3.7a).

As a final verification of the accuracy of the process reconstruction we applied the superoperator to squeezed vacuum states produced in our lab. Our squeezed state was created via a sub-threshold optical parametric amplifier and exhibited noise reduction in the squeezed quadrature of -1.86 dB and noise amplification in the orthogonal quadrature of 5.38 dB (the same as was used in Ref. [42]). Figure 3.8 compares the Wigner functions for experimentally measured retrieved squeezed vacuum states and those predicted with our csQPT characterization at both two-photon detuning conditions.

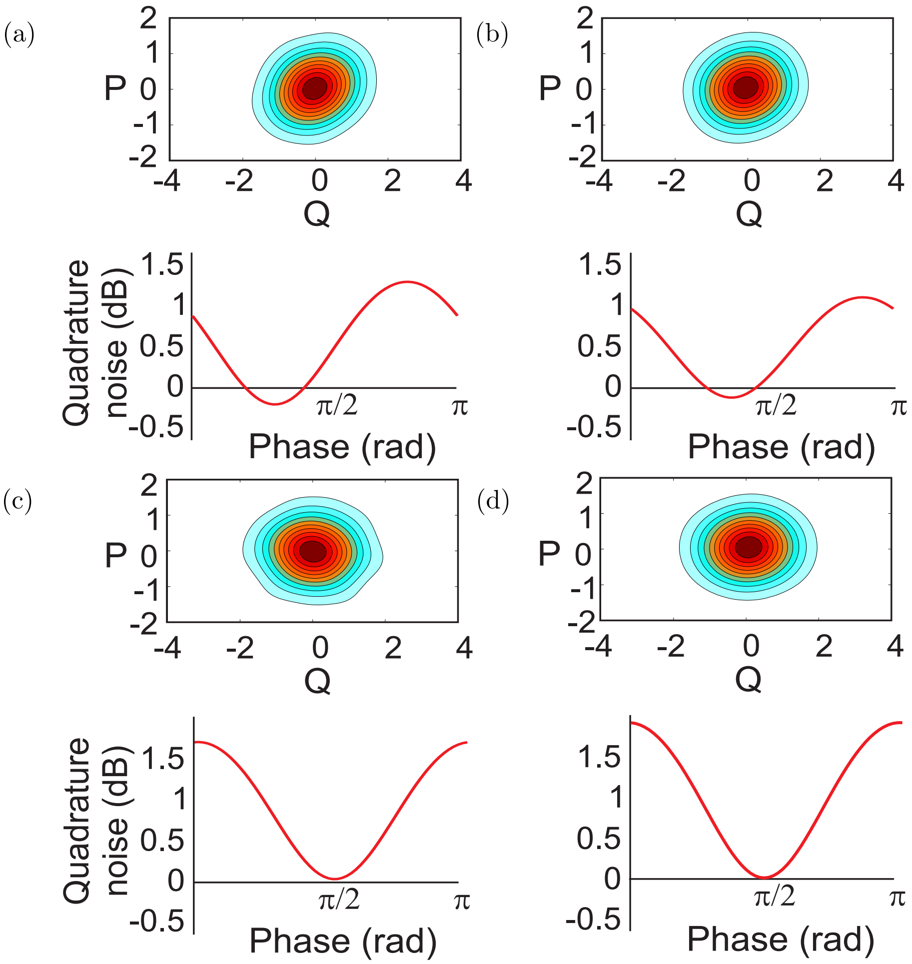

Figure 3.8: Comparison of the experimentally measured squeezed vacuum states retrieved from the quantum memory and those predicted with csQPT. Shown are the Wigner functions and the quadrature variance plotted as a function of the local oscillator phase. For δ= 540 kHz (a) experimental measurement (b) csQPT prediction and δ=0 kHz (c) experimental measurement (d) csQPT prediction.

We find quantum mechanical fidelities of 0.9959 ± 0.0002 for the two-photon detuning of δ=540 kHz and 0.9929 ± 0.0002 for the δ=0 case. Due to the lower amount of spontaneous photon scatter, and hence noise, we find δ=540 kHz to be better suited for the preservation of squeezed vacuum.

On a final note, this characterization procedure can also be used to estimate memory performance against any theoretical benchmark. As an example, the memory performance was analyzed with respect to the classical limit on average fidelity associated with the storage of coherent states with amplitudes distributed in phase space according to a Gaussian function of width $1/\lambda$ [1]. The limit of the fidelity as a function of λ is given by:

$$F(\lambda) = 2\lambda \int_0^{+\infty} e^{-\lambda\alpha^2} \langle\alpha|\hat{\mathcal{E}}(|\alpha\rangle\langle\alpha|)|\alpha\rangle \alpha d\alpha \leqq \frac{1+\lambda}{2+\lambda}. \tag{3.10}$$

From our measured data, we evaluate the average fidelity for our set of coherent states at both two-photon detuning values (Fig. 3.9). Both memory configurations show non-classical behavior, where the case of $\delta = 0$ corresponds to a higher average fidelity due to the higher storage efficiency.

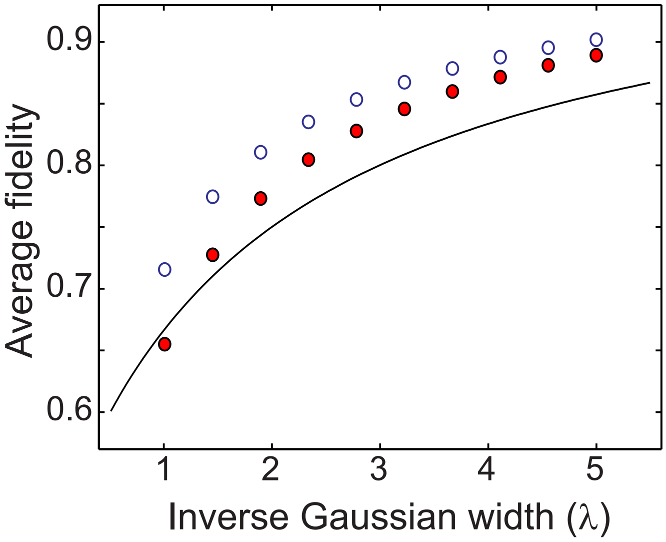

Figure 3.9: Average fidelity of the quantum memory for a Gaussian distributed set of coherent states. Blue empty (red filled) dots show the average fidelity calculated from the csQPT experimental data for δ=0 (540 kHz). The solid line shows the classical limit [1].

To summarize, we have demonstrated that our csQPT tool is capable of completely characterizing an EIT-based quantum memory system. Our characterization provides us with a “specification sheet” of sorts allowing prediction on any arbitrary quantum state prepared in the mode for which the process has been characterized. The reconstructed superoperators offer insight into device performance and possible feedback for optimization.

Chapter 4

Implementation of a Gradient Echo Memory System

In this chapter, we introduce and describe our implementation of a type of optical memory that has many variants, all of which belong to a class known as *photon echo memories*. Optical memories based on echo techniques in turn fall into the category of absorptive memories. The mechanism driving this type of memory scheme is the coherent absorption of light states by a medium, followed by a rephasing process in order to retrieve the light. We begin with a general overview of the underlying physics of how photon echo schemes work. This is followed by a description of the various photon echo techniques. We will then focus on a scheme known as Gradient Echo Memory (GEM) which we realized inside a warm alkali metal vapour and enables both highly efficient storage and can satisfy the criteria necessary for a quantum memory [86].

4.1 Fundamentals of Photon Echoes

4.1.1 Bloch Sphere

Any arbitrary pure superposition state of an isolated two-level system can be represented by a vector of unit length occupying the space known as the Bloch sphere (Figure 4.1), which is a common tool for describing the evolution of such systems.

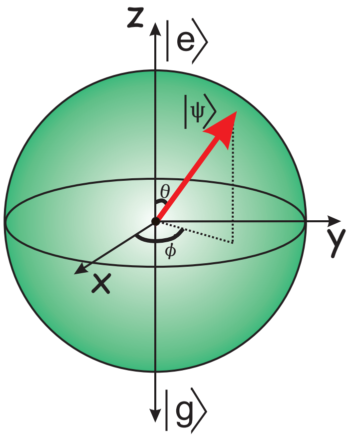

Figure 4.1: Bloch sphere representation of a two-level system. A pure superposition state is represented by a vector of unit length and is described by its polar and azimuthal angles θ, ϕ respectively.

Any pure state existing in this two-level system contains a unique mapping between its spherical polar coordinates and its wave function amplitudes:

$$|\psi\rangle = \cos(\theta/2)|g\rangle + e^{i\phi}\sin(\theta/2)|e\rangle \tag{4.1}$$

Inspecting Equation (4.1) we see that the probability amplitudes are related to the polar angles by $\cos(\theta/2)$ for the ground state $|g\rangle$ and $e^{i\phi}\sin(\theta/2)$ for the excited state $|e\rangle$. Convention is to define the z-axis to run through the top and bottom of the sphere which correspond to the excited and ground states respectively (Fig 4.1). The polar angle θ dictates the relative populations in each state and the azimuthal angle ϕ determines the relative phase shift between the states. In the case of an ensemble of single electron atoms, each atom has its own individual quantized spin and Bloch vector, however sometimes it is convenient to refer to the mean value of all these spins as a single Bloch vector representing the entire ensemble. This picture will be of benefit when describing photon echo schemes.

4.1.2 Basic Description

Consider an ensemble of two-level atoms that are inhomogeneously broadened, that is, each atom exhibits an emission spectrum detuned from all other atoms. This type of broadening is common to rare earth ions doped into crystals, where local electric fields are inhomogeneous resulting in a spectrum of Stark shifts within the crystal. If all atoms are initially in the ground state all Bloch vectors of the ensemble point along $-z$. We can then rotate these vectors by an angle θ about an orthogonal axis, the y-axis say, by applying an on-resonant pulse of duration τ such that $\theta(t) = \int_0^\tau \Omega dt = \Omega t$ where Ω is the Rabi frequency of the on-resonant pulse. A pulse of duration $\theta = \pi$, known as a π-pulse rather, will rotate the Bloch vectors 180° to the excited state which corresponds to an inversion of the population between the states.

To show an example of how these ensembles can be manipulated for generating photon echoes, we start with all our atoms in the ground state (Fig. 4.2a). By sending an on-resonant pulse into the atomic medium with duration such that $\theta(t) = \pi/2$, the ensemble evolves into a superposition of ground and excited states (Fig. 4.2b). Due to time evolution, the atomic population in the excited state will acquire a relative phase which corresponds to an ensemble Bloch vector rotation in the $x-y$ plane. Then as a result of the inhomogeneous broadening, each spin will precess at a different rate thereby causing them to "smear out" in the $x-y$ plane, or more succinctly the atomic coherence as a collective will *dephase* (Fig. 4.2c). If at a later time, a π-pulse is sent into the ensemble it will exchange the populations of the states which in our picture will flip the spins over the top pole of the Bloch sphere to the opposite side. The atoms will still rotate in the $x-y$ plane in their original direction which now will be back towards the $-y$-axis. Hence, the previous evolution has been effectively reversed in time. Another description is that the atoms that were previously in the ground state will be excited and will now undergo time evolution to acquire the same phase as the atoms that were initially excited by the

$\pi/2$-pulse causing a rephasing of the atoms (Fig. 4.2d). If the atomic dipoles dephased for a period of time τ before the action of the π-pulse, they will rephase at time 2τ after the initial $\pi/2$-pulse (Fig. 4.2e). At this point, the atoms will exhibit what is known as *collective emission* and emit an optical echo in the form of the original $\pi/2$-pulse.

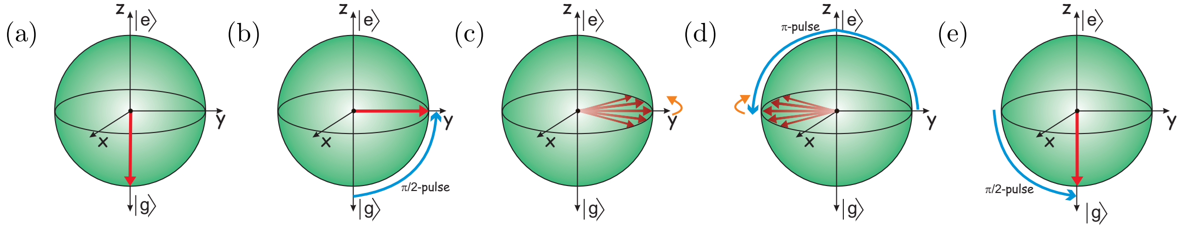

Figure 4.2: Bloch sphere representation of the two-pulse photon echo process. Initially all atoms are in the ground state (a) before absorption of a $\pi/2$-pulse excites the ensemble to a coherent superpostion state (b). Due to inhomogeneous broadening the spins will undergo dephasing (c). Absorption of a subsequent π-pulse will flip spins over the top pole of the Bloch sphere to the opposite side which triggers a rephasing of the spins (d), causing the emission of an echo $\pi/2$-pulse when the spins are once again in phase (e).

4.1.3 Phase-matching and Collective Emission

For a quantum description of the rephasing process, we start with an ensemble of N two-level atoms all of which are in the ground state such that the state of our ensemble is $|\psi\rangle = |g_1...g_N\rangle$. After absorption of a single photon on resonance at $t = 0$ the ensemble becomes a coherent superposition [87]:

$$|\psi\rangle = \frac{1}{\sqrt{N}} \sum_j a_j e^{-i(\delta_j t - i\mathbf{k}\cdot\mathbf{z_j})} |g_1...e_j...g_N\rangle. \tag{4.2}$$

This state corresponds to a single collective atomic excitation[1] also known as a Dicke state [88]. We see that the j^{th} atom in the ensemble will have a time-dependent phase

---

[1] In this case the Bloch vector of the ensemble will only undergo a miniscule polar angle rotation, contrary to the two-pulse photon echo case where $\theta = \pi/2$.

$e^{i(\delta_j t - i\mathbf{k}\cdot\mathbf{z_j})}$ where $\mathbf{z}_j$ is the atom's position and δ_j is its resonance frequency dictated by the inhomogeneous broadening. The ensemble will receive momentum $\hbar\mathbf{k}$, where $\mathbf{k}$ is the wave vector of the absorbed single photon (Note: a_j is the excitation probability of each atom). As time passes, the atoms will lose their coherence with respect to each other. By an effective reversing of the detunings, that is the introduction of a mechanism that causes $\phi = \delta_j t$ to be equal for all atoms at a later time, an echo in the form the original single photon will be emitted.

A remarkable feature is that the single photon echo will be emitted with the same wave vector as the original single photon $\mathbf{k}_{echo} = \mathbf{k}$, an attribute owed to phase-matching. Since all atoms have been imparted with the photon momentum $\hbar\mathbf{k}$, phase-matching is fulfilled when $\Delta\mathbf{k} = \mathbf{k} - \mathbf{k}_{echo} = 0$. At this point the amplitudes in Equation (4.2) interfere constructively which corresponds to a large probability amplitude for an emission event. Given that the well-defined retrieval direction allows for efficient optical readout, one can understand why these schemes are of great interest for practical applications [89]. Similar to the two-pulse photon echo, if the rephasing mechanism is introduced at time τ after the absorption of the single photon, the ensuing emission transpires at time 2τ. Note that in the phase-matching considerations of this process, the π-pulse used for rephasing would also need to be included in the phase-matching conditions. Similar analysis can be undertaken for storage in a three-level system involving read and write pulses, with any additional wave vectors included in the phase matching conditions. Note that in the example given for the single photon we assume a non-optical rephasing mechanism, we will discuss the specific mechanisms and techniques for rephasing in the following sections. Now that we have shown how inhomogeneous broadening is advantageous for light storage, in the next sections we will introduce the techniques in which it can be utilized.

4.2 Photon Echo Techniques and Results

4.2.1 Two and Three Pulse Photon Echo

In Section 4.1.2 we described the two-pulse photon echo scheme for storage of a $\pi/2$-pulse. While this protocol can preserve optical phase information [90] and is sufficient for storing classical data bits, it would not be of benefit for storing states holding quantum information that are typically composed of only a few photons. Due to the strong π-pulse necessary for rephasing, the large population transfer to the excited state results in spontaneous emission effects which will add noise to any retrieved quantum light state. Furthermore, this spontaneous emission would stimulate additional emission events causing an amplification process leading to the possibility of retrieval efficiencies greater than unity [91]. An extension to this technique is known as the three-pulse photon echo or stimulated photon echo which has the ability to store a series of data pulses. In the three-pulse scheme, an ensemble of two-level atoms are first prepared in a coherent superposition by sending in a strong $\pi/2$ "write" pulse of spectral width equal to or greater than the desired data rate. Then, a set of "data" pulses are sent into the medium which transfers the atomic coherence into a frequency-dependent population grating between the excited and ground states. To retrieve the data pulses, another strong $\pi/2$ "read" pulse is sent into the ensemble causing the atoms to rephase and emit echoes of the stored data pulses. This three-pulse scheme was also demonstrated to preserve phase information by using multiple readouts[2] to interfere the data pulses [92]. While this scheme may be adequate for the storage of classical optical data, due to spontaneous emission effects, the highest achievable fidelity is severely limited and such a scheme is not suited for quantum memory applications [93].

---

[2] This is possible due to the low efficiency of the protocol, allowing only fractions of the total excitation to be emitted at a given time.

4.2.2 Controlled Reversible Inhomogeneous Broadening (CRIB)

As the name implies, CRIB generates photon echoes by utilizing optically dense media that can be inhomogeneously broadened in a *controllable* manner. Upon absorption of a probe pulse, the dephasing process is reversed so that for each atomic detuning we get $\delta_j \to -\delta_j$. The first proposal for CRIB [94] called for a three level system in a Doppler-broadened vapour where it is the velocity distribution of the atoms that serves as the inhomogeneous broadening (See Fig. 4.3 for level structure). To begin, all atoms are optically pumped into the ground state $|1\rangle$. A probe pulse resonant with the $|1\rangle \leftrightarrow |2\rangle$ transition is then sent into the medium to be absorbed. Here, the spectral width of the probe would be large with respect to the homogeneous linewidth of the atoms but would be equal to or less than the inhomogeneous broadened excitation line. After absorption, the atomic mode will be similar to Equation 4.2 but now with multiple atomic excitations, and thus the atomic wave function will have a finite probability of existing in the excited state $|2\rangle$. Due to the inhomogeneous broadening, the dipoles formed by the excitation will dephase with respect to the portion of the ensemble remaining in the ground state. Within a time shorter than the lifetime of the $|1\rangle \leftrightarrow |2\rangle$ transition, the coherence of the atomic excitation can be mapped to another ground state $|3\rangle$ by means of a co-propagating π-pulse resonant with the $|3\rangle \leftrightarrow |2\rangle$ transition (Fig. 4.3).

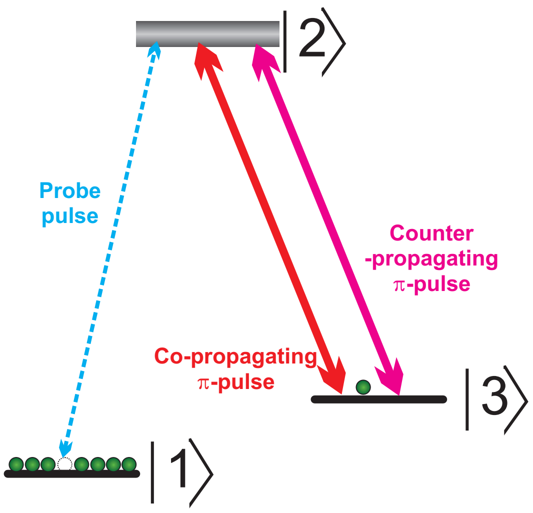

Figure 4.3: Doppler broadened three-level system suitable for CRIB. After absorption of the probe pulse on the Doppler broadened transition, a co-propagating π-pulse transfers the stored coherence from level $|2\rangle$ to $|3\rangle$ A counter-propagating π-pulse is used to reverse the dephasing for emission of an echo.

The ground states now hold the coherence of the original probe pulse. Application of another π-pulse in the counter-propagating direction will drive the probability amplitude of the atoms back to the excited state. Since the beam is counter-propagating, the Doppler shift relative to the first π-pulse will have the opposite direction, effectively reversing the inhomogeneous broadening causing the atoms to rephase. This operation gives a phase shift of $e^{-2i\mathbf{k}\cdot\mathbf{z}_j}$ to all excited atoms and the phase-matching conditions are satisfied by an echo emission in the backward direction. In this case, the echo will be a time-reversed version of the original probe pulse. For this scheme to generate near perfect time-reversed echos, the optical depth must be sufficiently large to achieve total absorption of the probe pulse and the atoms must exhibit little homogeneous broadening.

A later proposal for CRIB moved to solid-state systems with the frequency inversion accomplished via π-pulses and lattice defects serving as the source of inhomogeneous broadening [95]. In later proposals for CRIB [96, 97], and in its first experimental demonstration [98], the inhomogeneous broadening was inverted using externally applied electric field gradients. This technique is what the scientific community generally refers to as CRIB. A schematic diagram of the concept is shown in Figure 4.4. It starts with employing impurity ions that are doped into a rare-earth-ion-doped solid that is cooled to temperatures on the order of a few Kelvin. While the cooling will produce narrow homogeneous broadened absorption lines, imperfections in the host crystal lattice give rise to a large inhomogeneous broadening on the order of 10's of GHz that render the ensemble unsuitable for quantum storage in its current form (Fig. 4.4a). By using what is known as *hole-burning* to remove frequency classes of atoms to auxillary levels, one can manufacture a narrow transition line suitable for quantum storage (Fig. 4.4b). Controllable inhomogeneous broadening can be achieved by applying an external electric or magnetic field transverse to the direction of propagation of the incoming light fields. With sufficient broadening, an incoming light pulse will be absorbed by the ions and the coherence will be mapped to the atomic ensemble which then proceeds to dephase (Fig. 4.4c). After a desired time, the external field is reversed which flips the atomic detuning such that $\delta_j = -\delta_j$ and causes the atoms to rephase and emit photon echoes (Fig. 4.4d).

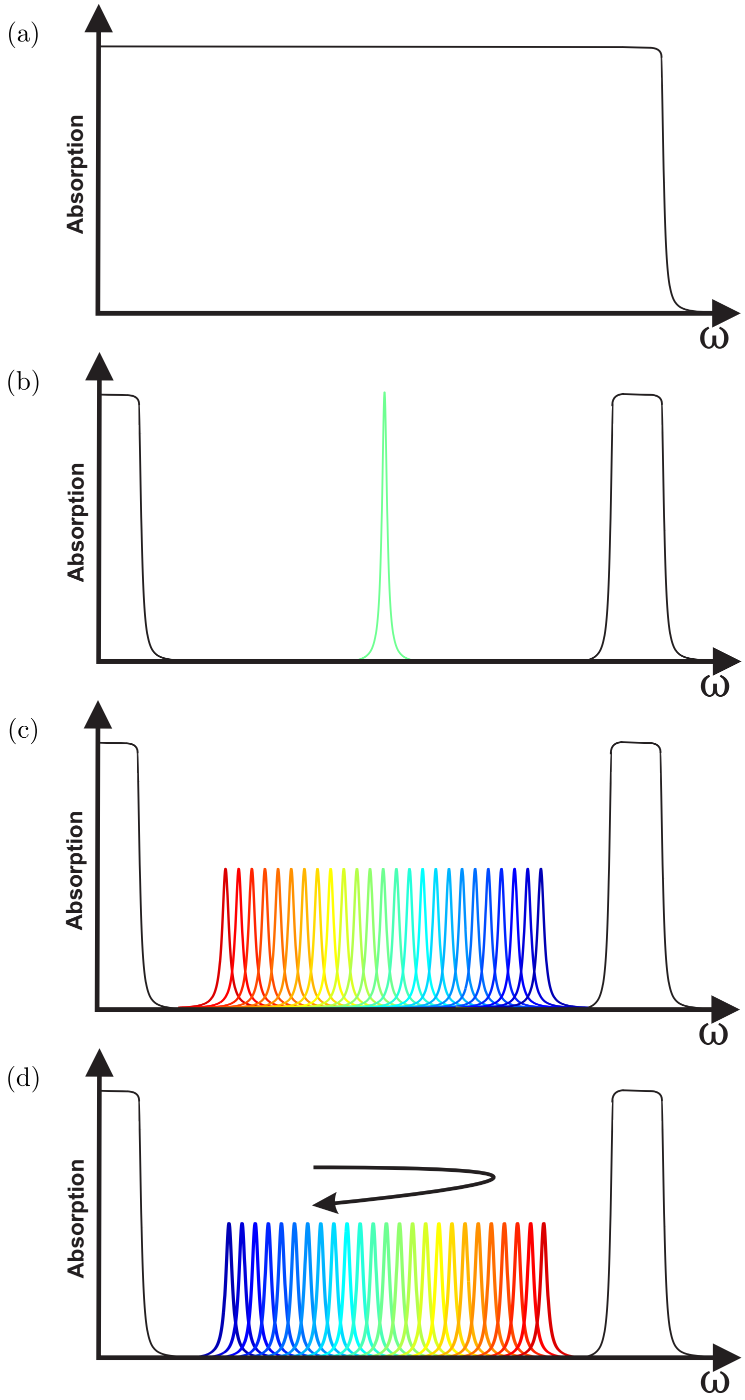

Figure 4.4: Hole burning and storage sequence for CRIB: (a) Initial inhomogeneous broadening. (b) Narrow spectral feature achieved with hole burning. (c) Broadened for absorption using an external electric field gradient. (d) After absorption the gradient is reversed to emit the echo. Figures adapted from Reference [2].

In the conditions just described, phase-matching conditions dictate that a time-reversed version of the absorbed light pulse will be re-emitted in the original forward direction. For a transverse or uniformly broadened medium, every slice along the pulse propagation axis will exhibit an identical absorption profile and as a consequence the re-emitted pulse is subjected to reabsorption. In a perfect system, this forward retrieval scheme has a maximum recall efficiency of 54% at a specific optical depth of $OD = 2$ [99]. However, similar to the first CRIB proposal, applying a position-dependent phase shift of $\exp(-2i\mathbf{k} \cdot \mathbf{z})$ to the entire ensemble will reverse the $\mathbf{k}$-vector in the atomic coherence which results in an echo emission in the backward direction. Using the backward retrieval procedure and a sufficiently large optical depth, unit efficiencies are theoretically possible [2]. Recent reports have proposed the use of these uniformly broadened CRIB based memories for quantum repeater applications citing their multimode potential [19] and their demonstrated capability for storage at the single photon level at telecom wavelengths [100].

A variation to the above scheme involves broadening the ensemble *longitudinally* along the direction of pulse propagation. With this type of broadening every slice of the ensemble will have a different detuning which circumvents any issues with reabsorption. Such a technique is closely related to the memory system implemented in this thesis and will therefore be left until Section 4.3.

4.2.3 Atomic Frequency Comb

A more recently developed echo memory is the atomic frequency comb (AFC) where, as the name suggests, the atoms used for storage are spectrally arranged in a comb-like structure. First proposed in Reference [87], and like CRIB, this memory is realized in rare-earth-ion-doped crystals that are cooled to liquid helium temperatures with the inhomogeneous broadening exploited for purposes of optical storage. By selecting ions of a particular level structure, one can first prepare all atoms in some auxillary hyperfine state $|aux\rangle$. Next, preparation pulses are used to transfer atoms into the ground state $|g\rangle$ at specific, uniformly spaced absorption sidebands. The absorption spectrum is then comb-shaped, with 'teeth' that are spaced spectrally by a chosen frequency δ. If an on-resonant light state is absorbed by this prepared ensemble at $t = 0$ the atoms will naturally rephase at times $t = 2\pi n/\delta$ where $n = 0, 1, 2, \dots$ and emit an echo due to collective emission. In other words, the storage time is pre-determined by construction of the comb teeth. The bandwidth of the memory is determined by the spectral range over which the comb is prepared. For example, with 20 comb teeth $N_p = 20$ spaced 5 MHz apart, the bandwidth of the memory is $\Delta = N_p\delta = 100$ MHz and will be capable of storing pulses of ~10 ns in duration with re-emission after 1.3 μs.

For a medium where the comb is prepared uniformly at every slice, similar to CRIB, the AFC protocol can reach efficiencies of 54% and 100% for retrieval in the forward and backward directions respectively. The absorption exhibited by the AFC is determined by the effective optical depth which is given by $d' = d/F$, where d is the optical depth of the atoms and F is the finesse of the comb (ratio of δ to the tooth linewidth). AFC is suited for highly multimode storage, with its multimode capabilities only dependent on the number of comb teeth N_p and completely independent of optical depth, an attribute in contrast to other memory systems [87, 101].

Experimental demonstration of AFC and its multi-mode capability was first reported in 2008 [102]. In that experiment, weak coherent states on the single photon level of 20 ns duration were re-emitted with an efficiency of 0.5% after a duration of 250 ns which was pre-determined by the comb spacing. Extensions to this protocol added the ability of on-demand read-out, a desired trait of any quantum memory [103, 104, 105]. This was achieved through transfer of the coherence to a second hyperfine ground state using two π-pulses, as a result the storage duration was increased to 10-30 μs. Improvements to the efficiency have been reported by using alternative ions [106], superior comb preparation techniques [107], and cavities to increase the optical path length [108].

In regard to the storage of quantum light states, AFC was shown capable of preserving time-bin entanglement by two groups simultaneously [109, 110]. These results were followed up by storing both rails of a dual-rail single photon qubit [111], storage of time bin qubits [112] and with some experimental modifications, polarization qubits were stored by three separate groups [113, 114, 115].

4.3 Introduction to Gradient Echo Memory (GEM)

Gradient echo memory is a variant of CRIB that was first demonstrated in an europium-doped crystal using longitudinal inhomogeneous broadening that was provided by external electric fields [98]. Contrary to transverse broadening, where every spatial location exhibits the same absorption profile, longitudinal broadening is along the direction of light propagation in the medium such that every spatial location exhibits a different detuning. The broadening is created with external and controllable fields such that the detuning of the atomic resonance of a two-level atom from the line centre is given, at position j, by $\delta_j = \xi z_j$ where ξ is the detuning per unit length (Fig. 4.5a). Upon absorption of a light pulse with bandwidth matching the broadening, the spectral components get mapped to different spatial locations along the medium (Fig. 4.5b). Then, identical to CRIB, by flipping the gradient $\delta_j \rightarrow -\delta_j$ the dephasing dipoles will begin to rephase followed by an echo emission (Fig. 4.5c).

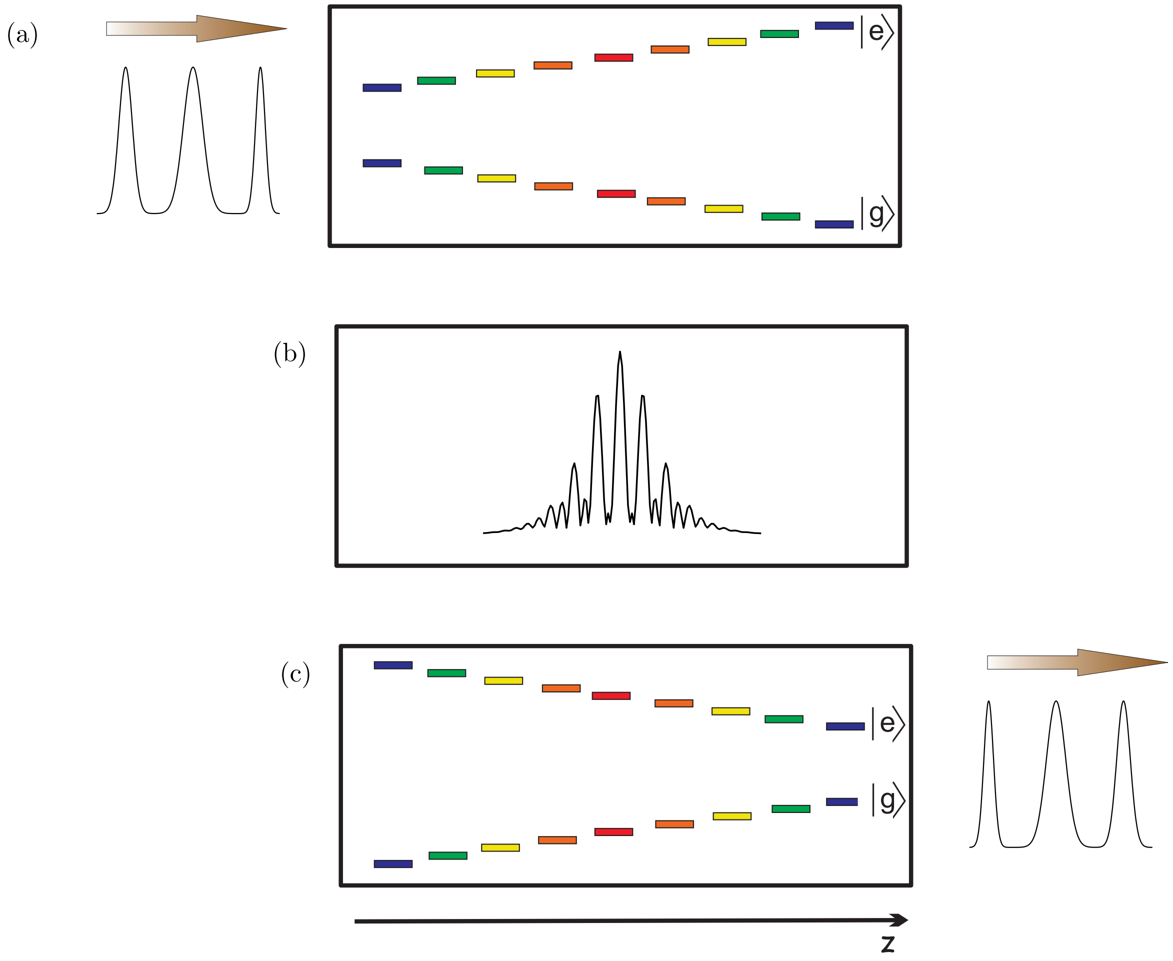

Figure 4.5: Optical storage using a GEM scheme with two-level atoms. (a) Medium is broadened along the direction of propagation for the incoming light pulses. (b) Spectral components are mapped to different spatial locations throughout the medium. (c) Upon reversal of the gradient, the dipoles rephase and emit a time-reversed copy of the input pulses. Figures are adapted from Reference [3].

In the Bloch sphere picture, we again start with all atoms in the ground state (Fig. 4.6a). After the absorption of a weak input pulse, such that $\theta \ll \pi/2$, the Bloch vector of the ensemble will undergo only a slight rotation along the polar axis (Fig. 4.6b). Just as in the case of the two-pulse photon echo, the atoms will dephase with respect to one another due to the broadening, this results in the spins "fanning out" from the Bloch vector of the ensemble (Fig. 4.6c). By reversing the gradient field, the spins will reverse their evolution and rephase (Fig. 4.6d). Due to collective emission, the ensemble will emit an echo of the input pulse which in this picture is represented by the ensemble Bloch vector rotating back to the ground state (Fig. 4.6e). Echoes will be emitted in the forward or backward direction depending on phase-matching conditions, in the former case the retrieved echoes are time-reversed copies of the original input [116].

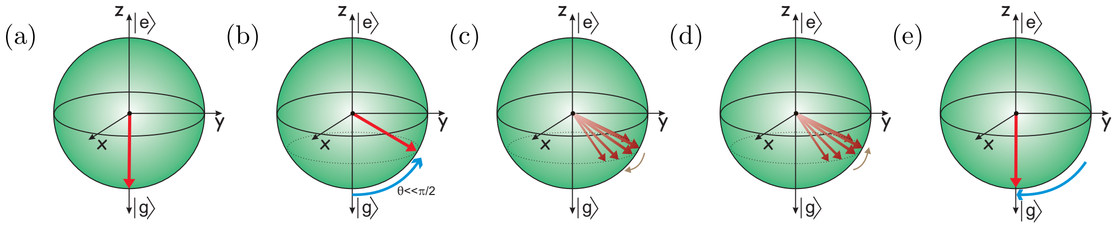

Figure 4.6: Bloch sphere representation of GEM. Initially all atoms are in the ground state (a). Absorption of a weak input pulse causes only a slight rotation of the Bloch vector; a larger rotation is shown in the figure for clarity (b). Due to inhomogeneous broadening of the ensemble, the spins will undergo dephasing (c). Reversal of the external gradient field will trigger a rephasing of the atoms (d), causing emission of an echo as a time-reversed copy of the input pulse (e).

For a more quantitative description of the dynamics of GEM, we can consider the Jaynes-Cummings Hamiltonian [117] for the interaction of a two-level atomic system with excited state $|a\rangle$ and ground state $|b\rangle$:

$$\hat{H} = -\hbar N \left[\delta \hat{\sigma}_{aa} + g(\hat{\mathcal{E}}^{\dagger} \hat{\sigma}_{ba} + \hat{\mathcal{E}} \hat{\sigma}_{ab}) \right] . \tag{4.3}$$

Here, N is the total number of atoms, $g = d\sqrt{\frac{\omega}{2\epsilon_0 \hbar V}}$ is the atom-light coupling, d is the dipole moment of the transition, and V the interaction volume. We want the detuning term δ to resemble our spatial gradient and therefore we make the substitution of $\delta \rightarrow$

$\delta(z) = \xi z$, with ξ being the gradient provided by the external field with units of frequency per unit distance. Since we work in the weak probe regime, it is assumed that almost all atoms begin and remain in the ground state such that $\sigma_{bb} \longrightarrow 1$. We now find the time evolution of the atomic coherence between the ground and excited state σ_{ba} by using the Liouville Equation and will simply add in a decay term Γ[3]:

$$\partial_t \sigma_{ba} = -(\Gamma + i\xi z)\sigma_{ba} + ig\mathcal{E}. \tag{4.4}$$

Also, we find the relevant Maxwell equation for the electric field amplitude $\mathcal{E}$ using the Heisenberg equation to yield

$$\partial_z \mathcal{E} = i\mathcal{N}\sigma_{ba}, \tag{4.5}$$

where $\mathcal{N} = gN/c$ is defined as the effective linear atomic density. For an atomic medium of length L that is centred at the origin, we can solve these equations analytically [118, 119] with respect to the beginning of the medium $z_0 = -L/2$ to arrive at the the following relationship[4]:

$$\ln\left[\frac{\mathcal{E}(z,\omega)}{\mathcal{E}(L/2,\omega)}\right] = \zeta(z), \tag{4.6}$$

with

$$\zeta(z) = i\alpha \ln\left[\frac{\Gamma - i(\xi z + \omega)}{\Gamma - i(-\xi L/2 + \omega)}\right]. \tag{4.7}$$

Here, $\alpha = g\mathcal{N}/\xi$ is the effective optical depth of our medium which exhibits a dependence on the broadening such that $\alpha \propto \xi^{-1}$. From Equation (4.6) it can easily be seen that the transmission amplitude can be calculated by

$$T(z,\omega) = e^{-\zeta(z,\omega)}, \tag{4.8}$$

---

[3] For simplicity we will concentrate on the most relevant concepts and thus the complete treatment of the Heisenberg-Langevin equations involving the noise operators is omitted. We will also omit the hat symbols.

[4] For the complete derivation of Equations (4.6) and (4.7) the reader is referred to Reference [118].

which can then be used to find the transmission intensity. By setting $z \rightarrow L/2$ we find an expression for the efficiency of our system which is

$$\eta = (1 - e^{-2\pi\alpha})^2. \tag{4.9}$$

From Equation (4.9) we can see that the efficiency of a two-level GEM system is a function of optical depth and that for large optical depths $\eta \rightarrow 1$ retrieval efficiencies of 100% are possible with both forward and backward retrieval procedures [119].

After the first demonstration of GEM in a two-level system using cryogenic rare-earth ions, it was followed up by the observation of efficiencies of 15% in 2008 [120], and then by the first demonstration of an unconditional quantum memory with a reported recall efficiency of 69% [121].

One final characteristic of this system worth noting is the case of high optical depth. In such a limit, the incoming probe pulses are slowed down while approaching the location of the original resonance frequency of the atoms. If the gradient is switched before the centre of mass of the pulse reaches this location, the resulting echo exhibits spectral components different from that of the incoming pulse. This phenomenon is known as a frequency chirp, and it will result in a degradation of the temporal mode fidelity between the retrieved mode with respect to the input. Experimentally, adjustments to the setup can alleviate this effect somewhat, such as fine tuning the central resonance of the atoms, but nonetheless achieving fidelities of exactly unity would be a challenging endeavour [122].

4.4 Λ-GEM system in Alkali Vapour

We now arrive at the system used in the current work, that is a GEM scheme realized in a warm vapour of alkali atoms. Such a scheme utilizes what is known as Raman scattering, but in relation to this thesis, this will be more conveniently referred to as

Raman absorption. In multi-level atomic systems interacting with multiple light fields we can have a variety of processes taking place. Of interest to us is the coherent interaction of a Raman transition, where two coherent light fields each off-resonantly couple a different ground state to a common excited state. In this way, the two-fields can stimulate a dipole-forbidden transition by passage through the excited state. This process lends itself to optical memory applications due to the long lifetime of the atomic coherence between the ground states.

4.4.1 Off-Resonant Atomic Interaction

To start, we will go over some of the off-resonant, two-field interaction properties of the atomic system. Not surprisingly, we begin with the same three-level system used for EIT that was shown in Figure 3.1 and the corresponding Hamiltonian given in Equation (3.1). Ignoring the decay terms for the moment, by direct application of the Schrödinger Equation one can solve for the population amplitudes. In the limit $|\Delta_c| \gg \Gamma, \Omega_c, \Omega_b$ we can use adiabatic elimination and approximate the excited state amplitude to be constant $\dot{\psi}_a \approx 0$. Thus we can solve for the evolution of the ground state probability amplitudes where we find that the system behaves as an effective two-level system comprised of only $|b\rangle$ and $|c\rangle$ with a corresponding Rabi frequency[5]:

$$\Omega_{\text{Raman}} = \frac{\Omega_c^* \Omega_b}{\Delta_c}. \tag{4.10}$$

While Equation (4.10) describes the population transfer, for any realistic situation we need to account for dephasing and decay as well. In order to derive an expression for the susceptibility we could use the same treatment as was used in Section 3.1 for EIT with the Lindblad formalism to formally calculate the evolution of the density matrix elements via a Master equation. Alternatively, we can instead turn to the more tractable

---

[5] For a more complete derivation of this result see Appendix A.

method of stochastic wave functions. In this approach, we develop a new Hamiltonian that is non-Hermitian by inclusion of the terms to model decay from both the excited $|a\rangle$ and metastable $|c\rangle$ state. The resulting non-Hermitian Hamiltonian can still be used in the Schrödinger equation provided that there is only a small probability of population exchange from either the excited or metastable state. Such an approximation is satisfied when there is a weak probe field such that the population in states $|a\rangle$ and $|c\rangle$ is negligible or the populations of the ground states remain constant [123]. With these constraints on the system, we can find the susceptibility of the probe-excited state transition to be of the form[6]:

$$\chi_{ab} \sim i\frac{|\Omega_c|^2/\Delta_c^2}{\gamma_{bc} + \Gamma(|\Omega_c|^2/\Delta_c^2) - i(\delta - |\Omega_c|^2/\Delta_c)}. \tag{4.11}$$

We can compare Equation (4.11) to the susceptibility corresponding to a two-level atom:

$$\chi \sim i\frac{1}{\Gamma/2 - i\Delta}, \tag{4.12}$$

and note that they are of the same form with the differences being the modified decay, shifted two-field resonance because of the AC-stark shift, and a correction to the optical depth by $|\Omega_c|^2/\Delta_c^2$. Equation (4.11) tells us the two-field resonance condition which dictates where the Raman absorption line appears: $\delta = \Delta_b - \Delta_c = |\Omega_c|^2/\Delta_c \rightarrow \Delta_b = \Delta_c + |\Omega_c|^2/\Delta_c$, as well as the effective width of the transition:

$$\Gamma_{Raman} = \gamma_{bc} + \Gamma\frac{|\Omega_c|^2}{\Delta_c^2}. \tag{4.13}$$

Equation (4.13) shows that the linewidth of the Raman transition scales linearly with respect to the control field power, which is a valid behavior in the regime $\Delta_c \gg \Omega_c$. By measurement of the FWHM of a series of Raman absorption lines as a function of the control field power, we can estimate the ground state dephasing term γ_{bc}. Note that

---

[6] A more comprehensive calculation for this equation can be found in Appendix A.

Raman absorption is insensitive to phase-matching between the fields as Equation (4.11) is only dependent on $|\Omega_c|^2$.

4.4.2 Analogy to a Two-Level System for GEM

We now move on to how this three-level system can be utilized as an effective two-level system suitable for GEM as described in Section 4.3. Starting with a similar interaction Hamiltonian as Equation (4.3),

$$\hat{H} = \hbar N \left[\Delta \hat{\sigma}_{aa} + \delta \hat{\sigma}_{cc} + g \hat{\mathcal{E}}^{\dagger} \hat{\sigma}_{ba} + \Omega_c \hat{\sigma}_{ac} + g \hat{\mathcal{E}} \hat{\sigma}_{ab} + \Omega_c^* \hat{\sigma}_{ca}) \right], \tag{4.14}$$

we use the Liouville Equation to find the time evolution of the operators corresponding to the coherence in the weak probe approximation such that $\sigma_{bb} \longrightarrow 1$. By once again simply adding in the terms for excited state decay Γ and ground state dephasing γ_{bc} we find the time evolution of the atomic coherences[7]:

$$\partial_t \sigma_{ba} = -(\Gamma + \gamma_{bc}/2 + i\Delta)\sigma_{ba} + ig\mathcal{E} + i\Omega_c \sigma_{bc} \tag{4.15a}$$

$$\partial_t \sigma_{bc} = -(\gamma_{bc} + i\delta)\sigma_{bc} + i\Omega_c^* \sigma_{ba}, \tag{4.15b}$$

with the Maxwell equation for the probe field amplitude unchanged from the two-level case:

$$\partial_z \mathcal{E} = i\mathcal{N}\sigma_{ba}. \tag{4.16}$$

As was done in Section 4.4.1, we use adiabatic elimination and approximate the excited state amplitude to be constant such that $\partial_t \sigma_{aa} \approx 0$ and $|\Delta_c| \gg \Gamma, \Omega_c, \Omega_b$ and with a transformation of variables our equations become:

$$\partial_t \sigma_{bc} = -(\gamma_{bc} + i\delta)\sigma_{bc} - i\frac{g\Omega_c}{\Delta}\hat{\mathcal{E}} \tag{4.17a}$$

---

[7] Once again for simplicity we will omit the Langevin noise terms and the hats.

$$\partial_z \mathcal{E} = i\frac{g\mathcal{N}\Omega_c}{\Delta}\sigma_{bc}. \tag{4.17b}$$

We have now arrived at equations similar to (4.3) and see that our Λ-system can be treated as an effective two-level system suitable for GEM. Following through on the same derivations from Section 4.3, we can reach a similar expression for the efficiency as Equation (4.9). The effective optical depth is now given by $\alpha = \frac{g\mathcal{N}}{\xi}(\frac{\Omega_c}{\Delta})^2$ which has an explicit dependence on both the control field power $|\Omega_c|^2$ and the detuning Δ.

The first observation of GEM in a vapour system was reported Reference [124] with subsequent publications in [125, 126, 86].

4.4.3 Doppler Broadening

With a basic description of Raman spectroscopy and how it can be utilized for GEM behind us we now move on to the other factors that require consideration when implementing such a system. Since our experiments employ a warm atomic ensemble, the effects of thermal motion must be considered. In Raman absorption, for an atom moving at velocity v with respect to the co-propagating laser beams, the two-photon resonance between the ground states will be shifted by [127]

$$\omega_{\text{Doppler}} \approx \omega_{bc}(1 + v/c). \tag{4.18}$$

For an ensemble of atoms we use a velocity distribution that is Maxwell-Boltzmann in form in all directions, then for the direction z which is parallel to the axis of beam propagation we have a velocity distribution v_z of

$$f(v_z) = \sqrt{\frac{m}{2\pi k_B T}} \exp\left[-\frac{m v_z^2}{2k_b T}\right], \tag{4.19}$$

where k_B is the Boltzmann constant, m is the mass of ^{87}Rb and T is the temperature of the ensemble. By inspection of Equation (4.19) we note that the standard deviation of the velocity distribution is given by $\sigma_{v_z} = \sqrt{k_b T/m}$. Along the direction of beam propagation we would observe the following changes in the detuning values due to the atomic velocity:

$$\Delta \to \Delta + \mathbf{k_p} \cdot \mathbf{v} \tag{4.20a}$$

$$\delta \to \delta + (\mathbf{k_p} - \mathbf{k_c}) \cdot \mathbf{v}, \tag{4.20b}$$

where $\mathbf{k_p}$ and $\mathbf{k_c}$ are the wave vectors of the probe and control fields respectively. At the temperatures typically used in this work (74°C), we would see average atomic speeds near 250 m/s in which case Equations (4.20a) and (4.20b) yield corrections of ~0.5 GHz and ~6 kHz for the single field and two-field detuning values respectively. Hence, Doppler broadening is significant for the single field detuning, as is apparent when observing spectroscopy of a single laser through a vapour cell. Contrarily, the effect of Doppler broadening is negligible in the case of two-field resonances with co-propagating fields. The effect of this broadening on the Raman absorption can be calculated by convolution with a Gaussian of width 6 kHz, which can be treated effectively as a delta function, and results in almost no broadening to the absorption profile for a far single field detuning[8].

4.4.4 Buffer Gas

Our glass rubidium vapour cells also contain a fraction of inert gases referred to as buffer gases. A relatively high concentration of buffer gas inside the vapour serves to dominate the collisions experienced by the Rb atoms resulting in the atoms to move in a diffusive manner oppose to the atoms undergoing ballistic collisions. This is an attractive trait for any coherence preserving ensemble. As a consequence, the atoms become restricted in their movement within the interaction region defined by the transverse spatial profile

---

[8] Given the dot product in Equations (4.20), a more rigorous calculation would involve also including the angular dependence between the wave vector and velocity vector of the atom.

of the light beams. The reduction of atomic movement reduces the effect of wave vector mismatch by a process known as Dicke narrowing [128]. Buffer gas collisions will also cause decay of the hyperfine excited states causing the transition to broaden. The collisional rate is a function of the buffer gas pressure, kinetic cross section between the Rb and buffer gas, temperature of the atoms and therefore their mean velocity. Collisional broadening values of the optical transitions that are relevant to our GEM system are Γ_{Kr}=17.1 MHz/Torr and Γ_{Ne}=9.84 MHz/Torr [129][9].

Movement of the atoms within the spatial profile of the light fields is an important consideration for any optical quantum memory, especially those employing warm atoms as a storage medium. However, in this thesis no explicit study of diffusion effects was undertaken.

4.4.5 Magnetic Fields

Rubidium is an alkali atom and therefore contains only a single valence electron. The number of possible transitions are determined by L-S coupling between the orbital L and spin S angular momentum of the electron which is known as the total angular momentum J. The total angular momentum $\mathbf{J} = \mathbf{L} + \mathbf{S}$ is conserved and the corresponding J values must satisfy the inequality $|L - S| \leq J \leq L + S$. Hence only two possible transitions exist: ${}^5S_{1/2} \rightarrow {}^5P_{1/2}$ for $J = 1/2$, referred to as the D1 transition at 794.979 nm and ${}^5S_{1/2} \rightarrow {}^5P_{3/2}$ for $J = 3/2$ referred to as the D2 transition at 780.241 nm. More important to this thesis, is the coupling between the the electron angular momentum J and the the angular momentum from the spin of the nucleus I. These two angular momenta couple to form the total nuclear angular momentum denoted by $\mathbf{F} = \mathbf{J} + \mathbf{I}$ and likewise any F

---

[9] Due to inelastic collisions with the buffer gas the hyperfine transitions also experience a shift in frequency, however this shift is < 1 kHz and is neglected in our studies [130].

quantum numbers must satisfy the relation

$$|J - I| \leq F \leq J + I. \tag{4.21}$$

In ^{87}Rb we have $I = 3/2$, and with $L = 0$ and $J = 1/2$ we have two possible hyperfine ground states with quantum numbers of $F = 1, 2$. Since we are only interested in the D1 transition we again have $J = 1/2$ and two possible hyperfine excited states $F' = 1, 2$. This yields four possible hyperfine transitions when observing the D1 spectrum of ^{87}Rb[10].

Delving further into the atomic structure, each hyperfine level F contains $2F+1$ sub-levels, denoted by the magnetic number m_F. These levels are degenerate in the absence of an external magnetic field, which is subsequently lifted in the presence of a B-field. With the quantization axis set by the direction of the B-field, most often the z-axis corresonding to the direction of light propagation, the m_F values are the z-components of the total angular momentum. The Hamiltonian describing the atomic interaction with the B-field is then:

$$H_B = \frac{\mu_B}{\hbar}(g_S\mathbf{S} + g_L\mathbf{L} + g_I\mathbf{I}) \cdot \mathbf{B} = \frac{\mu_B B_z}{\hbar}(g_S S_z + g_L L_z + g_I I_z), \tag{4.22}$$

where μ_B is the Bohr magneton and g_S, g_L, g_I are the Landé g-factors for the spin, orbital and nuclear angular momenta respectively. If the energy splitting due to the magnetic field is small compared to the hyperfine splitting such that $\Delta\text{E} \ll h\Delta_{hf} \approx h \cdot 7$ GHz then both J and F are good quantum numbers and thus:

$$H_B = \frac{\mu_B}{\hbar} g_F F_z B_z, \tag{4.23}$$

and the first order energy level split will be given by

$$\Delta E_{|F,m_F\rangle} = \mu_B g_F m_F B_z. \tag{4.24}$$

---

[10] The hyperfine energy shifts Δ_{hf} can be calculated using first order perturbation theory when considering the magnetic dipole moment of the nucleus [131].

The energy level splitting in Equation (4.24) is called the Zeeman effect and will be utilized in our system to break the degeneracy of the sub-levels and supply a broadened transition [131].

4.4.6 Four Wave Mixing and Gain

In any Λ-type energy level scheme with off- and near-resonant optical fields we have other mechanisms affecting the dynamics of the system. One of primary concern is the non-linear process of four-wave mixing (FWM). In our system, it stems from the fact that the strong control field needed for Raman absorption will off-resonantly couple both ground states in the Λ-scheme which opens up a two-way path for atomic population exchange as shown in Figure 4.7. This effect is detrimental to our Λ-GEM scheme for a number of reasons including our derivations for light storage (Sec. 4.4.2) that are reliant on the weak probe approximation $\sigma_{bb} = 1$.

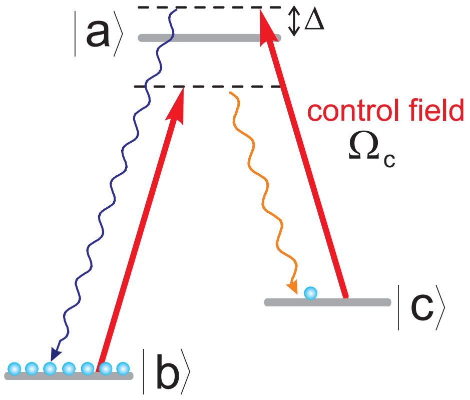

Figure 4.7: Atomic level diagram of a Λ-system highlighting how population can transfer via the four-wave mixing process.

From a qualitative viewpoint, not only does this process inhibit complete optical pumping of all population to a single ground state (ideal for GEM), but it also allows unintentional atomic population to occupy the "storage" ground state $|c\rangle$. The control field will then coherently transfer the unwelcome atoms in $|c\rangle$ back to the optically pumped state $|b\rangle$ which scatters noise photons into the mode of the probe field that are uncorrelated to the input state. When performing GEM, these additional photons can increase the signals measured in the retrieved mode with even the possibility of generating efficiencies greater than 100%! More importantly, this added signal will manifest itself as an increase in noise in accordance with the no cloning theorem [132].

A complete classical and quantum description of four-wave mixing can be found in Reference [133], however in relation to this thesis it provides little benefit to reproduce any of the derivations here. A generalized description of four-wave mixing consists of weak, off-resonant "signal" and "idler" fields that compliment the atomic interaction with the control field, all these fields together compose the *four waves* (Fig. 4.7). The presence of a signal field will create an idler field due to a $\chi^{(3)}$ non-linearity in the atomic system. Starting with the paraxial wave equation and imposing phase matching constraints one can derive coupled amplitude equations for the signal and idler fields. In the absence of an idler field, the intensity of the signal field I_s increases by a factor of $I_s(\zeta) = GI_s(0)$ where $G = \cosh^2(\zeta)$ is referred to as the gain and

$$\zeta = \frac{1}{2}k_s\chi\mathcal{E}_c^2 z. \tag{4.25}$$

Thus by Equation (4.25), amplification increases exponentially with the intensity of the control field $I_c = |\mathcal{E}_c|^2$. Pertinent to a Λ-GEM system is the case where there is no signal field present and it is in fact the vacuum fluctuations that stimulate a FWM process. From a quantum treatment of the problem it can be found that the mean photon number in the signal and idler modes is given by $\langle\hat{n}_s\rangle = \langle\hat{n}_i\rangle = \sinh^2(\zeta)$ with the noise of those added photons given by [133]

$$\langle\Delta\hat{n}_s\rangle^2 = \cosh^2(\zeta)\sinh^2(\zeta). \tag{4.26}$$

Hence, in our system under FWM conditions with no probe field present, the intensity and extra noise in the probe field channel should still increase exponentially with control field power.

4.4.7 Effect of Spatial Intensity Modulation

In all prior explanations of the behavior of our off-resonant Λ-system we took for granted that the optical fields were monochromatic and, more unrealistically, had infinitesimal spatial extent. Of course in practice all light beams will have some transverse profile of their intensity. Ideally, one would use Gaussian distributed intensity profiles in their beams, but due to experimental constraints (i.e. both high power and proper spatial filtering) this may not always be achievable. To investigate this, we simulate a spatially dependent intensity modulation on our control field to see the effect it has on the Raman absorption lines. We begin with a 1D Gaussian beam and include a weak, spatially dependent amplitude modulation such that

$$\Omega_c \to \Omega_c(x) = \left[\Omega_c + \epsilon\Omega_c \cos\left(\frac{2\pi x}{\omega_0/3}\right)\frac{1}{(\pi\omega_0^2)^{1/4}}\right] e^{-\frac{x^2}{2\omega_0^2}}. \tag{4.27}$$

We then substitute Equation (4.27) into an expression similar to that of Equation (4.7) and calculate the corresponding intensity transmission for different values of ϵ as shown in Figure 4.8.

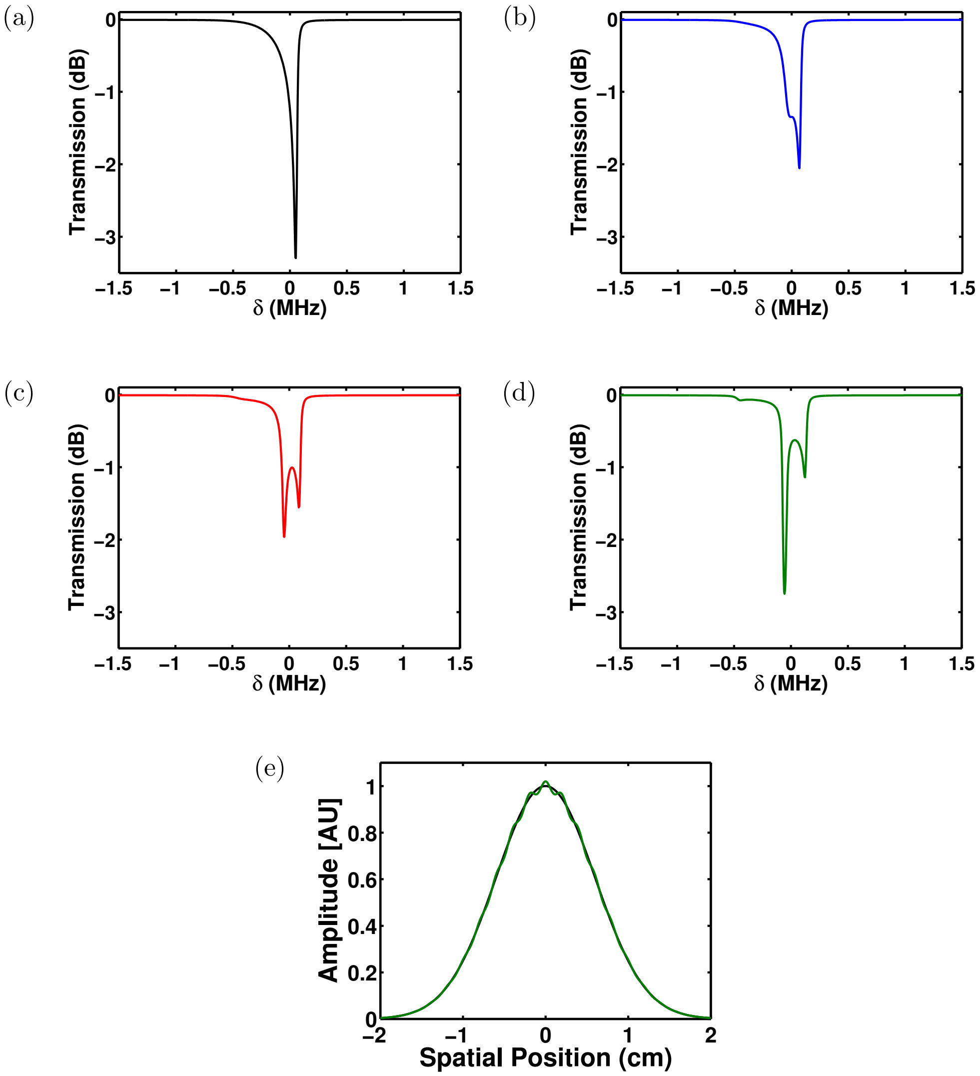

Figure 4.8: The effect of spatial amplitude modulation on the control field as it relates to the Raman absorption lines; (a) No modulation ϵ=0 ,(b) 0.005, (c) 0.01, (d) 0.02. (e) Amplitude profile of the control field with no modulation (black) and modulation of ϵ=0.02 (green). Parameters used in the calculations were Δ=1.3 GHz, $|\Omega_c|$=50 MHz, Γ=6 MHz, γ_{bc}=10 KHz, ω_0= 6mm.

Somewhat surprisingly, even with a small level of amplitude modulation applied we observe a drastic change in the shape of the Raman absorption profile. These results will be relevant to our measurements later on in this Chapter.

4.5 Experimental Implementation

Now that we have covered the theoretical framework for how a Λ-based GEM works, we now implement such a technology in the laboratory. Similar to the EIT experiments in Chapter 3, the memory was realized in a warm vapour of isotopically pure ^{87}Rb contained in cylindrical glass cells with anti-reflection coated windows affixed on both ends. The cells were manufactured by Triad Technologies (Longmount, Co). We used two different cells for observing GEM, the first with dimensions of 20 cm length and 25 mm diameter with 0.5 Torr of Ne buffer gas. The second had dimensions of 18 cm length and 25 mm diameter with 0.5 Torr of Kr buffer gas, similar to the vapour cell used in References [126, 86].

4.5.1 Oven & Coil Design

Cell Holders

Multiple issues needed consideration when designing an oven system suitable for a controllable GEM experiment. So much so, that an entirely new oven system, different from that used in the EIT studies (Ch. 3), was constructed for this experiment. To begin, the material encasing the cell is very crucial. Since we are interested in Raman absorption lines in warm vapours, we require stable control of temperatures up to at least 80°C. Furthermore, as discussed, in these Raman memories we exploit Zeeman splitting as the source of inhomogeneous broadening and need to invert the gradients quickly ($< 1\mu s$) to trigger the rephasing process before decay sets in. To that end, we require some material that not only exhibits good isothermal properties but does not generate any eddy currents that would prohibit a fast switching time. The solution was to use CPVC, an insulated material commonly used in plumbing pipes. This material has a melting point of 212°C, which is more than sufficient for our purposes and has the added bonus of being easily machinable.

Gradient Coils

In order to use Zeeman splitting as a broadening source we required both a uniform magnetic field and spatially dependent gradient field. The former is needed to break the degeneracy so that we can select a specific three-level system amongst the magnetic sub-levels that exhibits a weak-field Zeeman shift whose transitions are capable of being broadened. The latter imposes the gradient field to supply the inhomogeneous broadening. Not only do we want a high degree of control over the magnitudes of these B-fields, but we also want to be able to modify the gradient field in a simple and reproducible manner. For the gradient field, we developed a somewhat elegant solution. The cell holders were made in two sections that "cap" and enclose the cell at each end. Along the length of each cell holder, we designed a series of grooves comprised of "channels" of 2 mm depth and width that were separated by a 2 mm buffer space (Fig. 4.9).

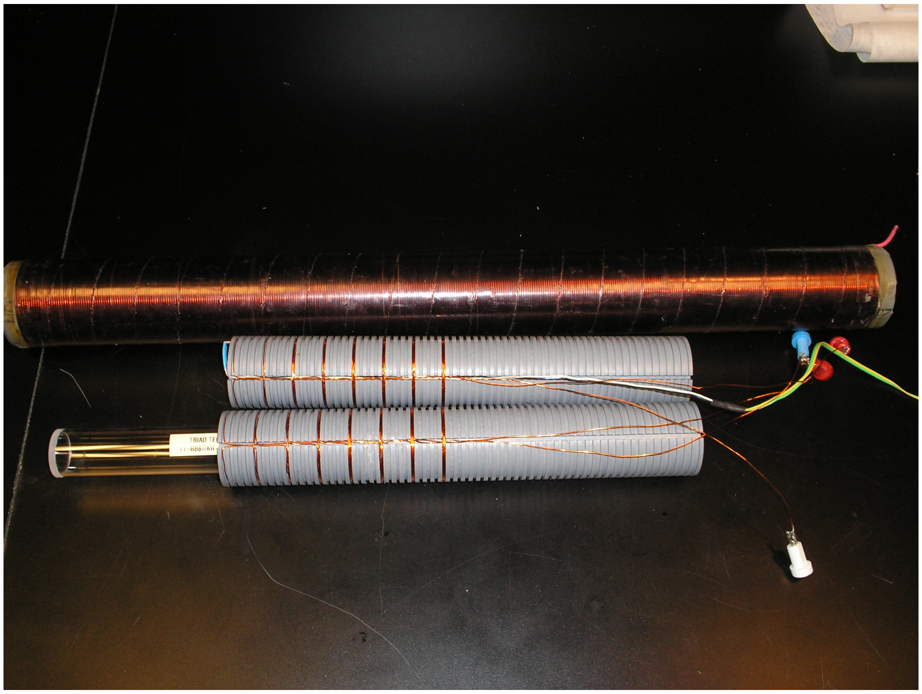

Figure 4.9: Uniform solenoid and gradient coils for housing the ^{87}Rb vapour cells used for GEM.

In this way we could create a variable-pitch solenoid by wrapping copper wire around the grooves with a number of turns of our choosing. A long channel along the length of the holders is used to run the wires to and from the centre of the cell. Using this design we engineered symmetric coil wrappings about the longitudinal centre of the cell. By running a current in opposing directions in each coil and connecting the coils outside of the oven we obtained magnetic fields that increased or decreased monotonically along the length to the vapour cell (see Fig. 4.13).

Uniform B-field

A uniform solenoid wrapped around a hollow tube made of the same CPVC material provided the uniform B-field. The tube also served to house the two cell holders (Fig. 4.9). To ensure uniformity of the field, the inside of the solenoid was measured to be uniform to within 0.3% over the length occupied by the vapour cell. We also calibrated the magnetic field as a function of the current through the solenoid (Figure 4.10).

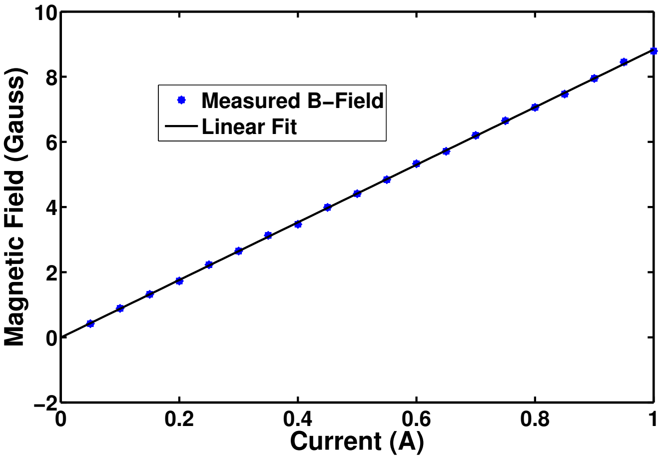

Figure 4.10: Magnetic field generated by the uniform solenoid as a function of the current in the coils.

A linear fit in Figure 4.10 gives a slope of 8.84 Gauss/A which will be useful for calibration of the magnetic sub-level splitting, typically ∼5 MHz for a current of 400 mA.

Oven

Magnetic shielding was necessary to remove the presence of any ambient magnetic fields that may affect the atoms. This was provided by a single layer, open-ended μ-metal sleeve that fitted tightly around the uniform solenoid / cell holder system. The sleeve was inserted inside a hollowed aluminum cylinder that held four resistive heating elements used to heat the cell to the desired temperature. A second uniform solenoid was wrapped outside the heating cylinder for purposes of de-Gaussing the μ-metal sleeve. To provide insulation from the outside environment the aluminum heating system was "propped up" inside another hollowed aluminium cylinder with a 1.5 cm air gap between the two cylinders. The uniform solenoid and oven had a length of 52 cm to eliminate any possibility of fringing magnetic fields at the ends of the vapour cell. A platinum resistance temperature detector (RTD) probe (PT 100 OMEGA) was inserted in the cell holders near the centre of the vapour cell and was controlled with a Wattlow PID control circuit to attain accurate temperature readings. Temperatures were kept stable within a precision of 0.1°C.

4.5.2 Magnetic Field Switch

One of the most vital components to a Λ-GEM system that utilizes Zeeman splitting, such as ours, is a device capable of reversing the magnetic field gradient quickly and smoothly. It is imperative that the direction of the current running through the coils can be reversed much faster than the decay of the ground state coherence. Additionally, the ideal switch will reverse the current monotonically over the switching time, in other words the magnetic field will not exhibit any type of ringing behavior that could be detrimental to the rephasing process. A relatively simplistic design was employed for our purposes which consisted of two current supplies, two power MOSFETS, a power resistor and a polyester-film-type capacitor. A schematic diagram of our design is shown in Figure 4.11.

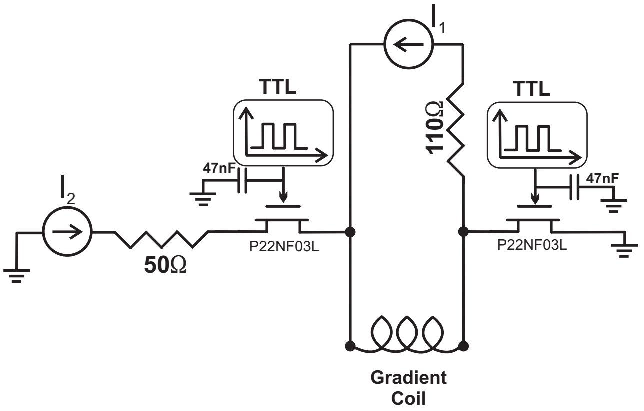

Figure 4.11: Schematic diagram of the magnetic field switch.

Referring to Figure 4.11 the main operation of the switch is as follows: current source I_1 is left on at all times during the storage and retrieval procedure to provide an "offset" magnetic field, current source I_2 is gated on and off by the MOSFETS which controls the storage and retrieval. In this design, the power MOSFETS (P22NF03L) have a switching time of ~20 ns and the gate voltage is supplied by a pulse/delay generator (BNC Model 565). When the gates are on as controlled by the TTL, a bias voltage is set such that the current source I_2 provides a magnetic field gradient that gives the desired amount of broadening. Note that the current I_2 is set with the current I_1 already present in the coils. Then when the gate is switched off, only the offset current source I_1 is present, it is this current that provides the reversed gradient. An example showing the ideal scenario is given in Fig. 4.12, where Curve A (black) gives the magnetic field due to the current I_2 in absence of the current I_1. Curve B (red) gives the resulting magnetic field with both currents I_1 and I_2 present in the coil, this is the gradient used for the absorption and corresponds to the period when the MOSFETS are gated on. Finally, Curve C (green) is the magnetic field due to current I_1 which supplies the gradient field used for rephasing of the dipoles.

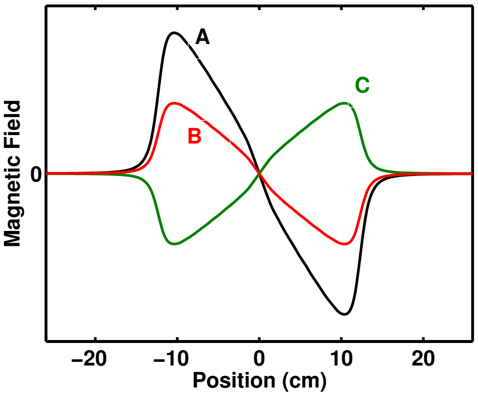

Figure 4.12: Magnetic field gradients as they refer to the operation of the current switch shown in Figure 4.11.

The coil by itself, with a small, but finite amount of resistance acts as a LR circuit, where L is the inductance and R is the resistance. When the circuit is effectively disconnected from a power source, such as when the gates are shut off, the zero input response (ZIR) of the circuit is given by

$$I(t) = I(t=0)e^{-\frac{R}{L}t}, \tag{4.28}$$

where the time constant of the circuit is given by $\tau = \frac{L}{R}$. Therefore the time it takes for the current to decay can be decreased by both increasing the resistance and decreasing the inductance of the coils. While the gradient coils are not a uniform solenoid, the expression for the inductance of a solenoid is still useful for optimizing the switch:

$$L = \mu_0 \frac{N^2 A}{l}. \tag{4.29}$$

Here N is the number of turns, A is the area of the solenoid cross-section, and l is the length of the coil. Given the geometry of our gradient coils, the lowest inductance is achieved using the lowest number of turns N in the solenoid. For this reason the solenoid was wrapped only long enough such that the magnetic field was monotonic over the length of the cells. In both cell holders, every 4^{th} groove was wrapped with an incremental number of turns from 1 to 8 as one moved away from the centre of the vapour cell. Given the spacing between grooves this yielded a total solenoid length of 2 x 11.5 cm = 23 cm. A test with a LC circuit found the inductance of the coils to be 6 μH which is consistent with that used in other experiments [134]. The magnetic field as measured along the length of the gradient coils is shown in Figure 4.13.

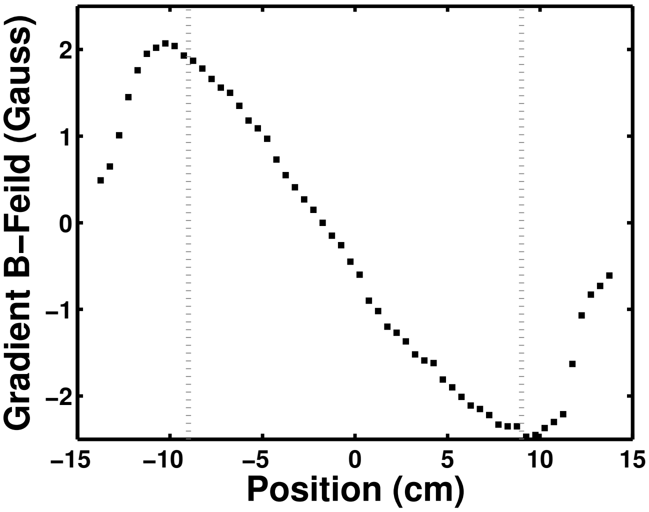

Figure 4.13: Magnetic field generated by the gradient solenoid along the length of the vapour cell with a current of I =500 mA. The area between grey dashed lines denote the position of the 18 cm long cell.

In regard to the resistance, we found using a power resistor of R = 110 Ω provided the optimal switching time. The final consideration was that the LR circuit exhibited a ringing behavior when the current source I_2 was gated off. To alleviate this problem we connected a capacitor to ground (shown in Figure 4.11) to sufficiently smooth out the ringing effect in exchange for an increased switching time as a compromise. We found a capacitance of 47 nF to be suitable for our purposes. With these parameters we measured a 10%-90% switch time of 450 ns which is much less than the inverse width of the Raman line used for storage. Figure 4.14 shows the response of the switch with and without the capacitor present.

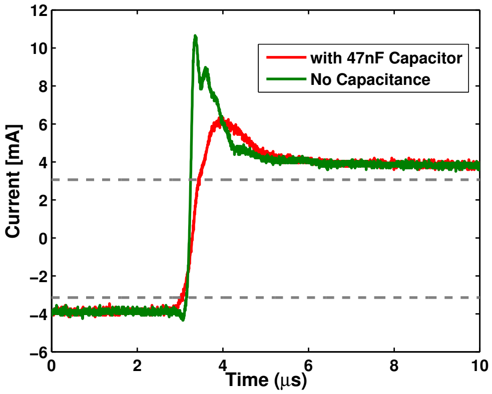

Figure 4.14: Current during the switching procedure as measured using the voltage drop through a 2 Ω resistor connected in series with the solenoid. Without the capacitor, a switching time of <100 ns was observed with a ringing effect. The ringing was sufficiently alleviated with a capacitor which increased the switching time to 450 ns.

4.5.3 Optical Setup

Laser Fields

The full experimental layout is shown in Figure 4.15.

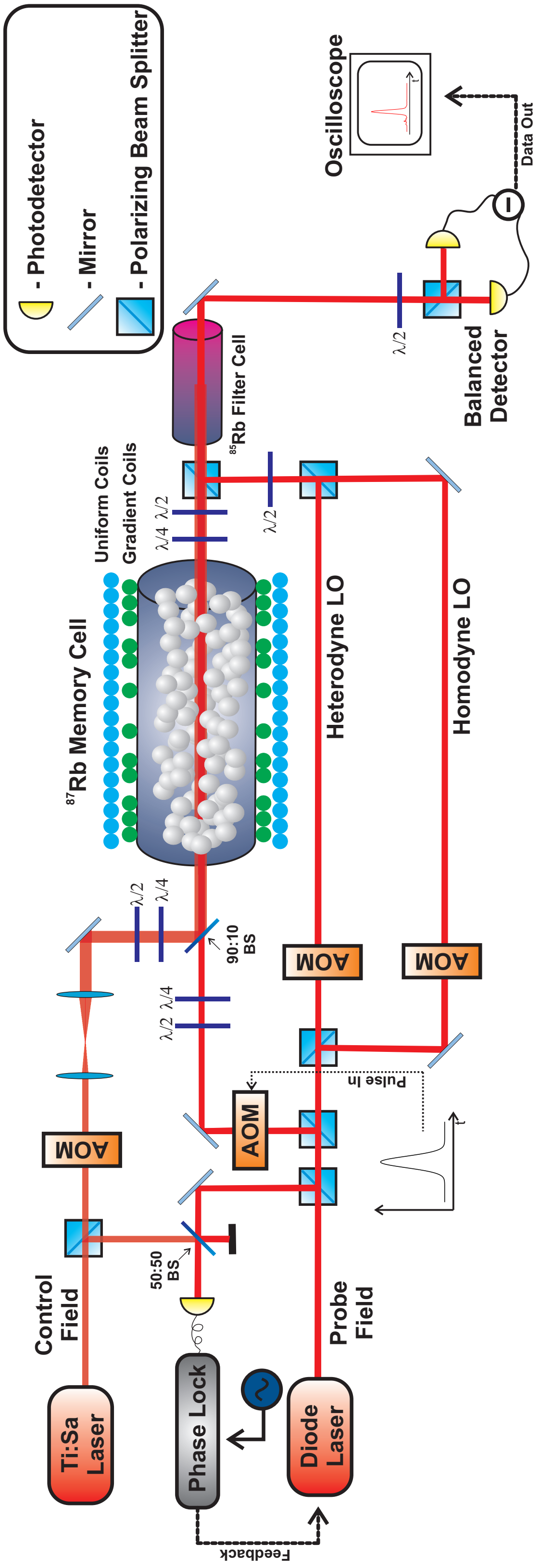

Figure 4.15: Schematic diagram of the experimental setup.

The control field was derived from a continuous-wave Ti:Sapphire laser (Coherent MBR-110) with a linewidth <100 kHz and was tuned to 795 nm on the D1 transition of ^{87}Rb. This allowed fine control over the desired off-resonant detuning Δ_c. For our experiments the control field was typically blue-detuned by Δ_c=1-2 GHz from the $|^5S_{1/2}, F = 2\rangle \leftrightarrow |^5P_{1/2}, F' = 2\rangle$ transition. The probe field used for storage was produced by a homemade external cavity diode laser (ECDL) and was phased-locked near +6.83 GHz (^{87}Rb ground state splitting) to the control field using a homemade phase lock loop (PLL) circuit [84]. The locking frequency was adjusted to the two-field resonance condition (δ=0) of the split magnetic sub-levels using a reference signal sent into the PLL. The two-field interaction of these lasers created a Raman absorption line at the blue-detuning value Δ_c of the $|^5S_{1/2}, F = 1\rangle \leftrightarrow |^5P_{1/2}, F = 2\rangle$ transition. Near-Gaussian pulses were generated by use of an AOM in conjunction with temporal modulation of an 80 MHz sinusoid via a voltage variable attenuator (VVA).

Field Combination

The GEM scheme for optimal efficiency used co-rotating circular polarized light fields [126, 86]; as a consequence, combining the laser fields for entry into the memory cell in a lossless manner is a non-trivial task. Lossless combination is essential if one were to store non-classical light states, since any loss will increase the vacuum component of any statistical mixture. Prior implementations by other research groups combined the fields with the use of ring cavities that required both design and external locking [86]. For our purposes, we only operated the memory on coherent states and therefore, in our studies were not concerned with any losses experienced by the fields *before* entrance into the memory cell. Hence, combination of the fields was attained using a 90:10 beam splitter and both control and probe field had their individual set of waveplates for optimal control over the optical polarizations.

Control Field Filtering

After operation of the memory, in order to detect any signal field, especially those on the order of a few photons, the control field must be extinguished to a satisfactory level. Since the probe and control field are of, or close to, identical polarization during the storage operation, any type of polarization filtering cannot be taken advantage of. Therefore, an alternative form of filtering, such as exploiting the frequency difference, was necessary. A possible solution would be to place a ring or Fabry-Perot cavity after the memory cell, the drawback of these methods is that they are best implemented with active locking using external laser fields. Alternatively, one could use monolithic Fabry-Perot cavities manufactured out of high-reflection-coated lenses such as those reported in Palittapongarnpim *et al.* [135]. The monolithic design is attractive, as it allows resonance tuning and stabilization using only temperature controls. Devices such as these have proved highly beneficial in experiments requiring a high degree of filtering [13]. The shortcoming of these devices is that the top coupling efficiencies are typically only $\sim 50\%$ which is not ideal for continuous variable quantum memory applications.

The best method, and the one implemented in this experiment, is the use of a pure ^{85}Rb vapour cell after the memory cell. With a detuning of Δ_c=1-2 GHz, the pump field was near resonant to the $|^5S_{1/2}, F=2\rangle \leftrightarrow |^5P_{1/2}, F=2,3\rangle$ ^{85}Rb transition and by heating the cell to a sufficient temperature, the strong control can be absorbed while the far off-resonant probe field is mostly transmitted. For our purposes we used an isotopically pure ^{85}Rb cell of dimensions 10 cm length and 25 mm diameter with anti-reflection (AR) coated windows to minimize loss. The cell was situated in a temperature-controlled oven primarily constructed out of aluminum with a RTD probe connected to a Wattlow PID system. The filter cell was maintained at $\sim$115°C to provide sufficient extinction of the control field at the desired detuning. At this temperature we typically observed a control field extinction of $\sim$55 dB and probe field transmission of 85%. To help reduce any condensation build-up on the cell windows, a hole was drilled into the top of the oven system so that an air hose could be used to create a cold spot on the cell walls in an area unaffected by beam propagation.

Detection

With sufficient filtering achieved, we now aimed to detect the light states retrieved from the memory apparatus. We did this using two types of balanced detection, namely heterodyne and homodyne (described in Section 2.3.2). The oscillator beams used for both detections were derived from the laser generating the probe field. For heterodyne detection, the oscillator beam was modulated at 74.9 MHz (generating a 5.1 MHz beat note) using an AOM and was mixed with the probe field after the memory process by means of a polarizing beam splitter (PBS). The light fields were mixed before the filter cell to offset the effect of wave vector fluctuations caused by the high temperature of the cell (as shown in Fig. 4.15). If the fields were mixed after the vapour cell, the recorded probe field signals exhibited fluctuations sizeable enough to render our measurements imprecise. At too high of filter cell temperatures, these signal fluctuations were unavoidable, which placed a maximum on the temperature we could set the filter cell to. Typically, visibilities of 97% were achieved between the probe field and the oscillator beams. Detection was realized with a half-waveplate-PBS combination with the beams in the output port impinging upon a balanced detector (Thorlabs PDB150A) operated at a 3 MHz bandwidth. In heterodyne detection, the RF output signals were monitored on a spectrum analyzer operated in the time-domain at the 5.1 MHz beat frequency. This detection scheme was used for the classical measurements of the echo retrieval and Raman absorption lines. For homodyne detection the light field was modulated at 80 MHz such that it would have the same frequency as the signal field. The remainder of the details regarding homodyne detection are identical to the description provided for heterodyne detection except that the output signals were recorded in the time domain using an oscilloscope.

4.6 Classical Measurements

4.6.1 Raman Absorption Lines

We now discuss the Raman absorption lines that we will utilize for our GEM scheme. First we need to select a specific three-level system formed by the magnetic sub-levels which become degenerate under application of a weak magnetic field. Figure 4.16 shows the Raman absorption line from the degenerate hyperfine sub-levels and lines from the non-degenerate levels when an external magnetic field is applied. Due to our co-rotating polarization configuration, we find that one transition will exhibit a higher optical depth than the others, an observation discussed in further detail in Section 5.1. It is this transition we will utilize for GEM .

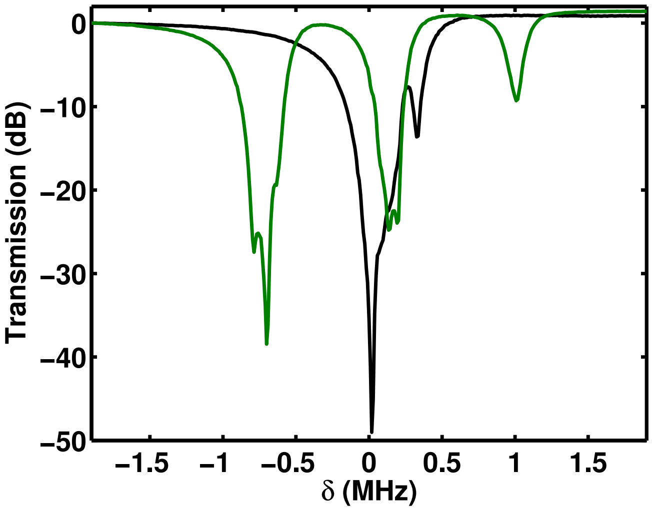

Figure 4.16: Raman absorption profiles with degenerate (black) and non-degenerate (green) magnetic sub-levels.

First we observe how the properties of the Raman lines change as a function of the single field detuning. These characterization measurements were done in the 18 cm long cell containing Kr buffer gas with single field detuning values between 0.6-1.9 GHz and the polarization of the control field optimized for the highest retrieval efficiency. A selection of the corresponding absorption profiles is shown in Figure 4.17 (a)-(c).

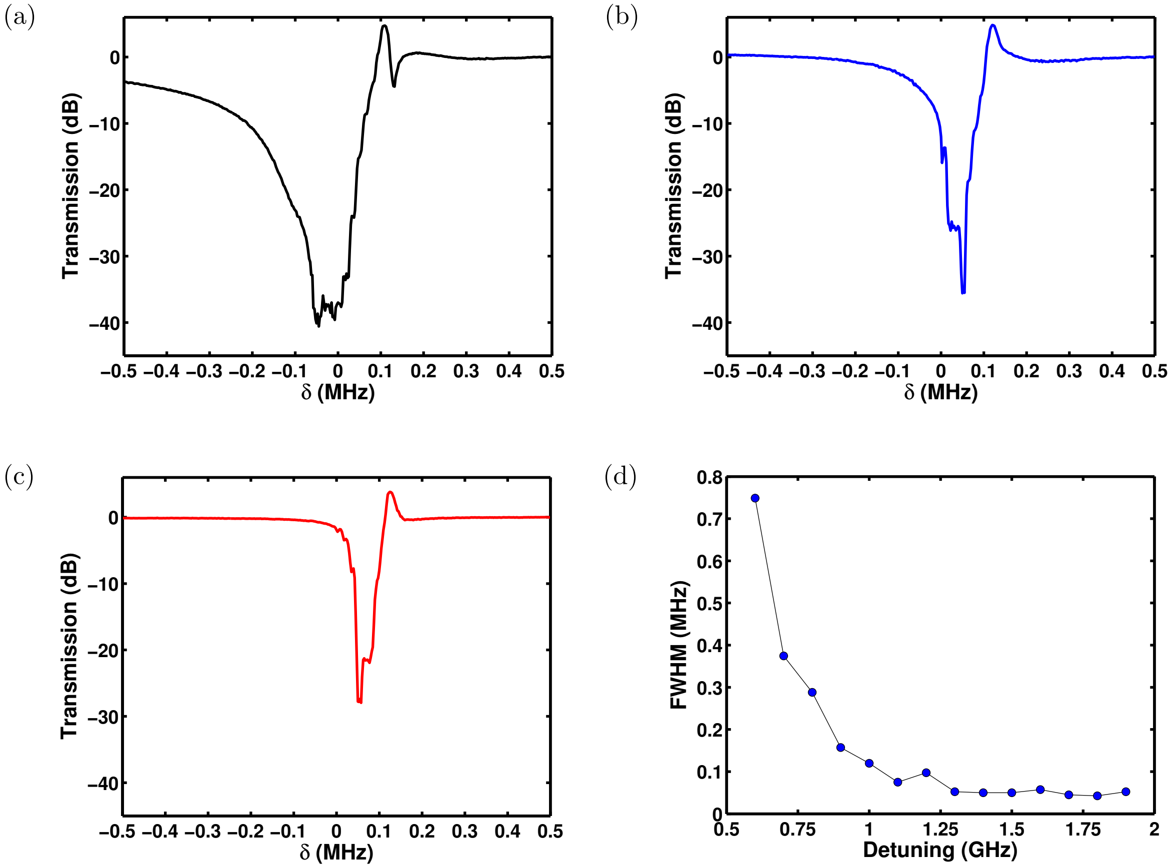

Figure 4.17: Raman absorption lines as measured with a selection of single field detuning values (a) 0.9 GHz (b) 1.3 GHz (c) 1.8 GHz , and (d) FWHM of as a function of the detuning showing the $1/\Delta^2$ dependence expected from Equation (4.13). The control field power was 250 mW, with a temperature of 75°C and a magnetic sub-level splitting of 6 MHz.

Additionally we plotted the FWHM as a function of the detuning Δ_c as calculated on a logarithmic scale. As shown in Figure 4.17d, the behavior follows the expected $1/\Delta_c^2$

dependency. From Figure 4.17(a)-(c) it can be immediately seen that the Raman absorption lines deviate in character from what would be anticipated based on Figure 4.8a. First, we note characteristics in the transmission profiles that bear a strong resemblance to those exhibiting a spatial intensity modulation in one or more of the fields, an effect which was described in Section 4.4.7. For the most part, this unsightly behavior was unavoidable when conducting the measurements and to the best of our knowledge, the weirdness in the line shapes had no strong correlation to any of the relevant properties of our GEM system, neither the efficiency nor the noise level[11]. Furthermore, it can be observed that the profiles exhibit transmissions greater than unity, or in other words gain, indicating the presence of FWM as discussed in Section 4.4.6 and to be investigated further in Section 5.2. While we found that the polarization could be adjusted to diminish and remove the gain features, as will be discussed in Section 5.1, we found no strong correlation between these features and noise.

A similar analysis of the Raman lines was performed with respect to control field power, using the same conditions as Figure 4.17, with powers in the range of 25-400 mW. A series of transmission profiles are plotted in Figure 4.18 (a)-(e).

---

[11] The effect of spatial modulation on the beam profiles as the cause of the weirdness of the Raman lines (Sec. 4.4.7) was not discovered until near the conclusion of the experiments and there was no immediate reason to believe these effects were detrimental to the memory performance. For these reasons there was no serious attempt made to improve the quality of the Raman absorption lines.

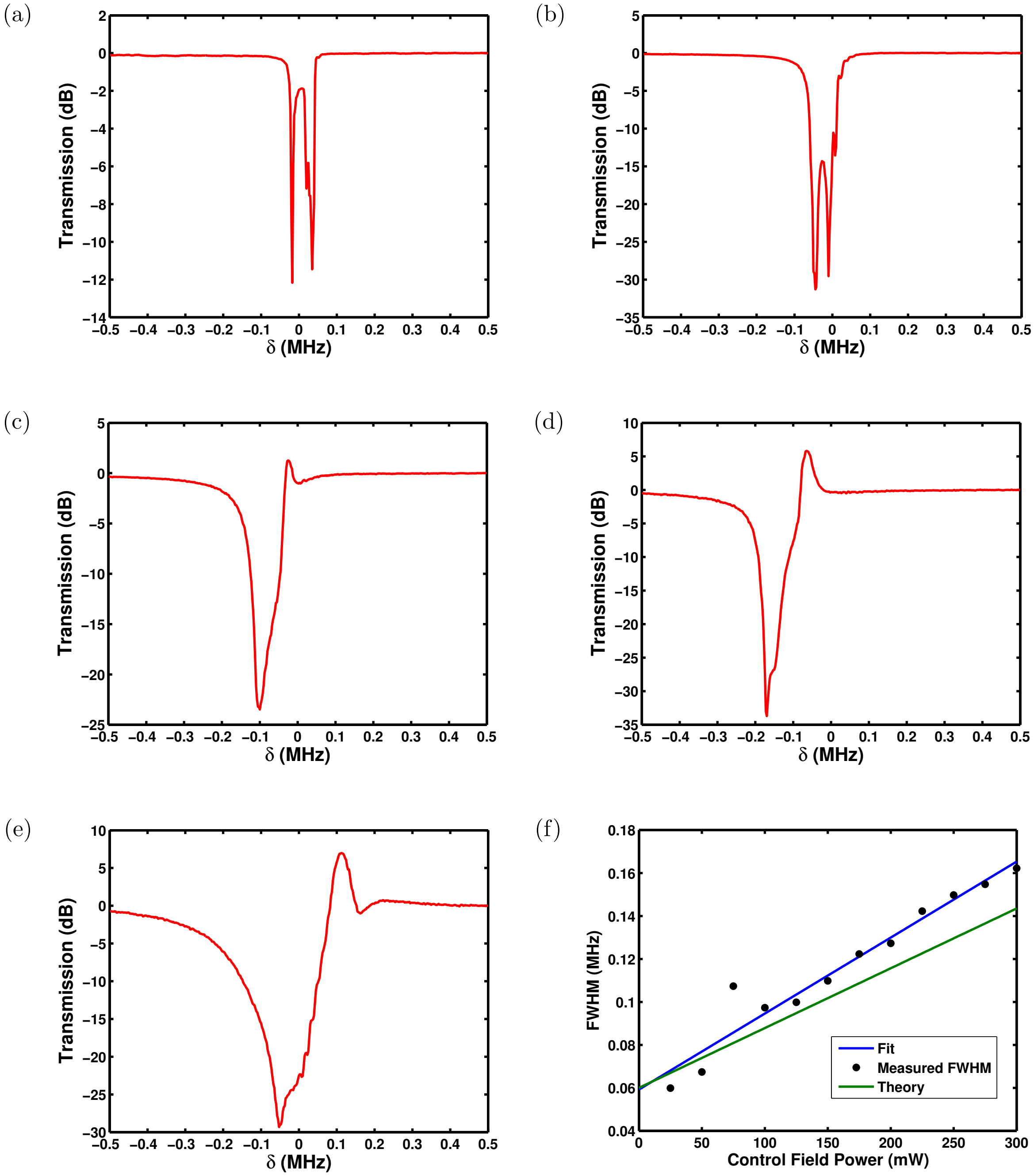

Figure 4.18: Raman absorption lines measured for a selection of control field powers (a) 25 mW (b) 100 mW (c) 200 mW (d) 275 mW (e) 400 mW and (e) FWHM of as a function of the control field power showing the linear relationship. A plot of the linear fit and theoretical prediction are shown for comparison. The single field detuning was Δ_c=1.3 GHz, at a temperature of 75°C with a magnetic level splitting of 6 MHz.

Observing the transmission profiles in Figure 4.18, we one can once again notice features indicative of gain and intensity modulation. One qualitative difference is that the jagged features tend to smooth out as the power is increased, the exact reason for this is not yet known. We also investigated the dependence of the FWHM on the control field power, where assuming that $\Delta_c \gg \Omega_c$ one would expect a linear relationship as predicted by Equation (4.13). Unfortunately, due to the unintended shape of the Raman absorption profiles, calculation of the FWHM values on a logarithmic scale yielded results that were nonsensical. To compromise, the transmission profiles were converted to a linear scale where many of the sharp features in the absorption became smoothed out. A plot of the calculated FWHM versus the control field power can be found in Figure 4.18f. Due to the nature of our measured Raman lines, deviations from linearity can be clearly noted. From a fit of the line we can extrapolate to find the corresponding ground state dephasing of our ensemble from the intercept, which yielded a value of $\gamma_{bc} = 60$ kHz[12]. The green line corresponds to the line width predicted by theory using the information in Reference [131].

4.6.2 Retrieval of Classical Echoes

Now we utilize our Raman absorption profiles for the storage and retrieval of optical light states. First, it was necessary to broaden the Raman absorption profile over the spectral bandwidth of the incoming light pulses, which in this case were 2 μs thereby requiring a broadening of $>$ 500 kHz. With all other parameters set to their desired value, this was achieved by running currents of ∼80 mA through the gradient coils which corresponded to a broadening of ξ= 28 kHz/cm. After the probe pulse was absorbed within the cell, the gradient magnetic field was flipped via the switch described in Section 4.5.2 to rephase the dipoles. By setting the magnetic field responsible for the rephasing to be greater than

---

[12] Omission of the data point corresponding to a control field power of 75 mW yielded an intercept of 52 kHz.

that used for the absorption, the time reversal process could be asymmetric [125]. In this way, the retrieved echo becomes temporally compressed relative to the input pulse, however this also reduces the amount of time the atomic coherence is subjected to any decay mechanisms and thus results in higher efficiencies[13]. Conversely, one could also expand the echo by setting the retrieval gradient to be less than the initial gradient used for absorption. As an example, a set of broadened Raman absorption lines that yielded a temporally compressed retrieved pulse are shown in Figure 4.19a with the associated retrieved echo with an efficiency of 86% shown in Figure 4.19b.

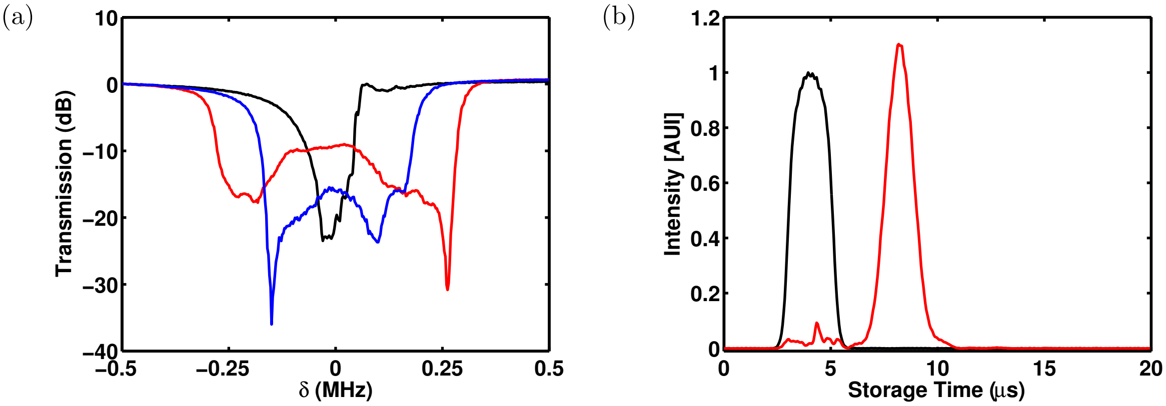

Figure 4.19: (a) Raman absorption lines utilized for optical storage, where profiles correspond to the initial absorption line (black), the broadened line used for storage of the pulse (blue), and the absorption profile of the gradient used for retrieval (red). (b) Input pulse (black) and corresponding retrieved echo (red) yielding an efficiency of 86% for a storage time of 4.2 μs. In this case, the retrieval gradient is higher than that used for storage which results in a temporally compressed retrieval pulse with a peak intensity higher than that of the input. The parameters used were a single field detuning of 1.3 GHz, control field power of 340 mW, and temperature of 75°C.

The storage duration of the memory procedure was controlled by the time at which

---

[13] Depending on the intended use for the memory, a compressed pulse may not be ideal due to the obvious reduction in the temporal fidelity with the incoming pulse.

the gradient was reversed (via the magnetic field switch in Section 4.5.2) after the pulse had entered the cell. For symmetric gradients, if the field was switched at time τ after absorption of the pulse, the emitted echo would be observed at time 2τ. After the incoming pulse has been absorbed, the decay time of the atomic coherence between the two hyperfine ground states should be related to the width of the Raman line. We measured the efficiency of the retrieved pulses for a series of storage times (Fig. 4.20a) and fit the values to an exponential curve to find the decay time.

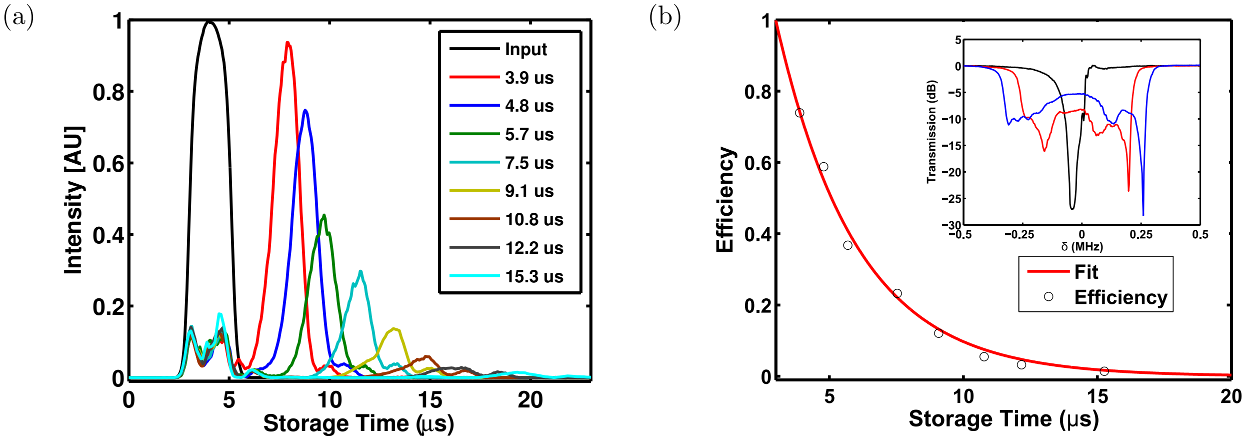

Figure 4.20: (a) Retrieved echoes for different storage durations. When operated in storage and retrieval conditions, the signal measured in the temporal mode of the original input pulse corresponds to the portion of the pulse that is transmitted and does not experience absorption. (b) Plot of the efficiency for different storage durations yielding a decay time of τ= 3 μs. (Inset) Corresponding Raman lines.

A fit to Figure 4.20 gave a decay time of τ= 3.0 μs, which is in agreement with the FWHM of the Raman line of Γ ~110 kHz corresponding to a decay time of $\tau = 1/(\pi\Gamma)$ ~2.9 μs. It has been reported that the decay time could be increased by a factor of 10 by turning off the control field for the duration of storage [126]. Since we were primarily concerned with the efficiency and noise capabilities of our memory and not the lifetime, the practice of turning off the control field was not implemented in our experiment

As a final investigation, we studied the dependence of the efficiency on the control field power. As derived in Section 4.3, the effective optical depth should increase linearly with the control field intensity and the efficiency should increase in accordance with Equation (4.9). The recorded efficiency values for a set of control field powers were found to be in agreement with the theoretical prediction calculated using the parameters in our setup (Fig. 4.21).

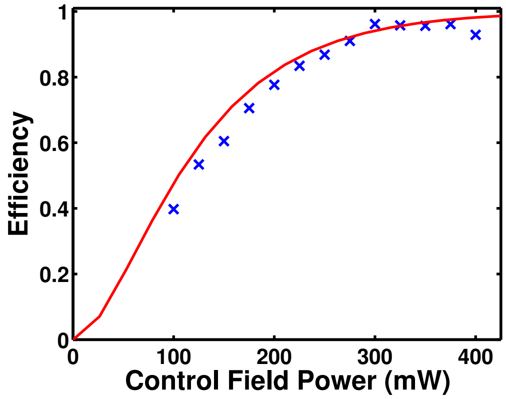

Figure 4.21: GEM Retrieval efficiency as a function of the control field power (Blue X's) versus the theoretical prediction (red line) calculated according to Equation (4.9). The parameters were Δ_c=1.3 GHz, with a magnetic field splitting of 4.6 MHz, at a temperature of 74°C.

Chapter 5

GEM as a Quantum Memory

One of the main goals of this thesis was to implement a GEM system capable of receiving a quantum state of light, storing it for a period of time, and finally recalling the state with its quantum nature intact. A device capable of this operation could be classified as a quantum memory. Another classification for a quantum memory is a device whose performance overcomes the limitations of a classical storage device, or more specifically, the memory must surpass what is known as the no-cloning limit [132]. To satisfy this criterion when storing Gaussian light states, namely squeezed vacuum and coherent states, we must be concerned with the degradation the states experience in the memory channel. Therefore, we will examine the loss, efficiency, and excess noise properties of our memory device and how these quantities change with respect to the degrees of freedom permitted in our setup.

5.1 Noise and Efficiency Characteristics

For GEM schemes involving an alkali vapour medium, two main polarization configurations have been reported. As was commonly done in EIT experiments, the first observation of Λ-GEM used control and probe fields that had orthogonal polarizations with respect to each another [124]. Intuitively, this is the most logical choice, since a cross-polarization scheme lends itself to easy separation of the probe and control fields. Hence, when our group constructed our first GEM system we used light fields of orthogonal linear polarization. With such a polarization scheme and a 18 cm long Kr buffer gas cell, we were successful in developing a system capable of light retrieval efficiencies that were commonly >80%. However, upon quantum state reconstruction of the retrieved mode, we observed 2 to 3 dB of extra noise in the output state quadratures. To investigate the possible causes of this noise, we began by looking at the homodyne spectrum in the mode of the probe field under GEM conditions with no input pulses present (Figure 5.1).

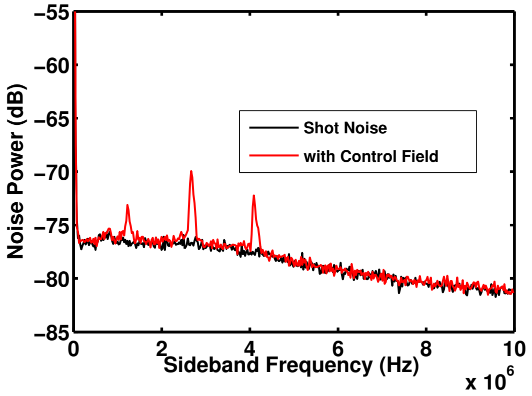

Figure 5.1: Homodyne spectrum near probe field resonance using orthogonal linear polarizations. Three distinct noise peaks are visible at sidebands corresponding to the Raman scattering peaks. The central frequency of these peaks with respect to one another is set by the splitting of the hyperfine magnetic sub-levels m_F.

In this measurement, a small uniform B-field was applied to break the degeneracy of the magnetic sub-levels and the local oscillator field was tuned off-resonant so any on-resonant characteristics were not masked by the 1/f noise of the spectrum analyzer. We observe three distinct noise peaks corresponding to the non-degenerate Raman scattering peaks. By selecting a suitable two-field detuning value the two off-resonant noise peaks can be moved outside the bandwidth of the homodyne detector, but the noise corresponding to the on-resonant Raman absorption line used for GEM will remain within the spectrum of the pulse. During GEM, this on-resonant noise peak is broadened over the spectral width of the probe pulse (Fig. 5.4b) in congruence with application of the gradient magnetic field. The effects of this broadening in regard to quantum memory will be discussed later.

An immediate possible cause for the noise is the effect of the cross-polarization scheme. As discussed in Chapter 4, to realize GEM we need a weak magnetic field to break the degeneracy of the hyperfine sub-levels, this magnetic field sets the quantization axis of our atoms. In our case, this is along the length of the cell and therefore any of our propagating light fields will have a polarization which is perpendicular to this axis. Since our linearly polarized fields can be decomposed into right and left circular components our atomic system is now coupled on all transitions where $\Delta m_F = \pm 1$ in accordance with selection rules (Fig. 5.2). This leaves us in the adverse circumstance of having a clutter of transition pathways [123] with multiple avenues for the atomic population to exchange levels.

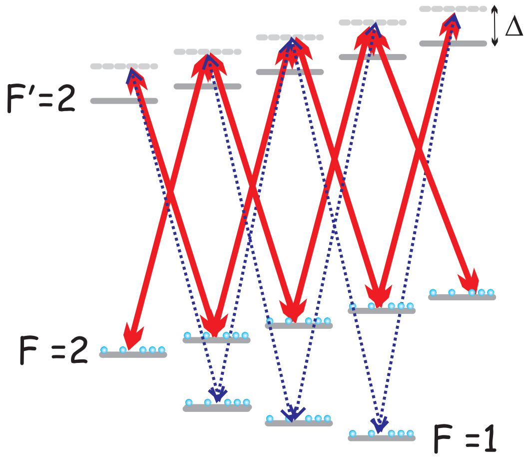

Figure 5.2: Transition scheme using control and probe fields that are of orthogonal linear polarization. The red and blue arrows correspond to transitions coupled by the control and probe fields respectively. Here, multiple transition pathways allow for atomic population to occupy multiple m_F sub-levels.

This type of population exchange is ill-suited for a Λ-GEM system. Ideally, one would have an isolated three-level system with all atomic population contained in a single ground state with the only population existing in the second ground state being placed there coherently and intentionally. Furthermore, it may also be hypothesized that it is the availability of these transitions that directly results in the presence of scattered photons and subsequent noise peaks shown in Figure 5.1.

A solution to this obstacle was proposed and implemented by the group of Ping Koy Lam and Ben Buchler at the Australian National University [86] which involved the use of co-rotating circular polarized light fields. As depicted in Figure 5.3, such a pumping scheme would nominally force all population into either the $|^5S_{1/2}, F = 1, m_F = \pm 1\rangle$ or $|^5S_{1/2}, F = 2, m_F = \pm 2\rangle$ ground state depending on the rotation direction of the polarization. More favourably this scheme should limit the possible ways the atoms could unintentionally end up in the $F = 2$ ground state used for storage, and if our hypothesis is correct, reduce the amount of scattered noise photons and extra noise.

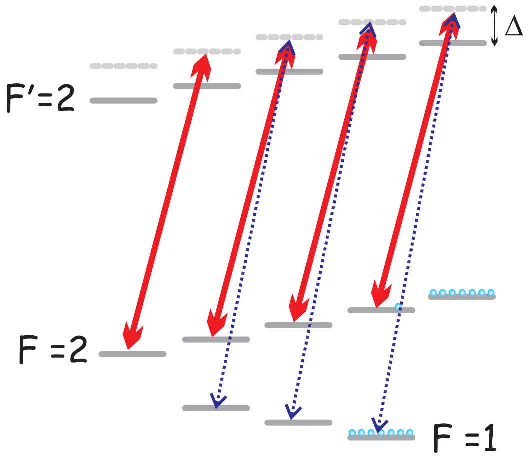

Figure 5.3: Transition scheme using co-rotating circular polarization for the probe and control fields. Nominally, all population would only be found in the pair of m_F sub-levels when in the steady state.

The consequence of using this scheme is that one can no longer take advantage of basic polarization filtering methods to remove the strong control field from the channel of the probe. As described in Section 4.5.3, this issue was overcome by placement of a filter cell after the oven housing the memory cell (shown in Figure 4.15).

The homodyne spectrum in the mode of the probe field with co-rotating circular polarized fields is shown in Figure 5.4a, once again a small offset magnetic field was applied so the noise peaks could be resolved and only the vacuum state was present as an input.

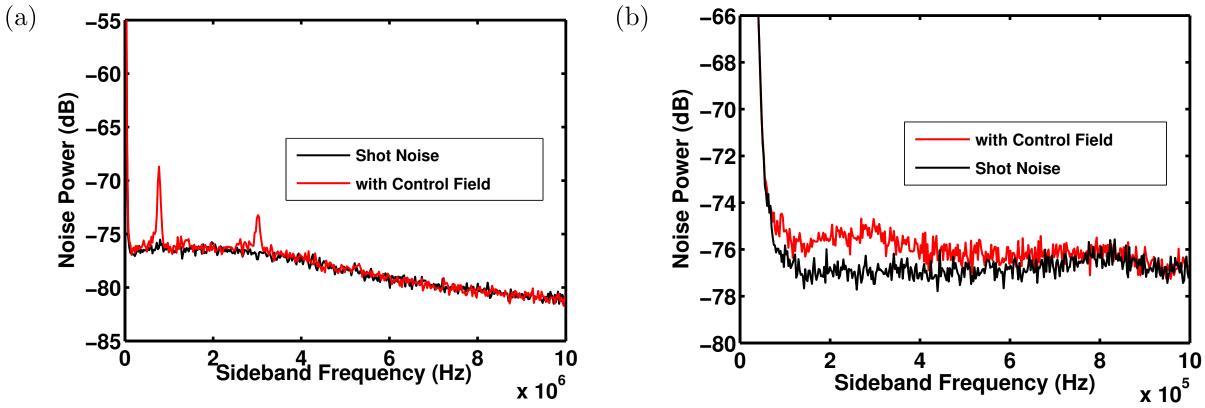

Figure 5.4: (a) Homodyne spectrum near-resonant to the probe field under the co-rotating polarization configuration with a uniform magnetic field applied. Note that, similar to the the cross polarization case, there exist three noise peaks with the peak at the furthest sideband barely resolvable. (b) Homodyne spectrum as measured in the steady state configuration (i.e. no switching of the magnetic fields) on-resonance with the probe field with the gradient magnetic field present.

Immediately we observe that the three noise peaks continue to persist, this time with magnitudes decreasing in accordance with the anticipated population distribution and measured absorption which was plotted in Figure 4.16. From this result, we conclude that the noise peaks cannot be solely due to the availability of the additional transitions pathways, and that our hypothesis in this regard is wrong.

GEM is performed on-resonant to the largest peak which exhibits ∼5 dB of extra noise relative to the shot noise level. Under application of the gradient magnetic field, this noise peak becomes broadened over the spectral width of the probe pulse (∼500 kHz for a pulse of 2 μs duration) as shown in Figure 5.4b. When performing state reconstruction of the retrieved mode (Sec. 2.4) this noise manifests itself, among other things, as an increase in the quadrature variance for any Gaussian input state and an increase in the mean photon number for a retrieved vacuum mode. Evidence to support these effects will be presented later in the Chapter.

Since these results were inconsistent with the group of Ping Koy Lam at Australia National University [126, 86] we proceeded to thoroughly investigate the parameter space. We aimed to find a set of controllable parameters in our GEM system that would either eliminate or reduce the aforementioned noise in the mode of the probe field such that our system can satisfy the criterion of a continuous variable quantum memory. These parameters are mainly comprised of the polarization, single field detuning Δ_c, and the control field power which is proportional to the square of the Rabi frequency $|\Omega_c|^2$. The metrics used to characterize these parameters were the classical retrieval efficiency as measured with heterodyne detection and the extra noise observed in the mode of the probe pulse. Efficiencies were calculated by integration of the retrieved pulse area relative to that of the input with the values obtained strictly from operation of the memory cell without correction for loss. Noise was calculated by averaging the spectrum analyzer signal over the spectral width of the probe pulse when the system was in the steady state configuration (Fig. 5.4b) and only the vacuum field was present at the input.

We begin with measuring the efficiency and noise behaviors with respect to the probe polarization in both co-rotating circular and orthogonal linear configurations. The efficiency measurement was carried out by randomizing the polarization of the probe in either the linear or circular basis before the field was sent into the memory cell. Then by rotating the polarization of the wave plates after the memory cell followed by filtering via the PBS (Fig. 4.15), we could choose a particular polarization for analyzing the noise and efficiency. Therefore in this measurement, the efficiency values were calculated using the component of the input polarization that matched what was selected for measurement using the wave plate and PBS combination. The control field polarization remained in either constant circular or orthogonal polarization depending on the measurement. As described previously, the noise was measured using only the vacuum state as the probe. The results from both polarization bases are shown in Figures 5.5a and 5.5b respectively. In this measurement we used parameters typically found to correspond to high efficiency retrieval with Δ=1.2 GHz, $|\Omega_c|^2$=250 mW, T=74°C and δ=4.6 MHz[1].

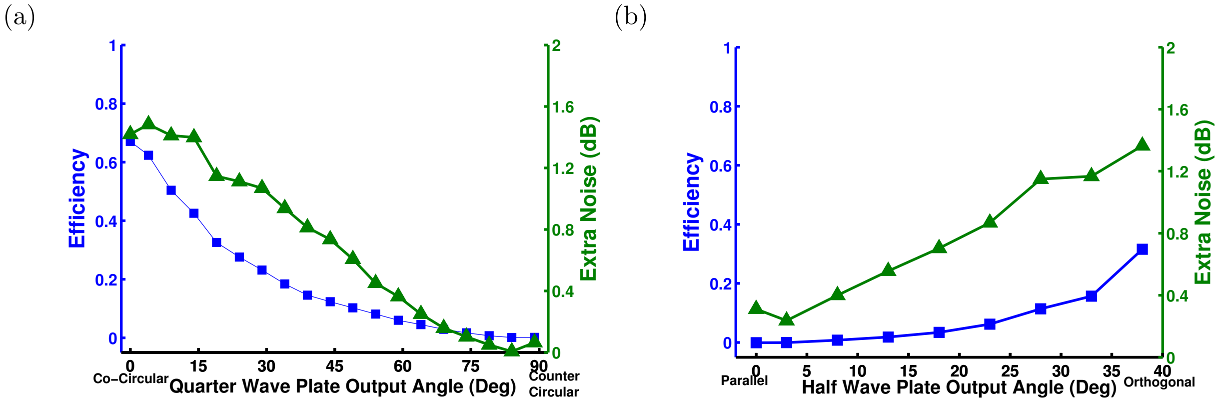

Figure 5.5: Efficiency and extra noise plotted against output polarization. (a) Selecting initially co-rotating circular polarization and rotating the quarter-wave plate until the orthogonal circular polarization is selected. (b) Starting with initially parallel linear polarizations and rotating the half-wave plate to an orthogonal configuration. This measurement was performed in the cell containing 0.5 Torr of Ne buffer gas and while not presented here the cell with Kr buffer gas showed similar results.

A key feature to extract from Figure 5.5 is that the noise does not exhibit a high degree of sensitivity to the polarization angle. One could then claim that the noise is not, primarily at least, because of a small impurity in the polarization of the fields. This is in contrast to the observations from Section 4.6.1 where the noticeable gain peaks did

---

[1] Since we were only concerned with how the efficiency and noise behaved with respect to one another, time was not spent on attaining the absolute highest efficiency ever recorded using the setup.

indeed have a sharp response with the polarizations.

We now explore how our system behaves as we blue detuned our laser fields from resonance[2]. For this measurement, since we are examining the behavior closer and further from atomic resonance we must account for the loss experienced by the probe field when propagating through the vapour cells. If not taken into consideration, we might underestimate the noise at detunings closer to resonance due to attenuation from the tail of the Doppler-broadened line. Therefore, the measured noise values were extrapolated by correcting for the attenuation. Both the Kr and Ne buffer gas cells were studied at a temperature of T=74°C, a control field power of 250 mW and a sub-level splitting of δ=4.6 MHz. The results are given in Figure 5.6.

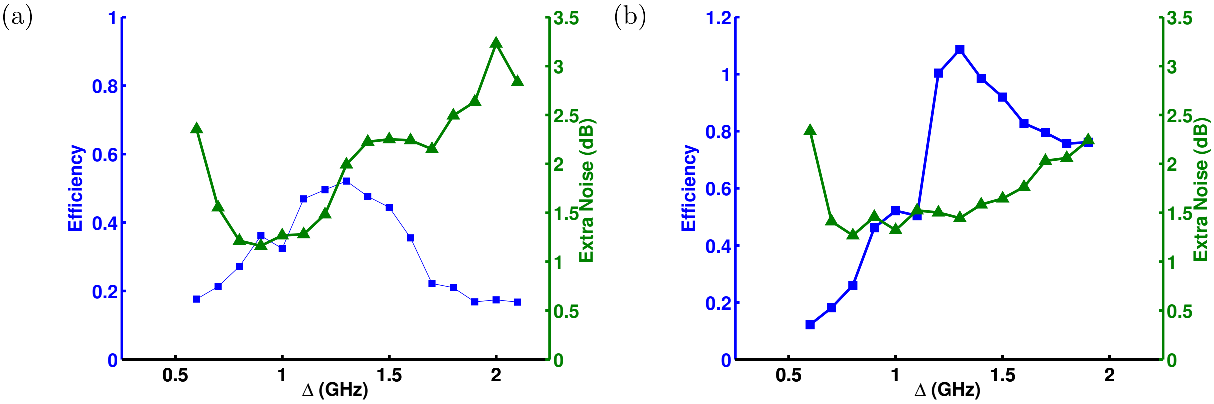

Figure 5.6: Efficiency and extra noise as measured with increasing single field detuning for vapour cells with (a) 0.5 Torr Ne and (b) 0.5 Torr Kr buffer gas.

We can take note of some similar tendencies between the two buffer gas cells. As we move away from resonance the efficiency will increase due to a reduction in the reabsorption of retrieved photons. At some frequency value, the efficiency reaches a maximum and begins to drop off due to the reduction in optical depth (see Section 4.4.2)[3].

---

[2] Due to the ^{85}Rb resonance exploited for extinguishing the control field it was not possible to investigate red detuned fields with co-rotating circular polarization.

[3] Close inspection of Figure 5.6 will display efficiencies greater than 100 % meaning gain was most

In regard to the extra noise, after a sharp decrease near resonance we see a steady increase with further detunings. The increase in noise can be at least partially attributed to a reduction in absorption caused by the tail of the Doppler-broadened line. The high noise values observed near resonance are partially an artifact of an over correction for the low transmission values of $\sim$30 % through the filter cell. As can be seen in the plots, we found the optimal detunings to be Δ=1.1 GHz and Δ=1.3 GHz for the Ne and Kr buffer gas cells respectively. Detuning values greater than Δ=1.6 GHz became increasingly difficult to analyze due to a reduced extinction of the control field through the filter cell. This could be compensated for by increasing the filter cell temperature but came with the additional detriment of **k**-vector fluctuations and noisy signals as discussed in Section 4.5.3.

Next we measured the dependence on the control field power, where the trends exhibited were more monotonic than those of the detuning. Extra noise and efficiency were measured for control field powers between 100 - 400 mW at a temperature of T=74°C, a single field detuning of Δ=1.1 and 1.3 GHz for the Ne and Kr buffer gas cells respectively, and a magnetic field splitting of δ=4.6 MHz. The results are shown in Figures 5.7a and 5.7b.

---

likely present during this measurement but was neglected since it was irrelevant to the primary focus of the characterization.

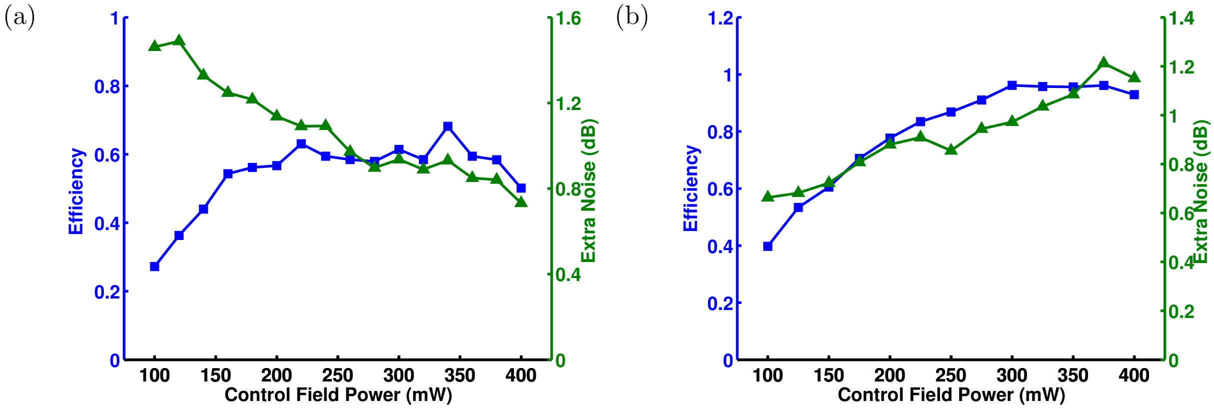

Figure 5.7: Efficiency and extra noise as measured with increasing control field power for the vapour cells containing (a) 0.5 Torr Ne and (b) 0.5 Torr Kr buffer gas.

We see that the efficiency follows an asymptotic behavior in that it levels off at high control field powers. This is consistent with the dependence on optical depth in Equation (4.9). In this system, the optical depth is proportional to square of the effective Rabi frequency for the Raman transition, and as mentioned in Section 4.4.1, is only valid in the regime where $\Delta \gg |\Omega_c|$. One would expect the extra noise to increase with the control field power due to Raman scattering and FWM (to be discussed in Section 5.2) which is the case in Figure 5.7b for the Kr buffer gas cell. The opposite trend occurs in the cell containing the Ne buffer gas (Fig. 5.7a), the reason for this is unknown and requires further investigation[4]. Regardless, based on these findings one could conclude that any regime generating high efficiency would require a strong control field which is associated with high extra noise.

Moving on, we look at the uniform B-field applied in order to break the degeneracy of the magnetic sub-levels via the Zeeman effect. As can be seen in Figure 5.8, we found no significant dependence on the level shift, which is what we would anticipate provided that the Raman transition utilized for GEM is shifted far enough to be distinct from the

---

[4] We find that the process tensors calculated in Section 5.12 are in disagreement with this result, indicating a more careful measurement is necessary.

other Raman transitions. Therefore, this parameter was not investigated further.

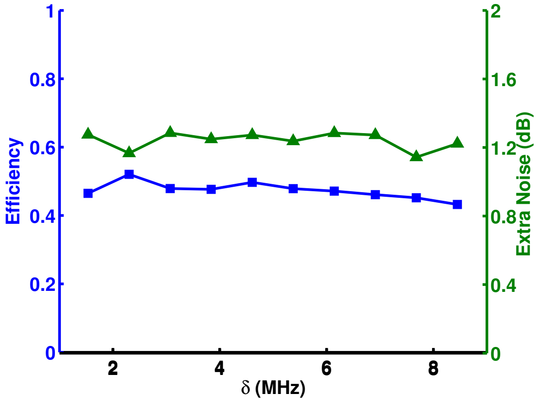

Figure 5.8: Efficiency and extra noise as measured with the magnetic field splitting for the cell containing 0.5 Torr of Ne buffer gas. It can be observed that increasing the magnetic field causes no significant changes to our metrics. Similar results were observed for the cell containing 0.5 Torr of Kr buffer gas.

On the whole, these results are discouraging, it appears the optimal efficiency and the presence of extra noise go hand-in-hand and one cannot achieve high efficiency while concurrently suppressing the extra noise. Now, with our search of parameter space complete, we now look more closely at the mechanisms causing the extra noise.

5.2 Raman Scattering versus Four Wave Mixing

There are two likely sources of the extra noise in our system, the first is four wave mixing (FWM) which was discussed briefly in Section 4.7. The other noise source is Raman scattering which results in the presence of spurious photons in the mode of the probe field. We now look at the experimental evidence regarding each of these sources individually.

Four wave mixing is a mechanism that permits coherent population exchange between the two ground states and results in the presence of gain peaks, which were apparent in our experiment as shown in Figures 4.17 and 4.18. As discussed in Section 4.4.6, FWM processes are dependent on the phase-matching between the pump and signal fields, which in our system corresponds to the control and probe fields respectively. Thus, the gain and extra noise should exhibit some dependence on the alignment of the **k**-vectors between the two fields [136]. As a crude test for the presence of FWM, we observed the effect of spatial-mode mismatch on the efficiency and noise (Figure 5.9). In this measurement, the control field alignment was first optimized for the highest efficiency and then subsequently misaligned from the point on the 90:10 beam splitter where the control field was combined with the probe (Fig. 4.15). Noise values correspond to the vacuum seeded case (mentioned in Section 4.4.6), meaning no signal (or probe) field was present.

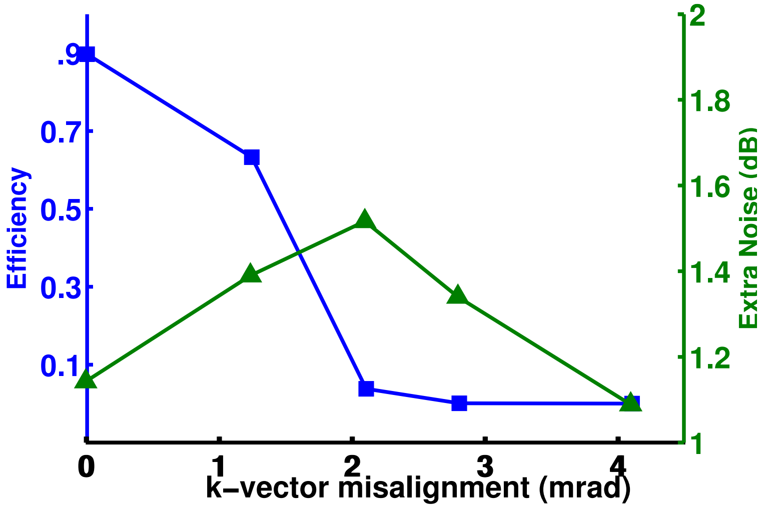

Figure 5.9: Efficiency and extra noise as a function of control field misalignment.

From Figure 5.9 it can be seen that as the control field becomes further misaligned the efficiency drops off monotonically, this is in contrast to the extra noise which exhibits a maximum near 2 mrad. This behavior of the extra noise is what one would expect under FWM conditions, where the gain exhibits its peak value when there is a non-zero angle between the **k**-vectors of the fields [136]. However, it should be noted that despite this angular dependence, the recorded extra noise level in this measurement was always greater than 1 dB. This signifies to us that while FWM processes may be present and contributing factor to the extra noise there still exists a least one other noise mechanism. To investigate the FWM in our system further, we looked at the dependence of the gain peaks present in the Raman spectroscopy with respect to the single photon detuning (Fig. 5.10a) and control field power (Fig. 5.10b). As a primitive analysis, we used the same experimental configuration described in Section 4.6.1, and quantified the gain by recording its maximum value as a function of the mentioned parameters. If FWM is the reason for the extra noise, we expect the classical FWM peak to behave in a similar fashion to the quantum extra noise as a function of the experimental parameters.

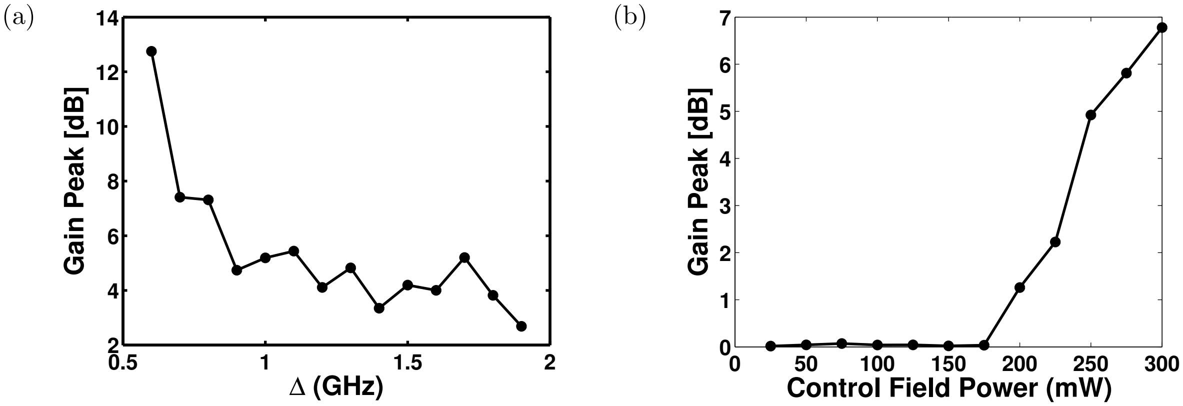

Figure 5.10: Maximum value of the gain peak observed in the vapour cell containing 0.5 Torr Kr buffer gas at 74°C as a function of (a) single field detuning and (b) control field power.

In Figure 5.10a we see that there is a high amount of gain near resonance that falls off sharply at about 0.8 GHz, the gain then remains roughly constant up to the largest single field detuning value observed. This result differs from the relationship shown in Figure 5.6b where the extra noise exhibited a steady increase with single field detuning values greater than 0.8 GHz. The behavior of the gain with respect to control field power is shown in Figure 5.10b, where we see that the gain is non-existent until about 200 mW at which point it increases substantially. These results possibly indicate that a minimum Rabi frequency is necessary before one can observe gain[5]. More importantly however, this behavior with the control field power is in disagreement with the plot of the extra noise in Figure 5.7, where the observed extra noise was present even at control field powers of 100 mW. From these findings we can conclude that while FWM is present in our system and is in all likelihood a contributing factor to the observed extra noise, there exists at least one other mechanism which is induced by the control field. This brings us to the other possible noise source, that of Raman scattering.

Unlike FWM where the photons comprising the gain are coherent, in Raman scattering, random $F = 2$ ground state atoms not utilized for storage become excited followed by subsequent emission of incoherent photons into the mode of the probe field. Such atoms can find themselves in the spatial mode of the probe field for a number of reasons which can all be treated as un-pumped atoms entering the beam area. The simplest explanation is that the atoms are already present before the probe field is absorbed. Therefore one would expect that by ensuring the entire ensemble is polarized before the storage procedure, the noise observed in the mode of the probe field would be reduced. This could be achieved by sufficient optical pumping of the atomic ensemble to prepare it in the closest representation of a pure state before the probe pulse enters the medium. In our setup, we did not have the availability of a second phase-locked laser or the means to quickly detune the lasers by factors of GHzs to carry out an ideal optical pumping procedure. We did however find that the extra noise observed in Figure 5.4b decreased with an increased duration of off-resonant pumping by the control field before the magnetic field gradient was switched. This observation seems reasonable: since the control

---

[5] The absence of gain at low control field powers could be an artifact of the transverse intensity profiles of our fields (Sec. 4.4.7).

field is closer to the $|^5S_{1/2}, F = 2\rangle \leftrightarrow |^5P_{1/2}, F' = 2\rangle$ transition the fraction of total atoms left in the $F = 2$ ground state should be reduced.

Another explanation is that random $F = 2$ ground state atoms continually enter the spatial mode of the probe field at a constant flux which leads to extra noise observed in the steady state. If this were the case, then illumination of the entire cross-section of the vapour cell with the control field for a sufficient period of time could ideally place every individual atom in the $F = 1$ ground state before entrance of the probe pulse. While a thorough investigation was not undertaken due to time constraints, increasing the beam waist of the control field only served to decrease the efficiency while the noise observed in the spectrum of the probe field remained >1 dB.

A final source of the unwanted ground state atoms is those introduced by dephasing or decay, meaning any atoms which originally formed the coherence in Equation (4.2) will either lose their phase or "decay" to the $F = 1$ ground state. This can be caused by a few mechanisms such as atom-atom collisions, atom-wall collisions, and off-resonant excitation. In regard to atom-atom collisions, they should be suppressed by the presence of buffer gas in the vapour cell, and based on the results of the ANU group [126, 86] we would have to believe such collisions are not the source of Raman scattered photons in our setup.

5.3 csQPT of GEM

Acquisition of the data necessary for characterizing our GEM system was similar to what was done in Section 3.2 for EIT. To characterize the GEM process we employed a different numerical process reconstruction than that used in Section 2.6: the maximum likelihood method introduced in Section 2.7.2. Thus, the reconstruction of density matrices was not required and the characterization was achieved by direct use of the measured quadrature and phase values. GEM was performed in two separate vapour cells typically kept at 74°C which provided a number density of $\sim 10^{11}/\mathrm{cm}^3$ and a corresponding on-resonant optical depth of ~ 700. Based on the results from the previous section we used a detuning of $\Delta_c = 1.1 - 1.3$ GHz and the control field powers were either 240 or 340 mW. Optimal alignment of the control field was attained by observing the classical retrieval measured using hetereodyne detection, this also allowed us to obtain the temporal modes needed for the time-integrated quadrature values (Sec. 2.4). To obtain the data necessary for process reconstruction, we sent 10 coherent states into the memory with amplitudes ranging from 0 to 2. For every state, 50 000 quadrature values for both the input, which were measured only in the absence of the control field, and output were obtained by integrating the homodyne current over the temporal waveforms. The associated phase values were calculated directly from the oscilloscope trace. To account for the losses external to the memory which the input states are subjected to, we first considered the on-resonant transmission for the probe field when propagating from just before the memory cell until after the filter cell when the control field was absent. This transmission was measured to be $\sim 78\%$ where some of the loss can be attributed to condensation build up on the cell windows. The visibility with the local oscillator was 97 % (Sec. 2.3.2) and with a photodetector efficiency of 92 % we typically had an end-to-end detection efficiency of 70 %. This loss was corrected for in the maximum likelihood reconstruction program [45]. All characterizations were done using the co-rotating circular polarization scheme with beam waists of 2 mm and 6 mm for the probe and control fields respectively.

We performed three process reconstructions of our Λ-GEM system and the diagonal elements of the corresponding process tensors $\mathcal{E}_{mm}^{kk}$ are shown in Figure 5.12. The process tensors shown in Figures 5.11a and 5.11b correspond to measurements performed in the 20 cm Ne buffer gas cell and employed identical parameters with the exception of the control field power. The third process tensor shown in Figure 5.11c was reconstructed using measurements from the 18 cm Kr buffer gas cell. The remainder of the parameter values can be found in the caption of Figure 5.12. In the data used for these reconstructions, the mean efficiencies of the retrieved weak coherent states were 63%, 75%, and 75% corresponding to the process tensors in Figures 5.11a, 5.11b and 5.11c respectively.

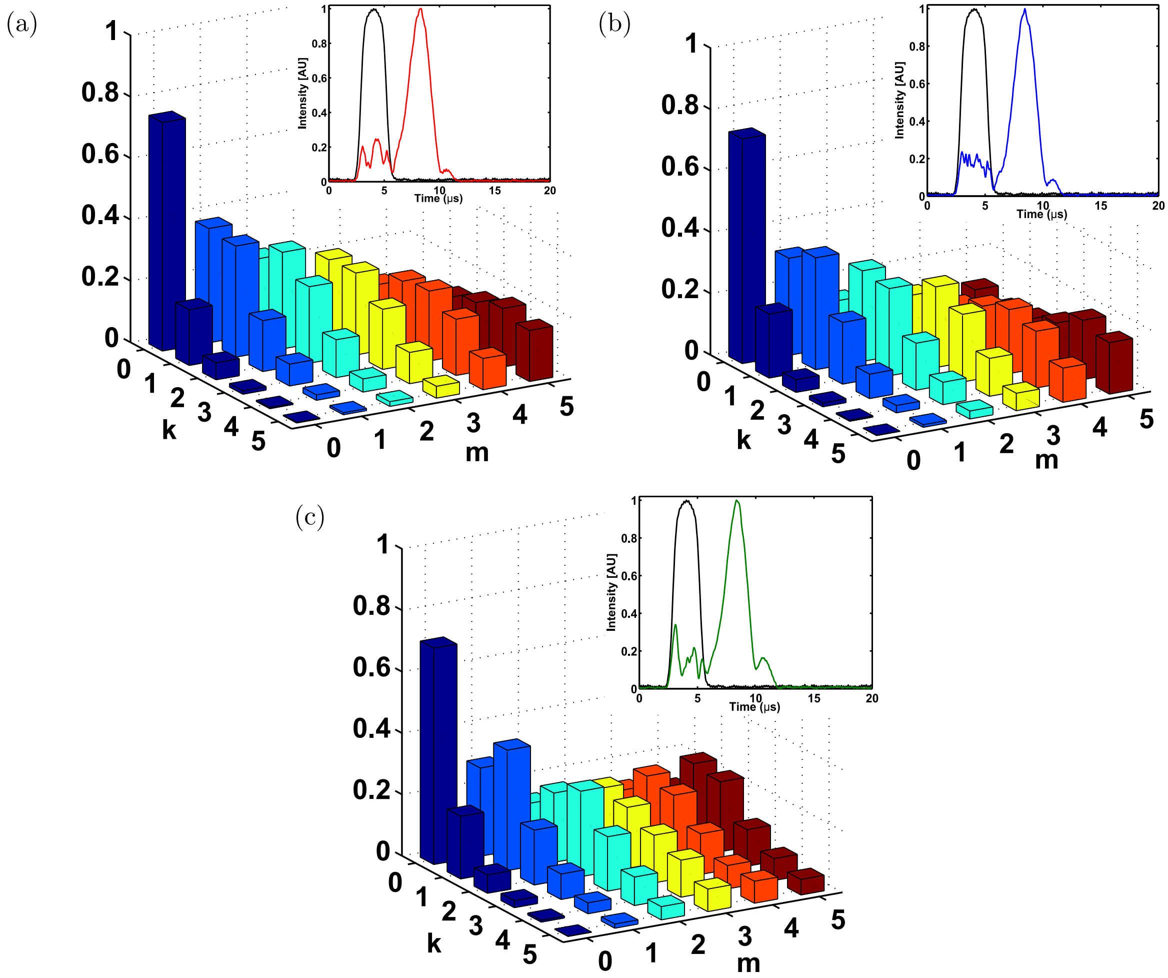

Figure 5.11: Diagonal elements of the reconstructed process tensors $\mathcal{E}_{mm}^{kk}$ where each m input state (colours) has a distribution of outputs k. The parameters used were: (a) Δ_c=1.2 GHz, sub-level splitting of 4.6 MHz, control field power of 240 mW; (b) Δ_c=1.2 GHz, sub-level splitting of 4.6 MHz, control field power of 340 mW; (c) Δ_c=1.3 GHz, sub-level splitting of 4.6 MHz, control field power of 240 mW. (Insets) Input and retrieval temporal modes used in the reconstruction.

By comparing the reconstructed superoperators in Figure 5.12 with those in Figure 3.7 for an EIT based quantum memory some immediate conclusions can be drawn. A strong indicator that can be used to preliminarily evaluate these systems on their capability as a quantum memory is the values of output elements k corresponding to the vacuum state input m=0. Here one would ideally want $\mathcal{E}_{00}^{00} = 1$ and any deviations from this value are evidence that the output is thermalized and exhibits an associated increase in quadrature variance. Looking at the mean photon number of the output for a vacuum state input, that is the quantity $\mathrm{Tr}[\hat{n}\hat{\mathcal{E}}(|0\rangle\langle 0|)]$, we find values of 0.33, 0.32, and 0.39 in the order that the tensors were presented. Preserving the above order, these values correspond to a quadrature variance of 2.2 dB, 2.15 dB and 2.5 dB which are consistent with the output variance measured for a vacuum state input of 2.14 dB, 2.87 dB, and 2.16 dB respectively. These results tell us that with only a vacuum state as input, our GEM operation will produce on average, 0.35 contaminate photons in the output mode. This is in stark contrast to the EIT memory where the thermalization only resulted in a mean photon number of 0.022 at the output [137]. This is the first sign that our GEM system, in its current form, is incapable of quantum memory operation.

5.3.1 Prediction on Squeezed Vacuum States

Next we use our reconstructed process tensors to predict how our GEM system will preserve squeezed vacuum states. To do so, we act the superoperators on the reconstructed density matrix of a state with a noise of -1.54 dB and 5.38 dB in the squeezed and anti-squeezed quadratures respectively (Figure 5.12a). The state was generated in our lab by employing a sub-threshold optical parametric amplifier, the same setup used in Reference [42]. We act our three reconstructed process tensors on the input state and calculate the Wigner functions of the associated outputs which are shown in Figures 5.12b, 5.12c, 5.12d. The variance at all phases is shown in Figure 5.13.

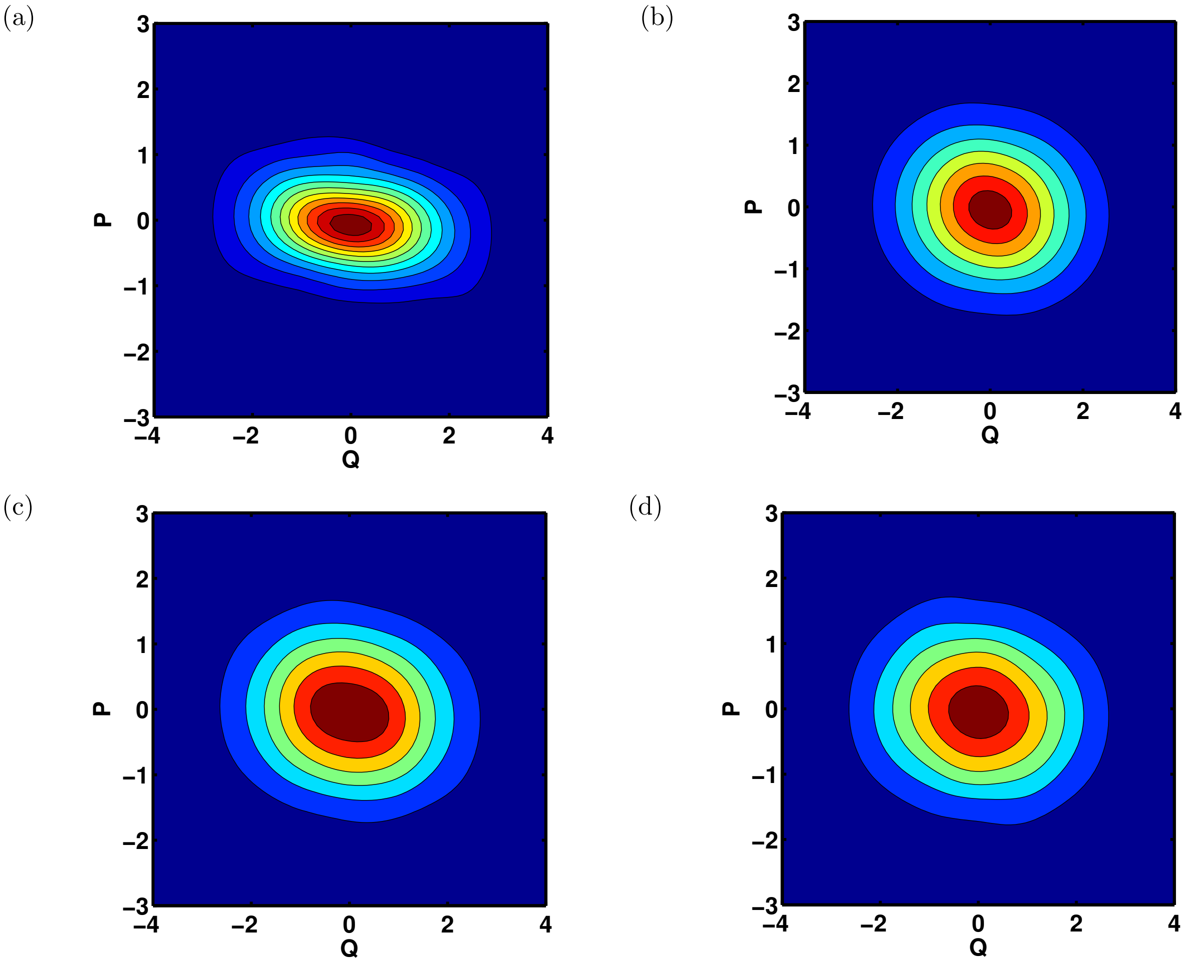

Figure 5.12: Wigner functions corresponding to the (a) input squeezed vacuum state and the output after operation by the reconstructed superoperators with (b) Ne buffer gas and 240 mW control field, (c) Ne buffer gas and 340 mW control field, and (d) Kr buffer gas and 240 mW control field.

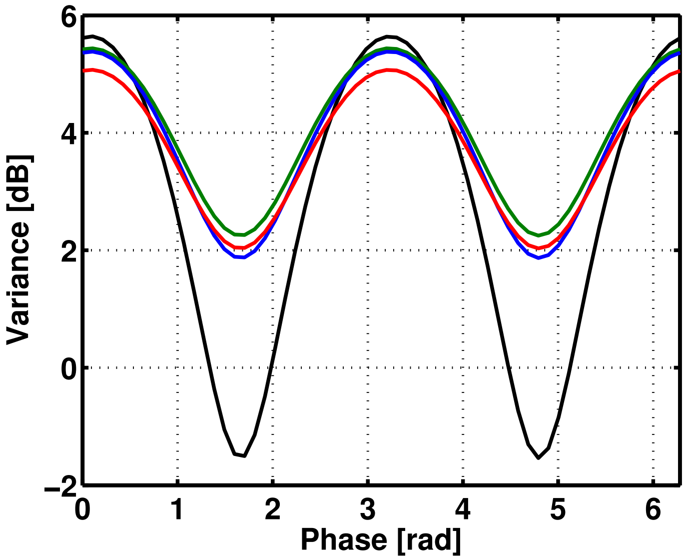

Figure 5.13: Variance versus phase for the input squeezed vacuum state (black) and the retrieval states predicted by the process tensors with: red- Ne buffer gas and 240 mW control field; blue-Ne buffer gas and 340 mW control field; green- Kr buffer gas and 240 mW control field.

From the Wigner functions in Figure 5.12 and the variance plots in Figure 5.13 it can be seen that none of the reconstructed tensors predict the retrieval of any noise reduced below the standard quantum limit after storage with our GEM system. This is a much different outcome than from our EIT system where -0.21 dB of noise reduction was retrieved from the vapour cells [137]. While this is a disappointing result, it is not surprising based on the comparisons between our GEM and EIT process tensors.

5.3.2 T-V Representation

Several criteria exist for classifying an optical storage device as a quantum memory[6], the most straightforward is any device that is capable of receiving and recalling an optical

---

[6] This statement may be a subject of debate for some.

state whilst preserving its quantum nature. Such a criterion was satisfied by our EIT memory in Section 3.2 but our GEM-based system presented in the previous section fell short of this criterion. Some have also used the calculation of fidelity as a metric for quantifying their quantum memory device (Sec. 2.6). However, fidelity is not a good indicator for our purposes since its value is dependent on the input state[7]. More suited towards our continuous variable measurements is a state-independent metric involving signal transfer coefficients T and conditional variances V_{CV} which was first proposed by Grangier [138] for transmission over quantum channels. These were later adopted for quantum memory evaluation in References [85, 139] but have been modified in more recent quantum memory studies [121, 86] to a form which we will apply to our GEM system. Briefly, T is a measure of how well the memory preserves the input and V_{CV} is a measure of the noise added to the input as a result of the memory operation. They are defined by

$$T^{\pm} = \frac{\eta}{1 + V_{out}^{\pm} - V_{in}^{\pm}} \tag{5.1}$$

$$V_{CV}^{\pm} = (1 - T^{\pm})V_{out}^{\pm}. \tag{5.2}$$

Here $V_{in}^{\pm}$ and $V_{out}^{\pm}$ are the measured quadrature variances of the input and output states respectively. The superscripts of $+$ and $-$ identify X and P quadratures respectively, η is the memory efficiency and here one unit of vacuum variance is normalized to $V_{|0\rangle\langle 0|}^{\pm} = 1$. Calculation of these variables allows comparison of our memory to the limitations of a classical storage device which are $V^{+} \times V^{-} = 1$ and $T^{+} + T^{-} = 1$. It then follows that any device that simultaneously achieves $V_{CV}^{+} \times V_{CV}^{-} \leq 1$ and $T^{+} + T^{-} \geq 1$ can be said to surpass the no-cloning limit and can be classified as a quantum memory [86]. A perfect

---

[7] The easiest explanation for this is to think of a very large coherent state of say $|\alpha| \approx 10^{6}$ that is retrieved from a memory device capable of 99% efficiency and adds no extra noise. The output state will have a negligible overlap with the input to produce a fidelity of zero. The opposite extreme would be a brick which can store and retrieve the vacuum state with a fidelity of unity.

memory device would have unit efficiency such that $T^+ + T^- = 2$ and would not add any extra noise thus $V^+_{CV} \times V^-_{CV} = 0$. We calculated these values for the weak coherent states retrieved from our memory and represent them pictorially on what is known as a T-V diagram shown in Figure 5.14. Efficiencies correspond to strictly that of the memory with loss not taken into account, however all output variance values $V^{\pm}_{out}$ were first corrected for the losses external to the memory as was described in Section 5.12. The variance of our measured input states were typically near unity matching that of a vacuum state.

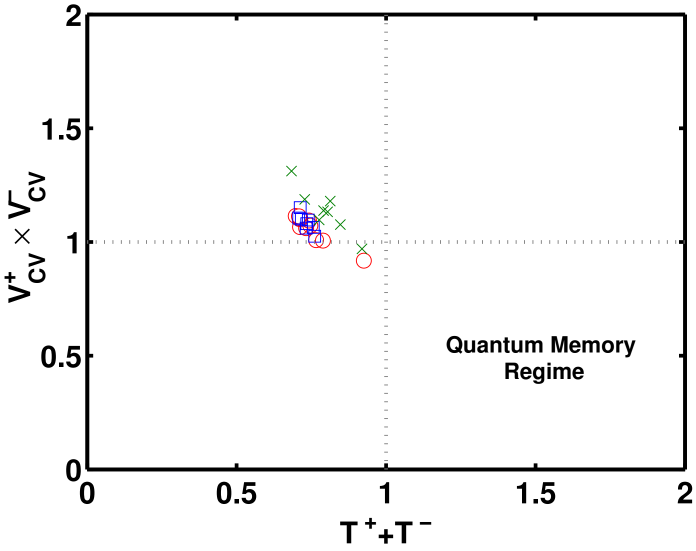

Figure 5.14: T-V diagram for weak coherent states retrieved from the GEM system, the bottom right quadrant set by the dashed lines corresponds to the quantum memory regime. The data points correspond to the retrieved states used for reconstruction of the process tensors with: red circles - Ne buffer gas and 240 mW control field; blue squares - Ne buffer gas and 340 mW control field; green X's - Kr buffer gas and 240 mW control field.

The grey lines in Figure 5.14 denote the bounds of a classical storage device, hence any states falling into the the bottom right quadrant are said to surpass the no-cloning limit. It can be clearly seen that none of the retrieved states used for any of the three process reconstructions fall into this regime. It should be said that this is a rather unfortunate result given that a similar system has already convincingly achieved this criterion [86].

5.4 Discussion

From the evaluations, we conclude that our Λ-GEM system does not meet any of the discussed criteria to operate as a quantum memory. This is not surprising given the thermalization measured in the output states which is clearly revealed in the process tensors shown in Figure 5.12 and the increased variance in the retrieved state quadratures. The excess noise in our system is apparent when observing the spectrum of the probe field (Fig. 5.4b) and it is correlated to the non-degenerate Raman transition used for our GEM scheme (Fig. 5.4). Based on the evidence in Section 5.2 we conclude that both FWM and Raman scattering effects are contributing factors to this observed extra noise. This is supported by the fact that the behavior of the gain features were in disagreement with the corresponding extra noise with increasing control field power. Furthermore, while extra noise did show a dependence with spatial-mode misalignment, the noise level always remained above a minimum value and could not be eliminated by alignment.

Chapter 6

Conclusion

In this thesis, a new technique for complete characterization of quantum optical processes using coherent states was developed and implemented on a selection of quantum processes, with emphasis on quantum memory. Coherent state quantum process tomography (csQPT) was performed on a "toy" process of an electro-optical modulator, bosonic creation and annihilation operators $\hat{a}^\dagger$, $\hat{a}$ and two quantum memory schemes, that of wlectromagnetically induced transparency (EIT) and gradient echo memory (GEM).

Process tomography is a powerful tool when incorporated as a routine procedure. By measuring the effect of a process on a subset of the coherent state basis one can gain enough information to completely characterize its operation. Hence, this characterization is achieved using only the states emitted from a common laser source which eliminates the need to identically prepare numerous complex input states for process optimization. Once the process tensor has been constructed, one could use it to predict the effect of that process on any arbitrary quantum state in the mode for which the quantum process has been characterized.

Our original procedure described in Section 2.6 [43], was derived from the optical equivalence theorem, which under suitable approximations in conjunction with the output data allowed the process tensor to be calculated. Output of the process on a set of coherent states was measured using homodyne detection followed by a maximum likelihood estimation for state reconstruction. The process tensor could then be used to operate on an arbitrary quantum state. The process tensor for a proof-of-principle operation comprised an EOM and PBS was constructed using measurements in the CV regime. The accuracy of the tensor was verified through its prediction on a squeezed vacuum state compared to the actual experiment with a fidelity >0.99. Improvements to the csQPT methodology were achieved by side-stepping the need for the Glauber-Sudarshan function [44], and more applicable to the work in this thesis, developing a maximum likelihood estimation for the process directly [45]. The estimation algorithm method of csQPT was advantageous in that it removed the intermediate step of reconstructing the density matrices by reconstructing the process directly from the phase and quadrature data.

The latter method was successfully implemented for characterization of the non-deterministic processes of photon annihilation $\hat{a}$ and creation $\hat{a}^\dagger$. Annihilation was done by a weak beam splitter comprised of a half-wave plate PBS combination, and creation was achieved by mode-matching the coherent states to a non-linear crystal under conditions of parametric down conversion. Any loss experienced by the probe states was accounted for directly in the reconstruction algorithm.

A large part of this thesis is dedicated to the application of the described csQPT techniques to quantum memory devices. The first technique introduced by our group [43] was applied to a quantum memory device based on EIT [137], a setup previously shown capable of receiving and preserving the quantum nature of a squeezed vacuum state [42]. Characterization was carried out for two different values of the two-field resonance. The accuracy of the reconstructed process tensors was verified by showing fidelities of > 0.99 between the predicted storage on a squeezed vacuum state compared to the actual experiment.

Finally we implemented an optical storage device base on a Λ-GEM scheme. We successfully designed and constructed an apparatus capable of retrieval efficiencies $> 80\%$ for Rubidium 87 vapour cells containing both Kr and Ne buffer gases. Multiple aspects of the GEM apparatus were investigated using both classical and quantum measurement techniques. These included the behavior of the Raman absorption lines, retrieval efficiencies and the devices' capabilities for quantum storage. Unfortunately we were unsuccessful in developing the GEM device to operate in the quantum memory regime. While high efficiencies were achievable, due to the presence of extra noise the memory performance was degraded beyond the capability of storing a quantum light state or meeting the quantum memory criteria as described in Section 5.3.2. The exact mechanism responsible for a majority of the observed extra noise remains elusive. A more intensive study is needed to improve the performance of our GEM system such that it can be classified as a quantum memory.

To summarize, based on the successful implementations of csQPT described in this thesis, we conclude that csQPT has been tested thoroughly enough to be widely applied in quantum technologies.

Appendix A

Deferred Derivations of Equations Stated in Text

A.1 Shrödinger Equation Approach for Off-Resonant Two-field Interaction

Equation (3.1) in Chapter 3 gives us the Hamiltonian of a Λ-system in the interaction picture. For the moment we will only consider coherent interactions and neglect any decay processes in the system. Also, we will change our notation by using Ω_b to denote the Rabi frequency of the probe transition $|b\rangle \rightarrow |a\rangle$ and again use $\Delta_b - \Delta_c = \delta$. We start with a single three-level atom in a completely arbitrary state such as [1]:

$$|\psi\rangle = \psi_a(t)|a\rangle + \psi_b(t)|b\rangle + \psi_c(t)|c\rangle, \tag{A.1}$$

which obeys the Schrödinger equation. Using the Hamiltonian we can calculate the dynamics of the population amplitudes to yield:

$$\dot{\psi}_a = i\Delta_b\psi_a + i\Omega_b\psi_b + \Omega_c\psi_c \tag{A.2a}$$

$$\dot{\psi}_b = i\Omega_b^*\psi_a \tag{A.2b}$$

$$\dot{\psi}_c = i\Omega_c^*\psi_a + i\delta\psi_c. \tag{A.2c}$$

In the case of Raman transitions with a far off-resonant detuning such that $\Delta_b \sim \Delta_c = \Delta$ and $|\Delta| \gg \Gamma, \Omega_c, \Omega_b$, the excited state amplitude will be small and constant to lowest

---

[1] Note that many of the derivations in this Appendix were adapted from Reference [123].

order in Ω/Δ, thus $\dot{\psi}_a \approx 0$ and then

$$\psi_a = -\frac{\Omega_b \psi_b + \Omega_c \psi_c}{\Delta}. \tag{A.3}$$

We can then use the above expression for ψ_a to calculate the time derivatives of the ground state probability amplitudes which give us:

$$\dot{\psi}_b = -i\frac{|\Omega_b|^2}{\Delta}\psi_b - i\frac{\Omega_c \Omega_b^*}{\Delta}\psi_c \tag{A.4a}$$

$$\dot{\psi}_c = i\left(\delta - \frac{|\Omega_c|^2}{\Delta}\right)\psi_c - i\frac{\Omega_b \Omega_c^*}{\Delta}\psi_b. \tag{A.4b}$$

By inspection of Equation (A.4a) and (A.4b) we can immediately see that this system behaves as an effective two-level system capable of coherent transfer of population between the ground states with an effective Rabi frequency given by Equation (4.10).

A.2 Stochastic Wave Function Method

We would like to solve for the susceptibility on the probe field transition in the presence of the control without invoking the full complexity of the density matrix formalism. The stochastic wave function method achieves this by using a non-Hermitian Hamiltonian that includes decay terms for the excited $|a\rangle$ and metastable state $|c\rangle$. If $\hat{H}$ is the original Hamiltonian of the three-level system then the new effective Hamiltonian is given by

$$H_{eff} = H - i\hbar\Gamma|a\rangle\langle a| - i\hbar\gamma_{bc}|c\rangle\langle c|, \tag{A.5}$$

where Γ is the excited state decay and γ_{bc} is the metastable state decay. Once again, we can find the time evolution of the probability amplitudes via the Schrödinger equation provided that the chance of decay is small. This is satisfied in two scenarios, the first is the weak probe regime whereby the populations in the excited $|a\rangle$ and metastable state $|c\rangle$ are of the order $|\Omega_b|^2$ or higher. Due to the low populations in these states we can neglect any decay processes originating from them. The second case is when the decay from the metastable state itself is negligible ($\gamma_{bc} \approx 0$) and the excited state population remains small $\psi_a \approx 0$ [123].

Since we are dealing with the weak probe regime, we apply our effective Hamiltonian (Eqn. (A.5)) to the general wave function (Eqn. (A.1)) to calculate the time derivatives of the amplitudes:

$$\dot{\psi}_a = i\Delta\psi_a + i\Omega_b\psi_b + \Omega_c\psi_c - \Gamma\psi_a \tag{A.6a}$$

$$\dot{\psi}_b = i\Omega_b^*\psi_a \tag{A.6b}$$

$$\dot{\psi}_c = i\Omega_c^*\psi_a + i\delta\psi_c - \gamma_{bc}\psi_c, \tag{A.6c}$$

where $\Delta_b \sim \Delta_c = \Delta$. We then note that because our probe is weak all population in $|b\rangle$ will, to first order, remain there and we can set $\psi_b \approx 1$. Now we solve Equations (A.6) for ψ_a and ψ_c in the steady state where $\dot{\psi}_a, \dot{\psi}_b, \dot{\psi}_c = 0$ followed by taking the Fourier transform of both sides to yield:

$$\Gamma_{bc}\psi_a = i\Omega_b + \Omega_c\psi_c \tag{A.7a}$$

$$\Gamma_{ba}\psi_c = i\Omega_c^*\psi_a. \tag{A.7b}$$

Note that here we have defined

$$(\Gamma - i(\Delta - \omega)) = \Gamma_{bc} \tag{A.8a}$$

$$(\gamma_{bc} - i(\delta - \omega) = \Gamma_{ba}, \tag{A.8b}$$

which are known as the complex decay rates and are frequency dependent. We are now able to solve for the density matrix components with:

$$\sigma_{bb} = |\psi_b|^2 \tag{A.9a}$$

$$\sigma_{cb} = \psi_b^* \psi_c = -\frac{\Omega_c \Omega_b^*}{\Gamma_{bc}\Gamma_{ba} + |\Omega_c|^2} \tag{A.9b}$$

$$\sigma_{ab} = \psi_b^* \psi_a = i\Omega_b \frac{\Gamma_{bc}}{\Gamma_{bc}\Gamma_{ba} + |\Omega_c|^2}. \tag{A.9c}$$

We are interested in the linear susceptibility of the transition of the probe field with the excited state which has the relation

$$\chi_{ba} \propto \frac{\sigma_{ab}}{\Omega_b}, \tag{A.10}$$

and from Equations (A.9) we can arrive at

$$\frac{\sigma_{ba}}{\Omega_b} = \frac{i}{\Gamma_{ba}} \left(1 - \frac{|\Omega_c|^2/\Gamma_{ba}}{\Gamma_{bc} + |\Omega_c|^2/\Gamma_{ba}} \right). \tag{A.11}$$

From the RHS of Equation (A.11) we can see two terms, the first describes the single field transition, while the second describes the two-field transitions which we will look at more carefully. In the limit of $\Delta \gg \Gamma$ the complex decay given in Equations (A.8) is simply $\Gamma_{ba} \approx -i\Delta$ and Equation (A.11) becomes:

$$\frac{\sigma_{ba}}{\Omega_b} - \frac{i}{\Gamma_{ba}} \approx \frac{i\frac{|\Omega_c|^2}{\Delta^2}}{\Gamma_{bc} + \frac{|\Omega_c|^2}{\Delta^2}(\Gamma + i\Delta)}, \tag{A.12a}$$

$$\frac{\sigma_{ba}}{\Omega_b} - \frac{i}{\Gamma_{ba}} \approx \frac{i\frac{|\Omega_c|^2}{\Delta^2}}{\gamma_{bc} + \Gamma\frac{|\Omega_c|^2}{\Delta^2} - i(\delta - \frac{|\Omega_c|^2}{\Delta})}. \tag{A.12b}$$

Equation (A.12b) describes the characteristics we are interested in. The real term in the denominator gives the width of our Raman absorption line as stated in Equation (4.13) and the complex component sets the two-photon resonance condition as stated in Section 4.4.1.

A.3 Maxwell Bloch Equations for a Two-Level System

Starting with Equation (4.14) for the Jaynes-Cummings Hamiltonian for the light-matter interaction in a two-level system, we can time-evolve the components of the density operator via the Liouville Equation

$$\partial_t \hat{\sigma} = -\frac{i}{\hbar}[\hat{H}_{int}, \hat{\sigma}]. \tag{A.13}$$

Here, the atomic operator $\hat{\sigma}$ corresponds to the collective atomic operator averaged over the ensemble of atoms such that:

$$\hat{\sigma_{ij}} = \frac{1}{N}\sum_{k}^{N} \sigma_{i,j}^{(k)}. \tag{A.14}$$

Finding the time evolution for the coherence between the excited and ground state σ_{ba} we arrive at[2]:

$$\partial_t \sigma_{ba} = -i\delta\sigma_{ab} + ig\mathcal{E}(\sigma_{bb} - \sigma_{aa}). \tag{A.15}$$

We also need to find the time evolution of the of the amplitude of the electric field $\mathcal{E}$ and to do so we need to include a photonic component into the Hamiltonian as follows:

$$H = H_{photon} + H_{int} = \hbar\omega\mathcal{E}^{\dagger}\mathcal{E} + H_{int}, \tag{A.16}$$

which we will use in Heisenberg Equation to yield:

$$\partial_t \mathcal{E} = -\frac{i}{\hbar}[\mathcal{E}, H] = -i[\mathcal{E}, \omega\mathcal{E}^{\dagger}\mathcal{E}] + igN\sigma_{ba}[\mathcal{E}, \mathcal{E}^{\dagger}] \tag{A.17a}$$

$$\partial_t \mathcal{E} = -i\omega\mathcal{E} + igN\sigma_{ba}. \tag{A.17b}$$

Using the fact that the electric field envelope is formally given by the Fourier transform over all optical modes $\mathcal{E}(z,t) = \int a_k(t)e^{ikz}dk$ [134] along with $\omega = ck$ we can write:

$$ick\mathcal{E} = ick\int a_k(t)e^{ikz}dk = c\partial_z \int a_k(t)e^{ikz}dk = c\partial_z\mathcal{E}. \tag{A.18}$$

---

[2] For the remainder of this analysis we will omit the hats on the operators for simplicity.

Substituting the result from Equation (A.18) into Equation (A.17b) we find

$$(\partial_t + c\partial_z)\mathcal{E} = igN\sigma_{ba}, \tag{A.19}$$

and then by moving to the frame at the speed of light where $z \to z - t/c$ we arrive at [134]

$$\partial_z\mathcal{E} = i\frac{gN}{c}\sigma_{ba}. \tag{A.20}$$

From here, Equations (A.15) and (A.20) in conjunction with the weak probe approximation $\sigma_{bb} \approx 1$ get us to the familiar Maxwell Bloch Equations for a two-level system (Equation (4.3)):

$$\partial_t\sigma_{ba} = -(\Gamma + i\delta)\sigma_{ba} + ig\mathcal{E} \tag{A.21a}$$

$$\partial_z\mathcal{E} = i\mathcal{N}\sigma_{ba}. \tag{A.21b}$$

Here, $\mathcal{N} = gN/c$ is the effective linear atomic density and we have simply added in the decay term Γ.

A.4 Effective Two-Level System

We now want to derive a similar set of evolution equations for the atomic operators in an ensemble of Λ-atoms. We begin with the interaction Hamiltonian (4.14) stated in Section 4.4.2 and calculate the time evolution of the coherences of the ground state with the excited σ_{ba} and metastable σ_{bc} states:

$$\partial_t\sigma_{ba} = -i\Delta\sigma_{ba} + ig\mathcal{E}(\sigma_{bb} - \sigma_{aa}) + i\Omega_c\sigma_{bc}, \tag{A.22a}$$

$$\partial_t\sigma_{bc} = -i\delta\sigma_{bc} - ig\mathcal{E}\sigma_{ac} + i\Omega_c^*\sigma_{ba}. \tag{A.22b}$$

Similar to the two-level system, we will once again use the weak probe approximation such that $\sigma_{bb} \approx 1$. As a result the coherence between the metastable and excited state will be of order $\sim |\mathcal{E}|^2$ which we can take to be approximately zero. Our coherences then become

$$\partial_t \sigma_{ba} = -i\Delta\sigma_{ba} + ig\mathcal{E} + i\Omega_c\sigma_{bc}, \tag{A.23a}$$

$$\partial_t \sigma_{bc} = -i\delta\sigma_{bc} + i\Omega_c^*\sigma_{ba}. \tag{A.23b}$$

As described in Section 4.4.2, we adiabatically eliminate fast excited-state fluctuations with the assumption $|\partial_t\sigma_{ba}| \ll |\Delta\sigma_{ba}|$ and by solving for σ_{ba} we arrive at:

$$\sigma_{ba} = \frac{gN}{\Delta}\mathcal{E} + \frac{\Omega}{\Delta}\sigma_{bc}. \tag{A.24}$$

We then substitute Equation (A.24) into both Equations (A.23b) and (A.21b) to yield

$$\partial_t \sigma_{bc} = -(i\delta + i\frac{|\Omega_c|^2}{\Delta})\sigma_{bc} + i\frac{gN\Omega_c}{\Delta_c}\mathcal{E}, \tag{A.25a}$$

$$\partial_z \mathcal{E} = i\frac{g\mathcal{N}}{\Delta}\hat{\mathcal{E}} + i\frac{g\mathcal{N}\Omega_c}{\Delta_c}\hat{\sigma}_{bc}. \tag{A.25b}$$

The AC-stark shift term in Equation (A.25a) can be accounted for when selecting the exact resonance of the split Raman absorption line. The first term on the right hand side of the Maxwell equation (Eqn. (A.25b)) can be removed with the transformations such that $\mathcal{E} \to \mathcal{E}e^{i\frac{g\mathcal{N}}{\Delta}}$ and $\Omega_c \to \Omega_c e^{-i\frac{g\mathcal{N}}{\Delta}}$ [134]. Finally we add in the term to account for the decay between the ground states γ_{bc} to get

$$\partial_t \sigma_{bc} = -(\gamma_{bc} + i\delta)\sigma_{bc} - i\frac{g\Omega_c}{\Delta}\mathcal{E}, \tag{A.26a}$$

$$\partial_z \mathcal{E} = i\frac{g\mathcal{N}\Omega_c}{\Delta}\sigma_{bc}. \tag{A.26b}$$

We can see that our far off-resonant three-level system is now described by dynamics equivalent to Equations A.21 for a two-level system.

Bibliography

[1] K. Hammerer, M. M. Wolf, E. S. Polzik, and J. I. Cirac. Quantum benchmark for storage and transmission of coherent states. *Physical Review Letters*, 94(15):150503, April 2005.

[2] W. Tittel, M. Afzelius, T. Chanelière, R. L. Cone, S. Kröll, S. A. Moiseev, and M. Sellars. Photon-echo quantum memory in solid state systems. *Laser and Photonics Reviews*, 4(2):244 – 267, February 2010.

[3] Mahdi Mosseini. *Quantum Optical Storage and Processing Using Raman Gradient Echo Memory.* PhD thesis, Australian National University, May 2012.

[4] N. Gisin, G. Ribordy, W. Tittel, and H. Zbinden. Quantum cryptography. *Reviews of Modern Physics*, 74:145–195, March 2002.

[5] S. Ritter, C. Nölleke, C. Hahn, A. Reiserer, A. Neuzner, M. Uphoff, M. Mücke, E. Figueroa, J. Bochmann, and G. Rempe. An elementary quantum network of single atoms in optical cavities. *Nature*, 484:195, April 2012.

[6] E. Knill, R. Laflamme, and G. J. Milburn. A scheme for efficient quantum computation with linear optics. *Nature*, 409:46–52, January 2001.

[7] P. J. Shadbolt, M. R. Verde, A. Peruzzo, A. Politi, A. Laing, M. Lobino, J.C.F. Matthews, and J. L. O'Brien. Generating, manipulating and measuring entanglement and mixture with a reconfigurable photonic circuit. *Nature Photonics*, 6:45–49, December 2012.

[8] R. Ursin et al. Quantum teleportation link across the danube. *Nature*, 430:849, August 2004.

[9] Jian-Wei Pan et al. Quantum teleportation and entanglement distribution over 100-kilometre free-space channels. *Nature*, 488:185–188, August 2012.

[10] J. Appel et al. Mesoscopic atomic entanglement for precision measurements beyond the standard quantum limit. *Proceedings of the National Academy of Sciences*, 106:10960–10965, July 2009.

[11] E. Bimbard, N. Jain, A. MacRae, and A. I. Lvovsky. Quantum-optical state engineering up to the two-photon level. *Nature Photonics*, 4:243–247, February 2010.

[12] C. K. Law and H. J. Kimble. Deterministic generation of a bit-stream of single photon pulses. *Journal of Modern Optics*, 44:2067–2074, 1997.

[13] A. MacRae, T. Brannan, R. Achal, and A. I. Lvovsky. Tomography of a high-purity narrowband photon from a transient atomic collective excitation. *Physical Review Letters*, 109(3):033601, July 2012.

[14] A. I. Lvovsky, B. C. Sanders, and W. Tittel. Optical quantum memory. *Nature Photonics*, 3:706 – 714, November 2009.

[15] W. K. Wooters and W. H. Zurek. A single quantum cannot be cloned. *Nature*, 299:802–803, October 1982.

[16] L.-M. Duan, M. D. Lukin, J. I. Cirac, and P. Zoller. Long-distance quantum communication with atomic ensembles and linear optics. *Nature*, 414:413–418, November 2001.

[17] N. Sangouard, C. Simon, H. de Riedmatten, and N. Gisin. Quantum repeaters based on atomic ensembles and linear optics. *Reviews of Modern Physics*, 83(1):33 – 80, March 2011.

[18] H.-J. Briegel, W. Dür, J. I. Cirac, and P. Zoller. Quantum repeaters: The role of imperfect local operations in quantum communication. *Physical Review Letters*, 81(26):5932–5935, December 1998.

[19] C. Simon, H. de Riedmatten, M. Afzelius, N. Sangouard, H. Zbinden, and N. Gisin. Quantum repeaters with photon pair sources and multimode memories. *Physical Review Letters*, 98(19):190503, October 2007.

[20] K. T. McCusker and P. G. Kwiat. Efficient optical quantum state engineering. *Physical Review Letters*, 103:163602, 2009.

[21] M. Hosseini, B. M. Sparkes, G. T. Campbell, P. K. Lam, and B. C. Buchler. Storage and manipulation of light using a raman gradient-echo process. *Journal of Physics B: Atomic, Molecular and Optical Physics*, 45:124004, 2012.

[22] B. Julsgaard, J. Sherson, J.I. Cirac, J. Fiurášek, and E. S. Polzik. Experimental demonstration of quantum memory for light. *Nature*, 432:482–486, November 2004.

[23] M. Mohseni, A. T. Rezakhani, and D. A. Lidar. Quantum process tomography: Resource analysis of different strategies. *Physical Review A*, 77(3):032322, March 2008.

[24] Z. Hradil, J. Rehacek, J. Fiurasek, and M. Jezek. *Maximum-likelihood methods in quantum mechanics Quantum State Estimation*. Springer, 2004.

[25] A. I. Lvovsky and M. G. Raymer. Continuous-variable optical quantum-state tomography. *Reviews of Modern Physics*, 81(1):299 – 332, March 2009.

[26] L. Marchildon. *Quantum Mechanics: From Basic Principles to Numerical Methods and Applications*. Springer, 2002.

[27] U. Leonhardt. *Measuring the Quantum State of Light.* Cambridge University Press, 1997.

[28] L. Mandel and E. Wolf. *Optical Coherence and Quantum Optics.* Cambridge University Press, 1995.

[29] R.J. Glauber. Coherent and incoherent states of radiation field. *Physical Review*, 131(6):2766–2788, September 1963.

[30] E. C. G. Sudarshan. Equivalence of semiclassical and quantum mechanical descriptions of statistical light beams. *Physical Review Letters*, 10(7):277–279, April 1963.

[31] R. Kumar, E. Barrios, A. MacRae, E. Cairns, E. H. Huntington, and A. I. Lvovsky. Versatile wideband balanced detector for quantum optical homodyne tomography. *Optics Communications*, 285:5259–5267, August 2012.

[32] Mary L. Boas. *Mathematical Methods in the Physical Sciences.* John Wiley and Sons, 1983.

[33] K. B. Petersen and M. S. Pedersen. The matrix cookbook. *http://matrixcookbook.com.*

[34] Z. Hradil, D. Mogilevtsev, and J. Řeháček. Biased tomography schemes: An objective approach. *Physical Review Letters*, 96(23):230401, June 2006.

[35] A. I. Lvovsky. Iterative maximum-likelihood reconstruction in quantum homodyne tomography. *Journal of Optics B: Quantum Semiclassical Optics*, 6:S556 – S559, May 2004.

[36] J. S. Lundeen, A. Feito, H. Coldenstrodt-Ronge, K. L. Pregnell, Ch. Silberhorn,

T. C. Ralph, J. Eisert, M. B. Plenio, and I. A. Walmsley. Tomography of quantum detectors. *Nature Physics*, 5:27–30, November 2009.

[37] L. Zhang, H. B. Coldenstrodt-Ronge, A. Datta, G. Puentes, J. S. Lundeen, X-M. Jin, B. J. Smith, M. B. Plenio, and I. A. Walmsley. Mapping coherence in measurement via full quantum tomography of a hybrid optical detector. *Nature Photonics*, 6:364–368, May 2012.

[38] J. B. Altepeter, D. Branning, E. Jeffrey, T. C. Wei, P. G. Kwiat, R. T. Thew, J. L. O'Brien, M. A. Nielsen, and A. G. White. Ancilla-assisted quantum process tomography. *Physical Review Letters*, 90(19):193601, May 2003.

[39] R. J. Glauber. Photon correlations. *Physical Review Letters*, 10(3):84–86, February 1963.

[40] J. R. Klauder. Improved version of optical equivalence theorem. *Physical Review Letters*, 16(12):534–536, March 1966.

[41] A. I. Lvovsky. *Nonlinear and Quantum Optics*. University of Calgary, Department of Physics and Astronomy, Fall 2012.

[42] J. Appel, E. Figueroa, D. Korystov, M. Lobino, and A. I. Lvovsky. Quantum memory for squeezed light. *Physical Review Letters*, 100(9):093602, March 2008.

[43] M. Lobino, D. Korystov, C. Kupchak, E. Figueroa, B. C. Sanders, and A. I. Lvovsky. Complete characterization of quantum-optical processes. *Science*, 322(5901):563 – 566, October 2008.

[44] S. Rahimi-Keshari, A. Scherer, A. Mann, A. T. Rezakhani, A. I. Lvovsky, and B. C. Sanders. Quantum process tomography with coherent states new journal of physics 13, 013006 (2011). *New Journal of Physics*, 13:013006, January 2011.

[45] A. Anis and A. I. Lvovsky. Maximum-likelihood coherent-state quantum process tomography. *New Journal of Physics*, 14:105021, October 2012.

[46] K. E. Cahill. Coherent-state representations for the photon density operator. *Physical Review*, 138:B1566–B1576, June 1965.

[47] R. Kumar, E. Barrios, C. Kupchak, and A. I. Lvovsky. Experimental characterization of bosonic photon creation and annihilation operators. *Physical Review Letters*, 110(13):130403, March 2013.

[48] A. Ourjoumtsev, R. Tualle-Brouri, J. Laurat, and P. Grangier. Generating optical schrödinger kittens for quantum information processing. *Science*, 312(5770):83–86, April 2006.

[49] J. S. Neergaard-Nielsen, M. Takeuchi, K. Wakui, H. Takahashi, K. Hayasaka, M. Takeoka, and M. Sasaki. Optical continuous-variable qubit. *Physical Review Letters*, 105(5):053602, July 2010.

[50] H. Takahashi, J. S. Neergaard-Nielsen, M. Takeuchi, M. Takeoka, K. Hayasaka, A. Furusawa, and M. Sasaki. Entanglement distillation from gaussian input states. *Nature Photonics*, 4:178, February 2010.

[51] A. Zavatta, V. Parigi, M. S. Kim, H. Jeong, and M. Bellini. Experimental demonstration of the bosonic commutation relation via superpositions of quantum operations on thermal light fields. *Physical Review Letters*, 103(14):140406, October 2009.

[52] G. Alzetta, A. Gozzini, L. Moi, and G. Orriols. An experimental method for the observation of r.f. transitions and laser beat resonances in oriented na vapour,. *Nuovo Cimento Soc. Ital. Fis. B*, 36(5), 1976.

[53] Peter Marzlin. *Physics 615: Advanced Quantum Mechanics I.* University of Calgary, Department of Physics and Astronomy, Winter 2008.

[54] M. Fleischhauer, A. Imamoglu, and J. P. Marangos. Electromagnetically induced transparency: Optics in coherent media. *Reviews of Modern Physics*, 77(2):633–673, 2005.

[55] E. Figueroa, F. Vewinger, J. Appel, and A. I. Lvovsky. Decoherence of electromagnetically-induced transparency in atomic vapor. *Optics Letters*, 31(17):2625 – 2627, September 2006.

[56] D. Budker, D. F. Kimball, S. M. Rochester, and V. V. Yashchuk. Nonlinear magneto-optics and reduced group velocity of light in atomic vapor with slow ground state relaxation. *Physical Review Letters*, 83(9):1767, August 1999.

[57] L. V. Hau, S. E. Harris, Z. Dutton, and C. H. Behroozi. Light speed reduction to 17 metres per second in an ultracold atomic gas. *Nature*, 397:594–598, February 1999.

[58] A. MacRae, G. Campbell, and A. I. Lvovsky. Matched slow pulses using double electromagnetically induced transparency. *Optics Letters*, 33(22):2659–2661, November 2008.

[59] M. Fleischhauer and M. D. Lukin. Dark-state polaritons in electromagnetically induced transparency. *Physical Review Letters*, 84(22):5094–50978, May 2000.

[60] D. F. Phillips, A. Fleischhauer, A. Mair, R. L. Walsworth, and M. D. Lukin. Storage of light in atomic vapor. *Physical Review Letters*, 86(5):783–786, January 2001.

[61] C. Liu, Z. Dutton, C. H. Behroozi, and L. V. Hau. Observation of coherent optical information storage in an atomic medium using halted light pulses. *Nature*,

409:490–493, January 2001.

[62] C. H. van der Wal, M. D. Eisaman, A. André, R. L. Walsworth, D. F. Phillips, A. S. Zibrov, and M. D. Lukin. Atomic memory for correlated photon states. *Science*, 301(5630):196–200, May 2003.

[63] M. Bajcsy, A. S. Zibrov, and M. D. Lukin. Stationary pulses of light in an atomic medium. *Nature*, 426:638–641, December 2003.

[64] A.V. Gorshkov, A. Andre, M. Fleischhauer, A.S. Sorensen, and M.D. Lukin. Universal approach to optimal photon storage in atomic media. *Physical Review Letters*, 98(12):123601, March 2007.

[65] N. B. Phillips, A. V. Gorshkov, , and I. Novikova. Optimal light storage in atomic vapor. *Physical Review A*, 78(2):023801, August 2008.

[66] I. Novikova, N. B. Phillips, and A. V. Gorshkov. Optimal light storage with full pulse shape control. *Physical Review A*, 78(2):021802, August 2008.

[67] I. Novikova, A.V. Gorshkov, D.F. Phillips, A.S. Sorensen, M.D. Lukin, and R.L. Walsworth. Optimal control of light pulse storage and retrieval. *Physical Review Letters*, 98(24):243602, June 2007.

[68] M. Shuker, O. Firstenberg, R. Pugatch, A. Ron, and N. Davidson. Storing images in warm atomic vapor. *Physical Review Letters*, 100(22):223601, June 2008.

[69] A. V. Turukhin, V. S. Sudarshanam, M. S. Shahriar, J. A. Musser, and B. S. Ham P. R. Hemmer. Observation of ultraslow and stored light pulses in a solid. *Physical Review Letters*, 88(2):023602, December 2001.

[70] J. J. Longdell, E. Fraval, M. J. Sellars, and N. B. Manson. Stopped light with storage times greater than one second using electromagnetically induced transparency

in a solid. *Physical Review Letters*, 95(6):063601, August 2005.

[71] R. Zhang, S. R. Garner, and L. V. Hau. Creation of long-term coherent optical memory via controlled nonlinear interactions in bose-einstein condensates. *Physical Review Letters*, 103(23):233602, December 2009.

[72] L. Li, Y. Dudin, and A. Kuzmich. Seconds-scale light storage. 43rd Annual Meeting of the APS Division of Atomic, Molecular and Optical Physics (Poster), June 2012.

[73] M. Mücke, E. Figueroa, J. Bochmann, C. Hahn, K. Murr, S. Ritter, C.J. Villas-Boas, and G. Rempe. Electromagnetically induced transparency with single atoms in a cavity. *Nature*, 465:755–758, May 2010.

[74] H.P. Specht, C. Nölleke, A. Reiserer, M. Uphoff, E. Figueroa, S. Ritter, and G. Rempe. A single-atom quantum memory. *Nature*, 473:190–193, May 2011.

[75] M. T. L. Hsu, G. Hétet, O. Glöckl, J. J. Longdell, B. C. Buchler, H.-A. Bachor, and P. K. Lam. Quantum study of information delay in electromagnetically induced transparency. *Physical Review Letters*, 97(18):183601, November 2006.

[76] D. Akamatsu, K. Akiba, and M. Kozuma. Electromagnetically induced transparency with squeezed vacuum. *Physical Review Letters*, 92(20):203602, May 2004.

[77] E. Figueroa, M. Lobino, D. Korystov, J. Appel, and A. I. Lvovsky. Propagation of squeezed vacuum under electromagnetically induced transparency. *New Journal of Physics*, 11:013044, January 2009.

[78] T. Chaneliere, D. Matsukevich, S. D. Jenkins, S.-Y. Lan, T. A. B. Kennedy, and A. Kuzmich. Storage and retrieval of single photons transmitted between remote quantum memories. *Nature*, 438:833–836, December 2005.

[79] M.D. Eisaman, A. Andre, F. Massou, M. Fleischhauer, A.S. Zibrov, and M.D. Lukin. Electromagnetically induced transparency with tunable single-photon pulses. *Nature*, 438:837–841, December 2005.

[80] K. Honda, D. Akamatsu, M. Arikawa, Y. Yokoi, K. Akiba, S. Nagatsuka, T. Tanimura, A. Furusawa, and M. Kozuma. Storage and retrieval of a squeezed vacuum. *Physical Review Letters*, 100(9):093601, March 2008.

[81] M. Arikawa, K. Honda, D. Akamatsu, S. Nagatsuka, A. Furusawa, and M. Kozuma. Quantum memory of a squeezed vacuum for arbitrary frequency sidebands. *Physical Review A*, 81(2):021605(R), February 2010.

[82] K. S. Choi, H. Deng, J. Laurat, and H. J. Kimble. Mapping photonic entanglement into and out of a quantum memory. *Nature*, 452:67–71, March 2008.

[83] H. Zhang et al. Preparation and storage of frequency-uncorrelated entangled photons from cavity-enhanced spontaneous parametric downconversion. *Nature Photonics*, 5:628–632, September 2011.

[84] J. Appel, A. MacRae, and A. I. Lvovsky. Versatile digital ghz phase lock for external cavity diode lasers. *Measurement Science and Technology*, 20(5):055302, May 2009.

[85] G. Hetet, A. Peng, M. T. Johnsson, J. J. Hope, and P. K. Lam. Characterization of electromagnetically-induced-transparency-based continuous-variable quantum memories. *Physical Review A*, 77(1):012323, January 2008.

[86] M. Hosseini, G. Campbell, B. M. Sparkes, P. K. Lam, and B. C. Buchler. Unconditional room-temperature quantum memory. *Nature Physics*, 7:794–798, June 2011.

[87] M. Afzelius, C. Simon, H. de Riedmatten, and N. Gisin. Multimode quantum memory based on atomic frequency combs. *Physical Review A*, 79(5):052329, May 2009.

[88] R. H. Dicke. Coherence in spontaneous radiation processes. *Physical Review*, 93(99), 1954.

[89] C. Ottaviani, C. Simon, H. de Riedmatten, M. Afzelius, B. Lauritzen, N. Sangouard, and N. Gisin. Creating single collective atomic excitations via spontaneous raman emission in inhomogeneously broadened systems: Beyond the adiabatic approximation. *Physical Review A*, 79(6):063828, June 2009.

[90] M. U. Staudt, M. Afzelius, H. de Riedmatten, S. R. Hastings-Simon, C. Simon, R. Ricken, H. Suche, W. Sohler, and N. Gisin. Interference of multimode photon echoes generated in spatially separated solid-state atomic ensembles. *Physical Review Letters*, 99(17):173602, October 2007.

[91] J. Ruggiero, J.-L. Le Gouet, C. Simon, and T. Chanelière. Why the two-pulse photon echo is not a good quantum memory protocol. *Physical Review A*, 79(5):053851, May 2009.

[92] M. U. Staudt, S. R. Hastings-Simon, M. Nilsson, M. Afzelius, V. Scarani, R. Ricken, H. Suche, W. Sohler, W. Tittel, and N. Gisin. Fidelity of an optical memory based on stimulated photon echoes. *Physical Review Letters*, 98(11):113601, March 2007.

[93] N. Sangouard, C. Simon, J. Minar, M. Afzelius, T. Chanelière, N. Gisin, J.-L. Le Gouet, H. de Riedmatten, and W. Tittel. On the impossibility of faithfully storing single-photons with three-pulse photon echo. *Physical Review A*, 81(6):062333, June 2010.

[94] S. A. Moiseev and S. Kröll. Complete reconstruction of the quantum state of a single-photon wave packet absorbed by a doppler-broadened transition. *Physical Review Letters*, 87(17):173601, October 2001.

[95] S. A. Moiseev V. F. Tarasov and B. S. Ham. Quantum memory photon echo-like techniques in solids. *Journal of Optics B: Quantum and Semiclassical Optics*, 5(4):S497–S502, August 2003.

[96] B. Kraus, W. Tittel, N. Gisin, M. Nilsson, S. Kröll, and J. I. Cirac. Quantum memory for nonstationary light fields based on controlled reversible inhomogeneous broadening. *Physical Review A*, 73(020302(R)), 2006.

[97] M. Nilsson and S. Kröll. Solid state quantum memory using complete absorption and re-emission of photons by tailored and externally controlled inhomogeneous absorption profiles. *Optics Communications*, 247:393–403, March 2005.

[98] A. L. Alexander, J. J. Longdell, M. J. Sellars, and N. B. Manson. Photon echoes produced by switching electric fields. *Physical Review Letters*, 96(4):043602, February 2006.

[99] N. Sangouard, C. Simon, M. Afzelius, and N. Gisin. Analysis of a quantum memory for photons based on controlled reversible inhomogeneous broadening. *Physical Review A*, 75(3):032327, March 2007.

[100] B. Lauritzen, H. de Riedmatten J. Minář, M. Afzelius, N. Sangouard, C. Simon, and N. Gisin. Telecommunication-wavelength solid-state memory at the single photon level. *Physical Review Letters*, 104(8):080502, February 2010.

[101] J. Nunn, K. Reim, K. C. Lee, V. O. Lorenz, B. J. Sussman, I. A. Walmsley, and D. Jaksch1. Multimode memories in atomic ensembles. *Physical Review Letters*, 101:260502, December 2008.

[102] H. de Riedmatten, M. Afzelius, M. U. Staudt, C. Simon, and N. Gisin. A solid state light-matter interface at the single photon level. *Nature*, 456:773–777, December 2008.

[103] M. Afzelius, I. Usmani, A. Amari, B. Lauritzen, A. Walther, C. Simon, N. Sangouard, J. Minář, H. de Riedmatten, N. Gisin, and S. Kröll. Demonstration of atomic frequency comb memory for light with spin-wave storage. *Physical Review Letters*, 104(4):040503, January 2010.

[104] N. Timoney, B. Lauritzen, I. Usmani, M Afzelius, and N Gisin. Atomic frequency comb memory with spin-wave storage in 153 eu 3 + :y 2 sio 5. *Journal of Physics B: Atomic, Molecular and Optical Physics*, 45:124001, 2012.

[105] N. Timoney, I. Usmani, P. Jobez, M. Afzelius, and N. Gisin. Single-photon-level optical storage in a solid-state spin-wave memory. *arXiv:1301.6924*.

[106] T. Chanelière, J. Ruggiero, M. Bonarota, M. Afzelius, and J-L. Le Gouët. Efficient light storage in a crystal using an atomic frequency comb. *New Journal of Physics*, 12:023025, February 2010.

[107] A. Amari, A. Walther, M. Sabooni, M. Huang, S. Kroll, M. Afzelius, I. Usmani, B. Lauritzen, N. Sangouard, H. de Riedmatten, and N. Gisin. Towards an efficient atomic frequency comb quantum memory. *Journal of Luminescence*, 130(9):1579–1585, September 2010.

[108] M. Sabooni, Q. Li, S. Kröll, and L. Rippe. Efficient quantum memory using a weakly absorbing sample. *Physical Review Letters*, 110(13):133604, March 2013.

[109] E. Saglamyurek, N. Sinclair, J. Jin, J. A. Slater, D. Oblak, F. Bussières, M. George, R. Ricken, W. Sohler, and W. Tittel. Broadband waveguide quantum memory for entangled photons. *Nature*, 469:512–515, January 2011.

[110] C. Clausen, I. Usmani, F. Bussières, N. Sangouard, M. Afzelius, H. de Riedmatten, and N.Gisin. Quantum storage of photonic entanglement in a crystal. *Nature*, 469:508–511, January 2011.

[111] I. Usmani, C. Clausen, N. Sangouard F. Bussières, M. Afzelius, and N. Gisin. Heralded quantum entanglement between two crystals. *Nature Photonics*, 6:234–237, March 2012.

[112] E. Saglamyurek, N. Sinclair, J. Jin, J. A. Slater, D. Oblak, F. Bussières, M. George, R. Ricken, W. Sohler, and W. Tittel. Conditional detection of pure quantum states of light after storage in a tm-doped waveguide. *Physical Review Letters*, 108(8):083602, February 2012.

[113] C. Clausen, F. Bussières, M. Afzelius, and Nicolas Gisin. Quantum storage of heralded polarization qubits in birefringent and anisotropically absorbing materials. *Physical Review Letters*, 108(19):190503, May 2012.

[114] M. Gündoğan, P. M. Ledingham, A. Almasi, M. Cristiani, and H. de Riedmatten. Quantum storage of a photonic polarization qubit in a solid. *Physical Review Letters*, 108(19):190504, May 2012.

[115] Z. Zhou, W-B. Lin, M. Yang, C-F. Li, and G-C. Guo. Realization of reliable solid-state quantum memory for photonic polarization qubit. *Physical Review Letters*, 108(19):190505, May 2012.

[116] G. Hétet, J. J. Longdell, M. J. Sellars, P. K. Lam, and B. C. Buchler. Multimodal properties and dynamics of gradient echo quantum memory. *Physical Review Letters*, 101(20):203601, November 2008.

[117] C. Gerry and P. Knight. *Introductory Quantum Optics*. Cambridge University Press, 2005.

[118] J. J. Longdell, G. Hetet, P. K. Lam, and M. J. Sellars. Analytic treatment of controlled reversible inhomogeneous broadening quantum memories for light using two-level atoms. *Physical Review A*, 78(3):032337, September 2008.

[119] S. A. Moiseev and N. M. Arslanov. Efficiency and fidelity of photon-echo quantum memory in an atomic system with longitudinal inhomogeneous broadening. *Physical Review A*, 78(2):023803, August 2008.

[120] G. Hetet, J. J. Longdell, A. L. Alexander, P. K. Lam, and M. J. Sellars. Electro-optic quantum memory for light using two-level atoms. *Physical Review Letters*, 100(2):023601, January 2008.

[121] M. P. Hedges, J. J. Longdell, Y. Li, and M. J. Sellars. Efficient quantum memory for light. *Nature*, 465:1052–1056, June 2010.

[122] M. P. Hedges. *High Performance Solid State Quantum Memory.* PhD thesis, Australian National University, 2011.

[123] Mikhail D. Lukin. *Physics 285b. Modern Atomic and Optical Physics II.* Harvard University, Department of Physics, Cambride, MA, Fall 2009.

[124] G. Hétet, M. Hosseini, B. M. Sparkes, D. Oblak, P. K. Lam, and B. C. Buchler. Photon echoes generated by reversing magnetic field gradients in a rubidium vapor. *Optics Letters*, 33(20):2323–2325, October 2008.

[125] M. Hosseini, B. M. Sparkes, G. Hétet, J. Longdell, P. K. Lam, and B. C. Buchler. A coherent optical pulse sequencer for quantum applications. *Nature*, 461:241–245, September 2009.

[126] M. Hosseini, B. M. Sparkes, G. Campbell, P. K. Lam, and B. C. Buchler. High

efficiency coherent optical memory with warm rubidium vapour. *Nature Communications*, 2:174, February 2011.

[127] M. Erhard and H. Helm. Buffer-gas effects on dark resonances: Theory and experiment. *Physical Review A*, 63:043813, 2001.

[128] R. H. Dicke. The effect of collisions upon the doppler width of spectral lines. *Physical Review*, 89:472–473, January 1953.

[129] M. D. Rotondaro and G. P. Perram. Collisional broadening and shift of the rubidium d1 and d2 lines (2s12 52p12, 52p32) by rare gases, h2, d2, n2, ch4 and cf4. *Journal of Quantitative Spectroscopy and Radiative Transfer*, 57(4):497, 1997.

[130] W. Happer. Optical pumping. *Reviews of Modern Physics*, 44(2):169–249, April 1972.

[131] D. A. Steck. Rubidium 87 d line data. *http://steck.us/alkalidata.*

[132] V. Scarani, S. Iblisdir, and N. Gisin. Quantum cloning. *Reviews of Modern Physics*, 77(4):1225–1256, November 2005.

[133] Andrew MacRae. *An Atomic Source of Quantum Light.* PhD thesis, University of Calgary, June 2012.

[134] Gabriel Hétet. *Quantum Memories for Continuous Variable States of Light in Atomic Ensembles.* PhD thesis, Australian National University, October 2008.

[135] P. Palittapongarnpim, A. MacRae, and A. I. Lvovsky. A monolithic filter cavity for experiments in quantum optics. *Review of Scientific Instruments*, 83(6):066101, June 2012.

[136] M. T. Turnbull, P. G. Petrov, C. S. Embrey, A. M. Marino, and V. Boyer. Role of the phase-matching condition in non-degenerate four-wave mixing in hot vapors for the generation of squeezed states of light. *arXiv:1303.7187*.

[137] M. Lobino, C. Kupchak, E. Figueroa, and A. I. Lvovsky. Memory for light as a quantum process. *Physical Review Letters*, 102(20):203601, May 2009.

[138] F. Grosshans and P. Grangier. Quantum cloning and teleportation criteria for continuous quantum variables. *Physical Review A*, 64(1):010301(R), June 2001.

[139] J. Ortalo, J. Cviklinski, P. Lombardi, J. Laurat, A. Bramati, M. Pinard, and E. Giacobino. Atomic-ensemble-based quantum memory for sideband modulations. *Journal of Physics B: Atomic, Molecular and Optical Physics*, 42(11):114010, May 2009.